

Arbeitsbericht NAB 19-07

**Self-sealing of fractures in
Opalinus Clay: experiments and
a conceptual framework for
quantitative assessments**

January 2019

A. Seiphoori

Massachusetts Institute of Technology,
Department of Earth & Atmospheric,
& Planetary Sciences, USA

**National Cooperative
for the Disposal of
Radioactive Waste**

Hardstrasse 73
P.O. Box 280
5430 Wettingen
Switzerland
Tel. +41 56 437 11 11
www.nagra.ch

Arbeitsbericht NAB 19-07

Self-sealing of fractures in Opalinus Clay: experiments and a conceptual framework for quantitative assessments

January 2019

A. Seiphoori

Massachusetts Institute of Technology,
Department of Earth & Atmospheric,
& Planetary Sciences, USA

KEYWORDS

Opalinus Clay, self-sealing, fracture transmissivity,
closure laws, geomechanics, microstructure, Mont Terri

**National Cooperative
for the Disposal of
Radioactive Waste**

Hardstrasse 73
P.O. Box 280
5430 Wettingen
Switzerland
Tel. +41 56 437 11 11
www.nagra.ch

Nagra Arbeitsberichte ("Working Reports") present the results of work in progress that have not necessarily been subject to a comprehensive review. They are intended to provide rapid dissemination of current information.

This report was prepared on behalf of Nagra. The viewpoints presented and conclusions reached are those of the author(s) and do not necessarily represent those of Nagra.

"Copyright © 2019 by Nagra, Wettingen (Switzerland) / All rights reserved.

All parts of this work are protected by copyright. Any utilisation outwith the remit of the copyright law is unlawful and liable to prosecution. This applies in particular to translations, storage and processing in electronic systems and programs, microfilms, reproductions, etc."

Table of Contents

Table of Contents	I
List of Tables.....	II
List of Figures	II
1 Introduction	1
1.1 Background.....	1
1.2 Objectives	1
1.3 Report outline	2
2 Self-sealing of fractures in Opalinus Clay - literature survey	3
2.1 Basic considerations	3
2.2 Formation of the EDZ fracture network	3
2.3 Hydro-mechanical behavior of fractures.....	5
2.4 Self-sealing and fracture closure Laws.....	5
2.5 Heuristic model of fracture self-sealing.....	10
3 Present study of the self-sealing of fractures in Opalinus Clay	13
3.1 Opalinus Clay material in this study.....	13
3.2 Mineralogical composition	14
3.3 Porosimetry analysis (MIP and N ₂ adsorption)	17
3.4 Pore-scale visualization	20
3.5 Interaction with in-situ pore water.....	21
4 Triaxial testing	23
4.1 Sample preparation	23
4.2 Internal fracture network	24
4.3 Calculation of the in-situ stress conditions	27
4.4 Permeability	27
4.4.1 Relationship between hydraulic conductivity and permeability.....	28
4.4.2 Fracture permeability.....	28
4.5 Triaxial testing equipment	29
4.5.1 General sample assembly	31
4.5.2 Cylindrical samples for self-sealing experiments.....	33
5 Results and discussion	37
5.1 Ar-gas fracture permeability experiments	37
5.2 Synthetic water fracture permeability experiments	44
5.3 Evolution of the internal pore structure due to self-sealing of fractures.....	50
5.3.1 Visual observations.....	50
5.3.2 Evolution of the internal pore structure (X-Ray micro-CT).....	50

6	Summary, conclusions and outlook.....	55
7	References.....	57
App. A:	Interaction of Opalinus Clay with synthetic water.....	A-1
App. B:	Steady-state Ar-gas permeability measurement in triaxial cell.....	B-1
App. C:	Steady-state water permeability measurements according to Tab. 6	C-1

List of Tables

Tab. 1:	Physical and index characteristics of Opalinus Clay (OPA)	13
Tab. 2:	XRPD bulk mineralogy (weight %) RIR method.....	15
Tab. 3:	Relative percentage of clay minerals in the < 2 μm clay size fraction	16
Tab. 4:	Synthetic pore water composition for Opalinus Clay after (Mäder 2011).....	21
Tab. 5:	Geometrical and physical properties of the tested samples in triaxial system	33
Tab. 6:	Steady-state apparent permeability measurement during triaxial self-sealing experiment.....	46
Tab. 7:	Water content and degree of saturation of the Opalinus Clay sample prior and after triaxial testing	49
Tab. A-1:	Steady-state permeability measurement of the artificially fractured Opalinus Clay sample (OPA-BCI-fractured).....	A-1

List of Figures

Fig. 1:	Conceptual models of EDZ	4
Fig. 2:	Experimental evidence of sealing effects in Opalinus Clay at Mont Terri.....	6
Fig. 3:	Mechanical and hydromechanical fracture responses under normal closure.....	7
Fig. 4:	Deformation, gas permeability and wave velocity of fractured OPA samples (Mont-Terri) to loading and unloading (Zhang 2011).	8
Fig. 5:	Comparison between the experimental fracture closure with applied normal stress and the model	9
Fig. 6:	Long-term measurements of water permeability on fractured COX and OPA samples at different temperatures	9
Fig. 7:	Schematic sketch of the conceptual framework for EDZ fracture closure in Opalinus Clay	10

Fig. 8:	Conceptual model proposed by (Fang et al. 2017) for the asperity and permeability evolution of an artificial cut fracture	11
Fig. 9:	Opalinus Clay materials in the present study were obtained from the Mont-Terri URL (BCI-21B section, depth about 300 m).	14
Fig. 10:	Mineralogical composition of the Opalinus Clay material from borehole BCI-21B, Mont Terri, studied in this research	15
Fig. 11:	XRPD Bulk Mineralogy analysis on the OPA material from the borehole BCI-21B, Mont Terri, studied in this research	16
Fig. 12:	XRPD analysis of the clay minerals in the < 2 mm clay size fraction.....	17
Fig. 13:	(a) Cumulative void ratios (e_{GH}) and (b) the pore (entrance) size distribution (PSD) functions for natural Opalinus Clay specimens in the present study	18
Fig. 14:	Adsorption-desorption isotherms of N ₂ at liquid N ₂ (-197.3 °C) temperature (STP: standard temperature).....	19
Fig. 15:	Typical microfabric of the Opalinus Clay material at Mont-Terri site (BCI and FEA sections).....	20
Fig. 16:	Time-lapse visual observation of the reaction of Opalinus Clay (BCI-21B) material with synthetic pore water, and fast disintegration of the material due to hydration and swelling.....	22
Fig. 17:	Hexagonal prism prepared using the wire-saw is cut into cylindrical samples by employing a mechanical lathe as demonstrated in (b) and (c).....	23
Fig. 18:	(a) Creation of the artificial fracture plane using an abrasive wire saw, (b) intact and artificially cut samples.....	23
Fig. 19:	X-Ray micro-CT analysis of a p-sample of Mont-Terri Opalinus Clay (BCI section), where the isolated pore channels along the bedding plane can be observed.....	24
Fig. 20:	The bright grains are either the carbonate calcium particles or the calcareous fossil tests across the bedding plane of the material	25
Fig. 21:	Enhances pore channel along the bedding and in the proximity of the non-clay particles and particularly the fossils.....	25
Fig. 22:	A cross section which is free of any pore channels or fractures along the bedding plane	26
Fig. 23:	Presence of irregular pore-channels along the bedding plane which are likely the pathways for flow and particle transport along the bedding of Opalinus Clay material	26
Fig. 24:	High-pressure triaxial cell parts and the fully instrumented sample.....	29
Fig. 25:	Schematic layout of the advanced triaxial testing equipment in the study of self-sealing fracture of Opalinus Clay material.....	30
Fig. 26:	The sample assembly prior to the triaxial experiment and the installation of the strain gauges and acoustic sensors.....	32
Fig. 27:	Spalling of the material from the fracture wall.....	34
Fig. 28:	Cylindrical sample for self-sealing triaxial experiment.....	34

Fig. 29:	Instrumentation map on the artificially fractured sample jacketed for triaxial testing	35
Fig. 30:	Variation of the total isotropic pressure, pore gas (Ar) pressures at top and bottom of the sample and the effective pressure with respect to time	37
Fig. 31:	Variation of the aperture displacement measured using the LVDT positioned in the direction normal to the fracture plane	38
Fig. 32:	Aperture change measured by the LVDT installed normal to the fracture plane with respect to the cycles of the applied effective pressure	38
Fig. 33:	Ar-gas apparent permeability of the artificially fractured Opalinus Clay sample	39
Fig. 34:	Ar-gas permeability of the intact Opalinus Clay sample as a function of the applied isotropic effective pressure for one cycle of loading and unloading	39
Fig. 35:	Variation of the p-wave velocities recorded during the gas permeability using p-wave piezoelectric sensors 1 and 2 as shown in Fig. 28	40
Fig. 36:	Variation of the radial strain recorded at gauge#1 (ϵ_{R1} in milli-strain).....	41
Fig. 37:	Variation of the axial strain recorded at gauge#1 (ϵ_{A1} in milli-strain).....	41
Fig. 38:	Variation of the axial strain recorded at gauge#2 (ϵ_{R2} in milli-strain).....	42
Fig. 39:	Variation of the axial strain recorded at gauge#1 (ϵ_{A2} in milli-strain).....	42
Fig. 40:	Variation of the total volumetric strain using data of the recorded axial and radial strain at gauge#1 (in milli-strain) positioned on the material's matrix.....	43
Fig. 41:	Variation of the difference in records of the radial strain at gauges #1 and 2 defined as ϵ_{ap} as an indication for the aperture strain of the artificial fracture.....	43
Fig. 42:	Variation of the pore water volume and pore pressure applied to the bottom and top of the sample in triaxial experiment	44
Fig. 43:	Variation of the pore volume top and bottom during the steady-state permeability measurement described in Fig. 42	45
Fig. 44:	(a) Change of the apparent permeability over time during the water flow through the fracture	45
Fig. 45:	Stress path applied on the artificially fractured sample immediately after gas experiment.....	46
Fig. 46:	Variation of the swelling displacement measured using the LVDT positioned normal to the fracture plane for a constant effective pressure over time	47
Fig. 47:	Variation of the radial strain (in milli-strain) measured using the strain gauge installed on the fracture position (see Fig. 29).....	48
Fig. 48:	Variation of the axial strain (in milli-strain) positioned in the proximity of the fracture position (see Fig. 29).....	48
Fig. 49:	Variation of the swelling deformation recorded by the LVDT and the pore volume difference ($v_b - v_t$)	49

Fig. 50:	(a), (b) Initial fracture plane after preparing the artificially fractured sample of the Opalinus Clay; and (c), (d) final fracture plane after triaxial self-sealing experiments, where the swelling and filling the initial gaps can be observed (see Fig. 27)	50
Fig. 51:	Process of self-sealing of the fractures in Opalinus Clay sample after triaxial experiments detailed in Section 5.2.....	51
Fig. 52:	Range of the pores visualized with the X-Ray micro-CT tomography technique compared with the MIP data for the intruded porosity with respect to the pore entrance size	51
Fig. 53:	Internal 3D pore structure of the Opalinus Clay sample (with artificial fracture plane) at initial condition reconstructed from the X-Ray micro-CT data before testing under triaxial condition.....	52
Fig. 54:	Internal 3D pore structure of the Opalinus Clay sample (with artificial fracture plane) after self-sealing experiment with synthetic pore water.....	52
Fig. 55:	A comparison between the internal 3D pore structure of the Opalinus Clay sample (with artificial fracture plane)	53
Fig. A-1:	Time-lapse visual observation of the reaction of Mont Terri OPA	A-1
Fig. A-2:	Time-lapse visual observation of the reaction of Schlattingen OPA.....	A-2
Fig. C-1:	Permeability versus time during the steady-state measurement of the synthetic water permeability during the self-sealing experiment on sample OPA-BCI-fractured	C-1

1 Introduction

1.1 Background

As part of reporting for Stage 2 of the Sectoral Plan for Deep Geological Repositories (SGT), Nagra has documented the comprehensive hydrogeological and geomechanical data base and derived reference parameters for the assessment of long-term safety and engineering suitability of a deep geological repository in Opalinus Clay (Nagra 2014a,b). In this context, the current understanding of self-sealing of the fractures in Opalinus Clay has been documented, the effect on the fracture transmissivity and bulk permeability of the material was evaluated and a conceptual framework for the numerical simulation of self-sealing processes in clay-rich rock was given. Preliminary experimental evidence for the impact of compaction on the evolution of hydraulic conductivity of the Opalinus Clay was derived by laboratory tests on intact and reconstituted core samples from Mont Terri and Schlattingen, respectively (Favero et al. 2016). Since that time, complementary laboratory experiments have been launched, aimed at broadening the mechanistic understanding of self-sealing processes in fractured claystone and increasing the experimental data base. This report complements previous studies, emphasising the hydro-mechanical behavior of intact and fractured Opalinus Clay in response to stress changes in the context of a multiscale study of the pore structure and hydro-mechanical properties. The research was performed at the Massachusetts Institute of Technology (MIT) and the University of Pennsylvania (UPenn), closely coordinated with a project on the effects of burial diagenesis on Opalinus Clay behavior (Seiphoori 2019).

1.2 Objectives

The capacity of clay-rich host rocks to self-seal excavation induced fractures and tectonic fractures is of high significance in the context of long-term safety. This report details a systematic study of the self-sealing of fractures in Opalinus Clay and its effect on the fracture permeability behavior of the material. Opalinus Clay samples from Mont Terri (borehole BCI-21B) were subjected to a comprehensive laboratory programme, aimed at broadening the mechanistic understanding of self-sealing processes with particular focus on:

- the geotechnical characterization of the core samples in terms of mineralogical composition and hydro-mechanical properties
- the collection of phenomenological evidence of self-sealing processes in Opalinus Clay on a spatial scale ranging from nm to cm
- the derivation of functional relationships, describing the aperture-transmissivity behaviour of fractures in clay-rich materials in response to stress stress-paths of potential relevance for a deep geological repository

This research is intended to improve our understanding of flow and transport processes along the Excavation Damaged Zone (EDZ) of the backfilled structures of a radioactive waste repository. Furthermore, it contributes to the assessment of transport processes (e.g., volatile and dissolved radionuclides) along discrete tectonic features in the repository nearfield. Our study is an innovative research to investigate the self-sealing potential of claystones in general, and the Opalinus Clay in particular.

1.3 Report outline

The report first surveys the existing literature about self-sealing of fractures in Opalinus Clay and presents key results of previous investigations (Chapter 2).

In Chapter 3 the mineralogy and microstructural features of the tested material are characterised and the origin of the material is referenced.

Chapter 4 is dedicated to triaxial testing. Sample preparation and experimental devices are described in detail.

The results of the laboratory investigations are presented in Chapter 5.

Chapter 6 summarises the results and draws the conclusions about the significance of self-sealing in fractured Opalinus Clay.

2 Self-sealing of fractures in Opalinus Clay - literature survey

2.1 Basic considerations

In Opalinus Clay formation with very low intrinsic matrix permeability ($\sim 10^{-19}$ to 10^{-21} m²), the fluid flow and transport of dissolved matter takes place predominantly through tectonic and excavation induced fracture systems. Therefore, the Excavation Damaged Zone (EDZ) around the backfilled underground structures of a geological repository represents a release path for radionuclides, which needs to be addressed in the long-term safety assessment of radioactive wastes repositories (Mazurek et al. 2008, Bossart 2018, Marschall et al. 2018). On the other hand, the EDZ may also perform as a highly efficient escape route for the gases associated with corrosion and degradation of wastes and thus limit the gas overpressures in the backfilled repository structures (Johnson et al. 2004, Diomidis 2016). The efficiency of such release paths depends not only on the geometry of the EDZ (Popp et al. 2008), but also on the "self-sealing" capacity of the host rock formation and the prevailing stress state conditions, such as in-situ stresses and the pore pressure (Neuzil 1994, Bossart et al. 2002, Deming et al. 2002, Lanyon & Senger 2011). The formation and temporal evolution of the EDZ is highly controlled by the complex hydro-chemo-mechanical coupled processes at the repository location. For the long-term safety assessment of a repository, in-depth understanding, comprehensive characterization, and mechanistic process models of the self-sealing process of the EDZ are essential (Bock et al. 2010). Simplified fracture closure models, able to mimic the safety-relevant functional features of the EDZ in a traceable manner are indispensable for the simulation of flow and transport processes along the EDZ with the goal of capturing the evolution of hydraulic significance of the EDZ after closure of the backfilled underground structures.

2.2 Formation of the EDZ fracture network

Excavation of an underground repository for disposal of radioactive waste in an argillaceous formation generates damaged zones with significant irreversible modification in their flow and transport properties such as an increasing permeability by two or more orders of magnitude (Tsang et al. 2005). This zone around the underground structure is referred to as excavation damage zone (EDZ) (Fig. 1-a). The creation and evolution of the EDZ around the openings is controlled by several factors, including the hydro-mechanical state conditions (e.g., stress, pore pressure, temperature), engineering design (e.g., configuration of the underground structures, size and shape of tunnel cross-sections, excavation technique, support system/lining) and the impacts on the system during the operational phase (e.g., ventilation, waste emplacement) (Tsang et al. 2005, Alheid et al. 2007, Mazurek et al. 2008). The deformation behavior is further complicated, amongst others, by (i) rock anisotropy (stiffness and strength), (ii) spatial variability of rock fabric (facies variability and tectonic features) and (iii) clay-specific hydro-mechanical couplings, giving rise to long-lasting time-dependent processes in the EDZ even after closure of the backfilled repository structures (Mazurek et al. 2008). The inventory of brittle EDZ features (i.e., caused directly by the short-term excavation-induced unloading and loading) includes extensional fractures, spalling and buckling of the bedding planes, interactions with the existing tectonic features, bedding slip, single shear fractures and shear-bands (Marschall et al. 2006, Mazurek et al. 2008). Far reaching bounding shear bands delimit the EDZ and the intact rock zones (Blümling et al. 2007).

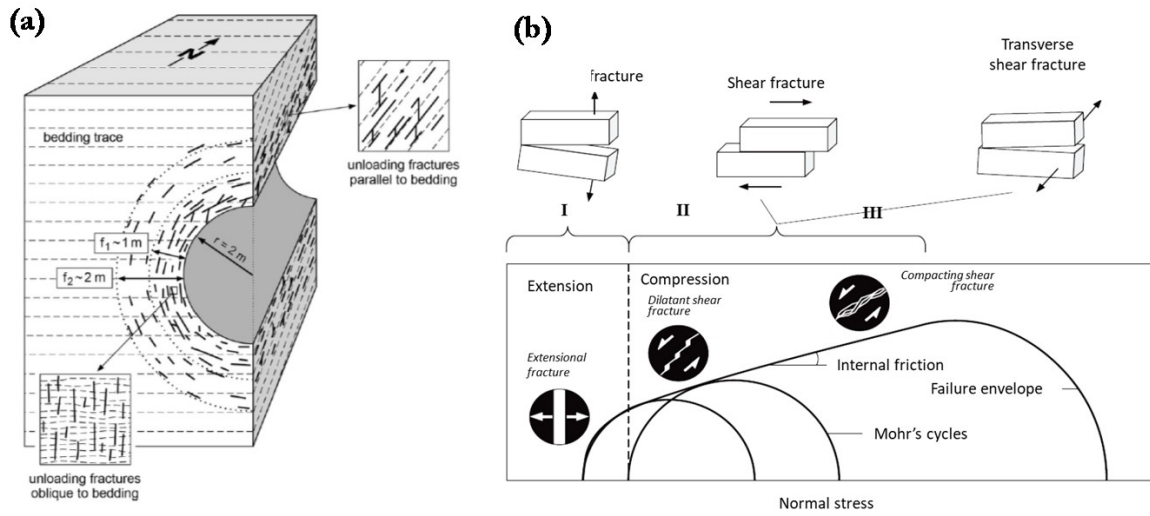


Fig. 1: Conceptual models of EDZ
 (a) radial distribution of extensile fracturing within EDZ, (b) classification of EDZ fractures from the fracture mechanics viewpoint

Further EDZ features can be associated with the operational phase, such as desiccation cracks in response to tunnel ventilation and swelling-induced disaggregation of the rock matrix, when subjected to water-based fluid (Mazurek et al. 2008). The weakening of the EDZ during the operational phase is associated predominantly with time-dependent ductile failure, gravity driven mechanisms, also termed "creep" (Sone & Zoback 2011, Kohli & Zoback 2013), going along with a gradual loss of cohesion in the rock matrix and the development of fault gouges along fracture planes. Slow creep deformation can occur along the transmitting fracture surface, where a high fraction clay or organic materials is present (Abouelresh & Slatt 2012). From a fracture mechanics point of view, the EDZ fractures may be classified as extensional fractures in the regime of very low mean effective stress (Fig. 1-b mode 1), dilatant shear fractures at moderate mean effective stress (Fig. 1-b mode 2 & mode 3) and compacting shear fractures at high effective stress (Fig. 1-b mode 2 & mode 3). An insight into the fracture pattern evolution using advanced visualization techniques including the X-Ray Micro-Computed Tomography (Micro-CT) and Scanning Electron Microscopy (SEM) can provide information on the fracture classes in Opalinus Clay.

2.3 Hydro-mechanical behavior of fractures

The hydro-mechanical fracture properties of fractured rocks can be categorized in two groups of mechanical and hydraulic properties. The mechanical behavior of typical rock materials is often characterized by measuring the displacement (closure) of the fracture surfaces as a function of the applied normal load. The fracture stiffness is then defined as the ratio of the change in stress to the change in fracture aperture (Goodman et al. 1968). On the other hand, the hydraulic properties are referred to as the fracture transmissivity or permeability (Zimmerman & Main 2004). Fracture permeability experiments conducted on various rock types, including the natural and artificial fractures, concluded some major, consistent observations (Gale 1982, Raven & Gale 1985, Hofmann et al. 2016), as summarized by Hofmann et al. (2016):

- fracture transmissivity decreases with increasing confining stress
- fracture transmissivity decreases with time due to an inelastic deformation of asperities and gouge production (fracture creep)
- fracture transmissivity decreases with cyclic loading/unloading and waiting time between cycles, where at least two to three cycles are required before the hysteresis effects normally become negligible

A study of the relevant literature indicates that the hydro-mechanical fracture behavior of claystone formations in general (Zhang 2011, 2013, Giot et al. 2018), and the Opalinus Clay in particular under controlled triaxial stress condition has received limited attention. The swelling of the clay matrix due to water-based fluid is expected to play a significant role in the fracture permeability behavior of the material with large clay content. An active fracture can affect the transmissivity of the fluid under a given stress condition by sealing the fracture gaps during the hydration and swelling of the clay matrix. We expect a strong coupling between the swelling potential and the transmissivity behavior; a mechanism arising from a competition between the strength of the diagenetic cementation bonds and the clay matrix swelling potential during hydration.

2.4 Self-sealing and fracture closure Laws

The dependence of fracture gas transmissivity on the effective normal stress in claystones including the Opalinus Clay has been investigated experimentally by several researchers (Blümling et al. 2007, Zhang 2011, 2013). In addition, as a part of the Gasfrac Self-sealing (GS) experiments at the Mont Terri Lab, hydraulic tests were conducted before and after a combined hydro- and gas-frac experiments (Marschall et al. 2005). The experiment was carried out in a test interval containing a hydrofrac with a well-defined fracture geometry. Interval transmissivity increased by 5 – 6 orders of magnitude when the injection pressure exceeded the effective normal stress on the fracture plane (Fig. 2). For low injection pressures, however, the interval transmissivity was close to that of the intact rock ($T \leq 10^{-12}$ m²/sec). These findings can be explained by the dependence of fracture transmissivity (or hydraulic conductivity) on the effective normal stress, which follows a hyperbolic fracture closure law. An effective mechanical self-sealing of the artificial fracture is observed already at moderate effective normal stresses in the order of 1 – 2 MPa (Fig. 2).

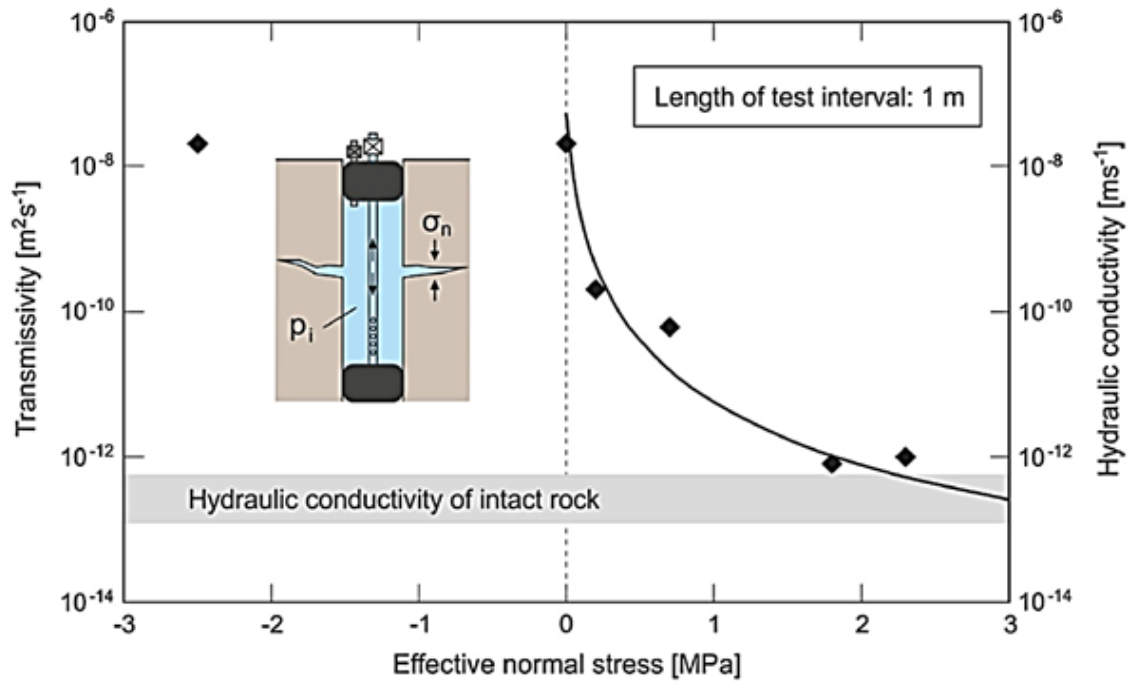


Fig. 2: Experimental evidence of sealing effects in Opalinus Clay at Mont Terri
 Suggested hyperbolic relationship between interval transmissivity and effective normal stress, based on the investigation of fracture closure mechanisms in the Gasfrac self-sealing (GS) experiment (Marschall et al. 2005)

The fracture closure can be modeled by hyperbolic functions such as those proposed by Goodman (Goodman 1976) and Bandis et al. (Bandis et al. 1983) or by exponential models employed for the compaction of backfill materials (Bock et al. 2010). The fractures also feature a hysteresis behavior arising from the surface mismatch, sampling disturbance and crushing of asperities (Barton et al. 1985). Several empirical models were developed and applied for normal closure behavior. The first nonlinear joint model is Goodman's hyperbolic form:

$$\Delta u_n = \frac{\sigma'_{ni}}{K_{ni}} \left(1 - \frac{\sigma'_n}{\sigma'_{ni}} \right) \tag{Equation 1}$$

where Δu_n is joint normal displacement, and K_{ni} and σ'_{ni} are normal stiffness and effective normal stress at an initial reference stage. The most commonly applied joint model is Bandi's hyperbolic function (Bandis et al., 1983):

$$\delta = \frac{\sigma'_n}{K_{n0} + \sigma'_n / \delta_{max}} \tag{Equation 2}$$

where δ is current normal closure, δ_{max} is maximum normal closure, and K_{n0} is normal stiffness at the zero-stress intercept as shown in Fig. 3 adopted from (Rutqvist & Stephansson 2003). The basic parameters K_{n0} and δ_{max} can be estimated from Barton-Bandis basic joint parameters, joint roughness coefficient (JRC_0), and joint compressive strength (JCS_0) using empirical relationships (Barton et al. 1985).

The second most commonly used model is the logarithmic type, mostly applied in hot-dry rock geothermal-reservoirs (Rutqvist & Stephansson 2003). The logarithmic model can be written as (Evans et al. 1992):

$$\Delta u_n = -\frac{1}{\left(\frac{dk_n}{d\sigma'_n}\right)} \ln\left(\frac{\sigma'_n}{\sigma'_{n0}}\right) \quad \text{Equation 3}$$

The parameter $(dk_n/d\sigma'_n)^{-1}$, which Evans et al. (1992) termed as "stiffness characteristics", can be estimated theoretically from Hertz's analysis of deformation for two fracture surfaces containing linear elastic hemispheres in contact (Rutqvist & Stephansson 2003). In general, the hyperbolic Equations (Equation 2) has been shown to match mated fractures better whereas the logarithmic Equations (Equation 3) represents unmated fractures better.

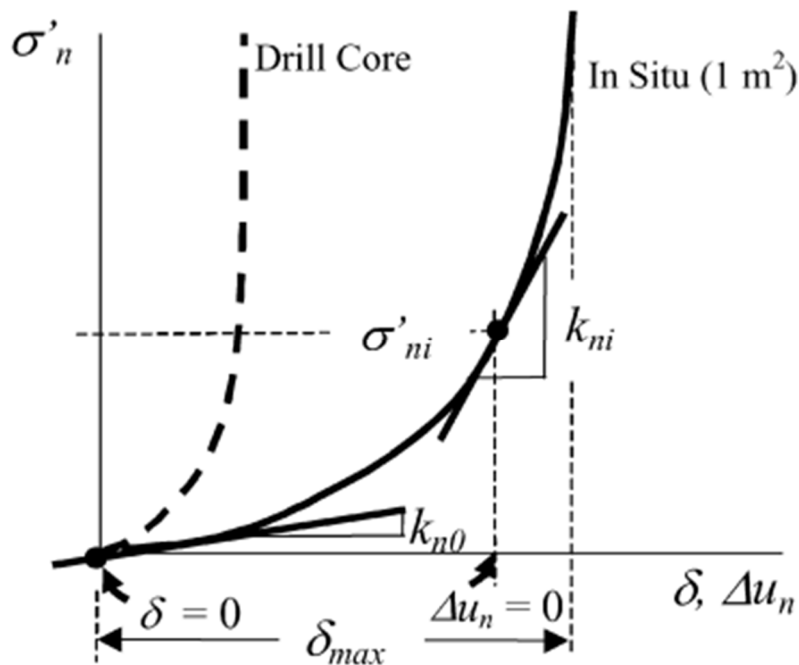


Fig. 3: Mechanical and hydromechanical fracture responses under normal closure

Effect of sample size is indicated with the laboratory sample response (dashed lines) compared with in-situ fracture response (1-m² size) from (Rutqvist & Stephansson 2003).

Zhang (2011) investigated the self-sealing of fractures on heavily fractured cylindrical specimens from the Callovo-Oxfordian (COX) argillite and the Opalinus Clay (OPA) materials on hollow-cylinder samples. N₂ gas and synthetic water was applied under a confining stress up to 15 MPa and temperature varying from 20 to 90 °C. The p-wave velocity, permeability and deformation were measured continuously to provide information on the self-sealing behavior of the studied materials. A significant sealing process of the fractures was observed with fracture closure and permeability decrease to levels of 10⁻¹⁹–10⁻²¹ m² within months to years. First, the sealing of fractures under compression loading and without water was studied as shown in Fig. 4. Zhang proposed an exponential model for the description of the normal stress–fracture closure as follows:

$$\Delta b = b_m(1 - e^{-\alpha\sigma_n^\beta}) \tag{Equation 4}$$

where Δb is the aperture closure, b_m is the maximum aperture closure (equal to the initial aperture), σ_n is the normal stress, α and β are material parameters. The proposed model along with experimental data of fracture closure along the loading path with $\alpha = 0.48$ and $\beta = 0.3$ for an aperture ($b_m=0.6$ mm) in a Mont-Terri Opalinus Clay sample is shown in Fig. 5 (the blue curve). The material parameters depend on the amplitude and distribution of the aperture, surface roughness, contact area, deformability and strength of asperities and vary from one sample to another.

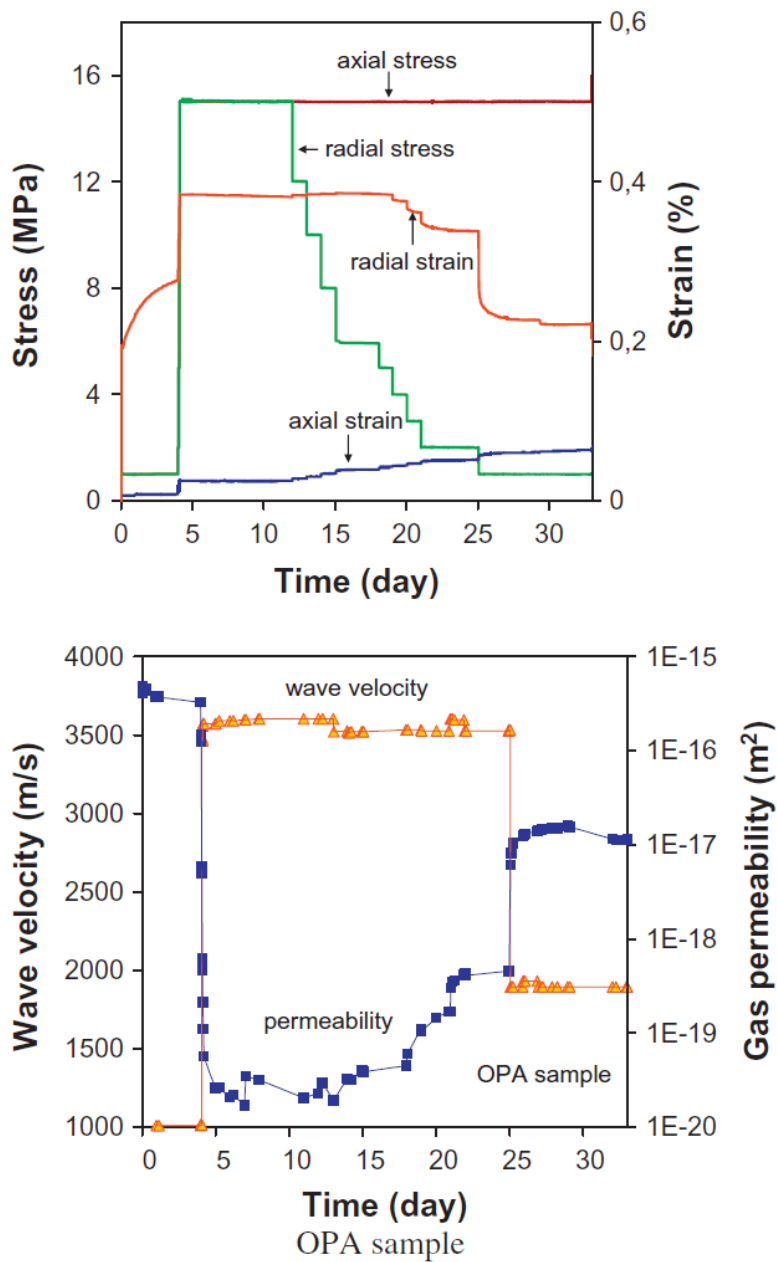


Fig. 4: Deformation, gas permeability and wave velocity of fractured OPA samples (Mont-Terri) to loading and unloading (Zhang 2011).

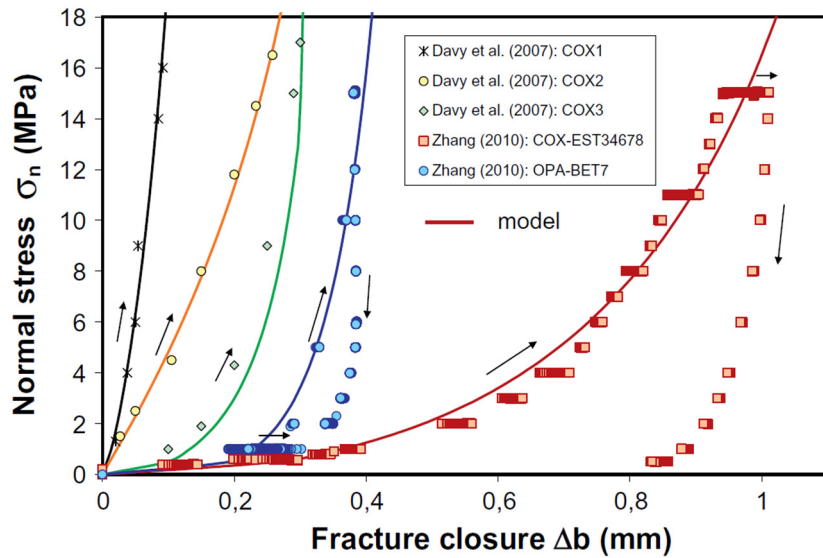


Fig. 5: Comparison between the experimental fracture closure with applied normal stress and the model

Proposed by Zhang (2011) during N₂ gas permeability experiment on different claystone materials. Data from (Davy et al. 2007) is also presented in this plot.

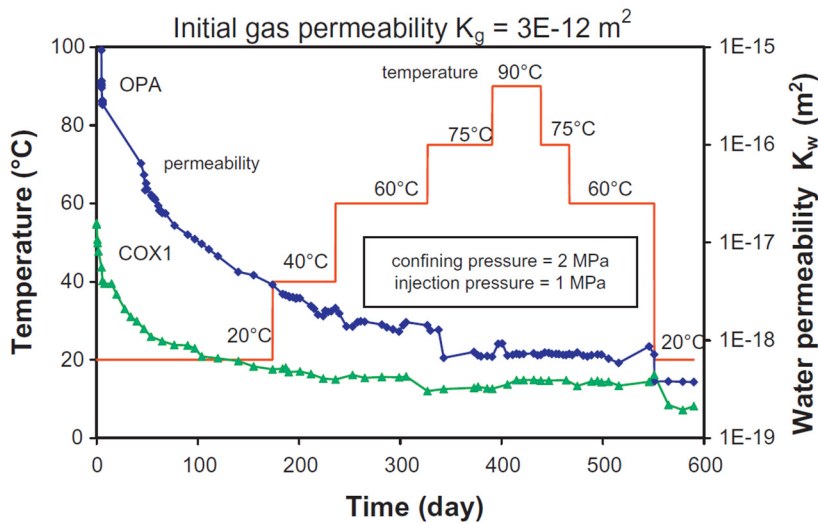


Fig. 6: Long-term measurements of water permeability on fractured COX and OPA samples at different temperatures (from Zhang 2011).

Zhang (2011) investigated the thermal impacts on the sealing of fractures in both materials by heating the fractured samples (50 × 100 mm) under a confining stress of 2 MPa and pore pressure of 1 MPa as shown in Fig. 6. The permeability of both materials decreases gradually up to a very low value of 10⁻¹⁸ – 10⁻¹⁹ m² by increasing the temperature; however, after reaching a certain region, the temperature effect seems negligible (see Zhang 2011 for further discussion of the experimental results).

2.5 Heuristic model of fracture self-sealing

Marschall et al. (2018) presented a conceptual framework for EDZ fracture closure in Opalinus Clay (Fig. 7). It is stated that the hydraulic significance of the EDZ during tunnel construction and its evolution during the operational phase and after backfilling of the underground structures can be formulated in terms of a heuristic EDZ closure model. Creation of the EDZ is a brittle process, i.e., the increase of the void volume of the damaged rock zone around the excavation is solely attributed to the fracture opening, whereas the porosity of non-fractured rock domains remains essentially unchanged during the early times. Initially, the newly created EDZ fractures are unsaturated and exposed to atmospheric pressure, whereas the non-fractured rock domains remain saturated and exhibit a low matrix suction as a consequence of the high gas entry pressure of the Opalinus Clay. The initial transmissivity of the unsaturated EDZ fractures is controlled by the fracture aperture and can be very high. The matrix hydraulic conductivity remains essentially unchanged, i.e. is the same as the conductivity the intact rock. The matrix suction in the rock matrix decreases over time due to the uptake of pore water from outer rock zones and the fractures start to resaturate. Porewater uptake of the non-fractured rock zones is associated with swelling and consequently with an increase of matrix porosity.

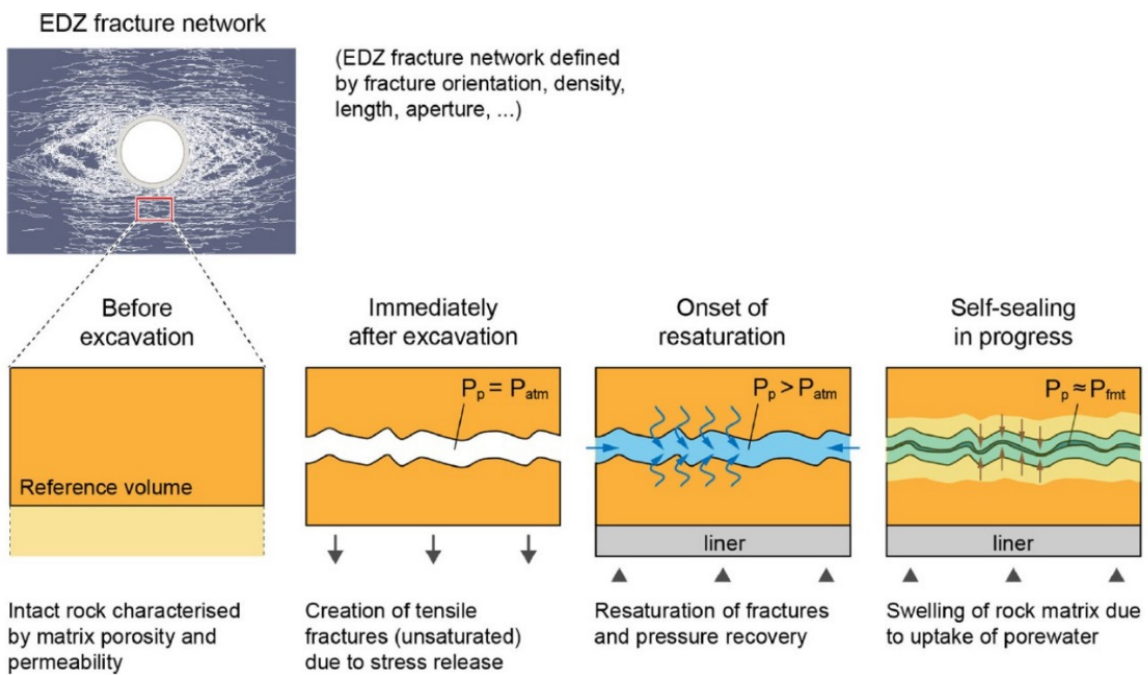


Fig. 7: Schematic sketch of the conceptual framework for EDZ fracture closure in Opalinus Clay

Covering the key phenomena and features from the early post excavation phase until static formation pressure recovery (Marschall et al. 2018)

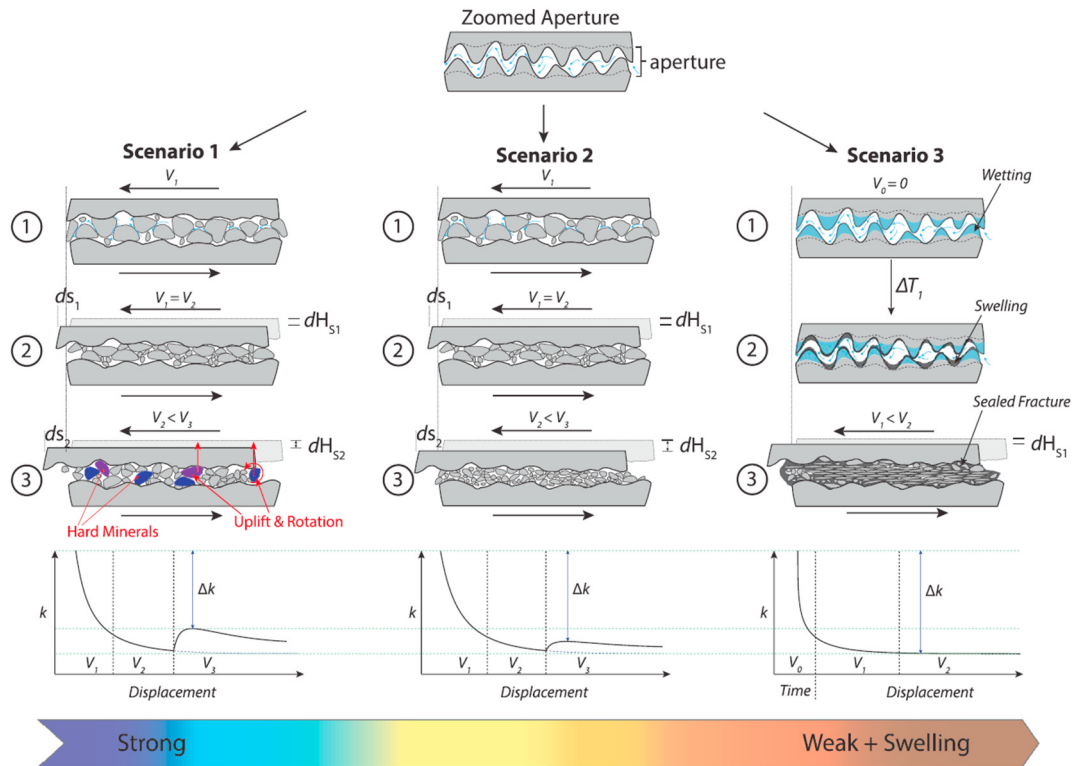


Fig. 8: Conceptual model proposed by (Fang et al. 2017) for the asperity and permeability evolution of an artificial cut fracture

Scenario 1: End-member of clay-poor, brittle-like fracture material composed of hard minerals. Scenario 2: Intermediate case between clay-poor and clay-rich end-members. Scenario 3: End-member of clay-rich and weak-ductile fracture material that is composed of soft minerals

This porosity increase of the rock matrix happens at the expense of the fracture aperture, i.e. the fractures start to close and fracture transmissivity reduces drastically, whereas the hydraulic conductivity of the non-fractured matrix zones increases slightly as a consequence of the porosity increase. This process of porosity and conductivity increase of the matrix is associated with the decrease of fracture aperture and transmissivity progresses until the effective stress reaches the equilibrium. This is essentially the case, when pore pressure reaches the static pressure of the formation (Marschall et al. 2018).

To understand the mode of fracture reactivation and permeability evolution, Fang et al. (2017) conducted direct-shear experiments to measure the frictional strength and stability of Opalinus Clay (Clay rich formation (OPA); Mont Terri, BEZ-G50 section) and Green River shale (Carbonate rich formation (GRS), Grand Junction, Colorado) along the permeability. They observed that under a low effective normal stress, the OPA exhibited weaker frictional strength but stronger frictional stability and a larger permeability reduction than the GRS. They proposed three interconnected physical mechanisms for their observations (Fig. 8): (1) the hard minerals are difficult to comminute into small particles during the shearing, and the fracture may dilate significantly; (2) the fracture material is brittle and contains weak minerals that can be crushed into fine particles and compacted with shear displacement; and (3) the material contains soft minerals readily deform and comminute into smaller particles under the applied shearing, and fill the channel. By further infiltration of the fluid, the clay matrix swelling forms a thin layer of clay-rich foliae that seals the fracture.

3 Present study of the self-sealing of fractures in Opalinus Clay

Here, we detail the physical and geomechanical properties of the tested Opalinus Clay material in this study followed by introducing the advanced microstructural, porosimetry, visualization and hydro-mechanical triaxial testing techniques employed to characterize the self-sealing properties of the Opalinus Clay. The results and discussions are presented after introducing the techniques.

3.1 Opalinus Clay material in this study

Opalinus Clay is a sedimentary formation which can be classified as a claystone based on its mineralogical composition and a clayey siltstone based on its particle size analysis (Nagra 2014). It was formed approximately 174 – 170 million years ago in a marine environment, and was subjected to burial, uplift and erosion processes (Mazurek et al. 2006, Gradstein et al. 2012). Opalinus Clay materials were obtained from the Cement-clay Interaction (CI) experimental site of the Mont Terri Underground Research Laboratory as demonstrated in Fig. 9. The Mont Terri URL is located in the Jura Mountains of the north-western Switzerland at a depth of approximately 250 to 300 meters. The borehole BCI in Gallery 98 is located in the clay-rich facies of the Opalinus Clay formation (Freivogel et al. 2003). The Mont Terri Opalinus Clay was deposited in the Aalenian, and was subjected to two successive stages of burial (in the Cretaceous and Tertiary) with a maximum burial depth of about 1'350 m during Cretaceous, and 1'000 m during Miocene (Mazurek et al. 2006). Tectonic events during Alpine orogeny resulted in tilting and uplift of the claystone strata, and in combination with erosion, cause the current state of over-consolidation (Bock 2000). The basic physical and geotechnical index characteristics of the Opalinus Clay are summarized in Tab. 1.

Tab. 1: Physical and index characteristics of Opalinus Clay (OPA)

Material	OPA-BCI
In-situ depth (m)	~ 300
Max. estimated depth (m)	~ 1'350
Specific gravity, G_s	2.75
Water content, w (%)	6.95
Degree of saturation, S_r (%)	95.56
ρ^* (g/cm ³)	2.44
Void ratio	0.20
Porosity, n	0.17
Zeta potential ζ^{**} (mV)	-17.0 ± 0.5

* ρ is the density of the Opalinus Clay (BCI section) measured immediately after opening the main core sample.

** Zeta potential was measured on suspended pulverized material (< 25 μ m) in deionized water. The measurement was conducted for further analysis for the effect of ionic strength on the Opalinus Clay particles surface charge.

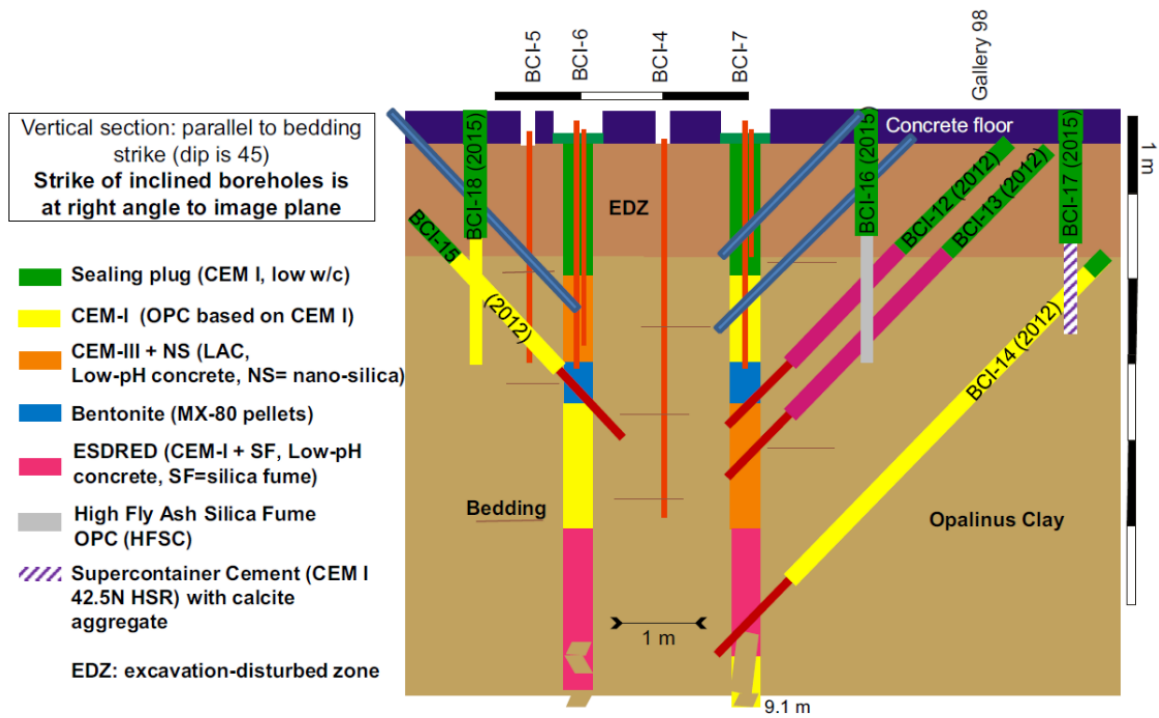


Fig. 9: Opalinus Clay materials in the present study were obtained from the Mont-Terri URL (BCI-21B section, depth about 300 m).

The CI (cement-clay interaction) experiment is located in the HE-D niche adjacent to Gallery-98 that was excavated in 1998 (Bossart 2018, Mäder et al. 2018)

The specific gravity was measured using ASTM D854, while average porosity ($n = 0.17$; void ratio $e = 0.20$) was obtained by a liquid displacement technique using a non-polar liquid (Seiphoori et al. 2017). Atterberg limits were also analyzed using ASTM D4318 (Tab. 1). Note that the void ratio is $e = wG_s/S_r$ and $n = e/(1+e)$, where w is the water content, G_s is the specific gravity (as in Tab. 1) and S_r is the degree of saturation.

3.2 Mineralogical composition

X-Ray Powder Diffraction (XRPD)

We performed the bulk and < 2 micron clay fraction mineralogical analysis by X-Ray powder diffraction (XRPD). The bulk sample was wet ground (in ethanol) in a McCrone mill and spray dried to produce a random powder. The X-Ray powder diffraction (XRPD) pattern was recorded from $2 - 75^\circ 2\theta$ using Cobalt $K\alpha$ radiation. Quantitative analysis was done by a normalised full pattern reference intensity ratio (RIR) method. Unless stated otherwise, expanded uncertainty using a coverage factor of 2, i.e. 95 % confidence, is given by $\pm X0.35$, where X = concentration in wt.-%, e.g. 30 wt.-% ± 3.3 . Note also that for phases present at the trace level (< 1 %) there may also be uncertainty as to whether or not the phase is truly present in the sample. This is both phase and sample dependent. It arises because at trace concentrations identification is often based on the presence of a single peak and the judgement of the analyst in assigning that peak to a likely mineral. The clay fraction of < 2 μ m was obtained by timed sedimentation, prepared as an oriented

mount using the filter peel transfer technique and scanned from 2 – 45° 2θ in the air-dried state, after glycolation, and after heating to 300 °C for one hour. Clay minerals identified were quantified using a mineral intensity factor approach based on calculated XRPD patterns. Unless otherwise stated, for clay minerals present in amounts > 10 wt.-% uncertainty is estimated as better than ± 5 wt.-% at the 95 % confidence level. The XRPD patterns are identified by a lab-code and by a name based on customer supplied identifiers, plus the suffix 'A' for Air-Dried, 'G' for ethylene glycol treated, 'H3' for heated to 300 °C and 'B' for bulk sample.

Tab. 2: XRPD bulk mineralogy (weight %) RIR method

Quartz	15.3	Pyrite	2.4
Plagioclase	1.2	Anatase	0.5
K-feldspar	2.2	Muscovite	5.3
Calcite	4.4	I+I/S-ML	47.2
Dolomite	0.7	Chlorite (Tri)	2.4
Siderite	0.2	Kaolinite	18.2

Chlorite(Tri) = trioctahedral chlorite
 I+I/S-ML = illite+illite/smectite – mixed layered

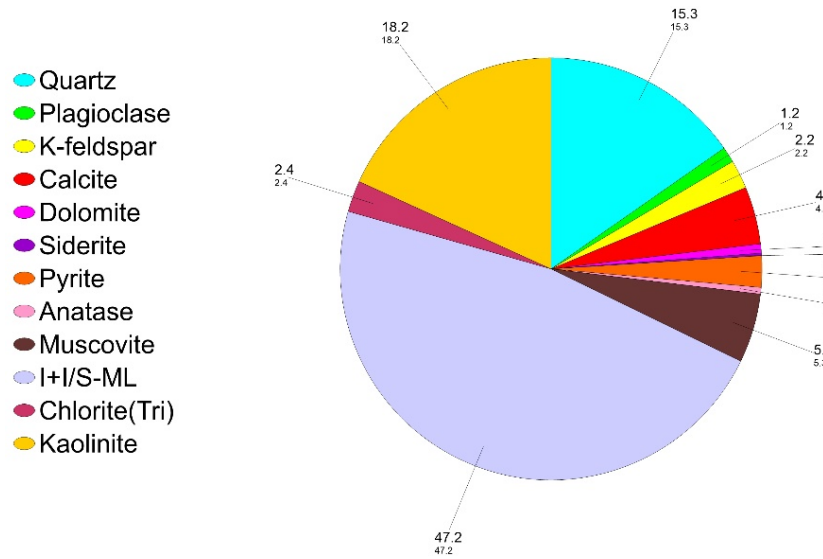


Fig. 10: Mineralogical composition of the Opalinus Clay material from borehole BCI-21B, Mont Terri, studied in this research

Tab. 3: Relative percentage of clay minerals in the < 2 µm clay size fraction

Chlorite(Tri)©	3
Kaolinite©	13
Illite©	8
I/S-ML©	76
%Exp©	25

I/S-ML© = illite/smectite mixed-layer clay
 Chlorite(Tri) = trioctahedral chlorite

The bulk XRPD results are presented in Tab. 1 and clay fraction results are in Tab. 2 and Fig. 10. The XRPD pattern, with the main non-clay phases identified in the bulk samples by reference to patterns from the International Centre for Diffraction Database (ICDD), is provided for reference. The sample is a mixture of undifferentiated illite plus illite/smectite, kaolinite, quartz, plagioclase, K-feldspar, calcite, dolomite, siderite, pyrite, muscovite, anatase and chlorite. The < 2 micron clay fraction is predominantly mixed-layer illite/smectite with kaolinite and smaller amounts of illite and chlorite. The expandability of the mixed-layer illite/smectite is estimated as approximately 25 %. Note that the expandability refers to the basal spacing in clay mineral structure where a nonexpanding 10-Å material is a discrete illite.

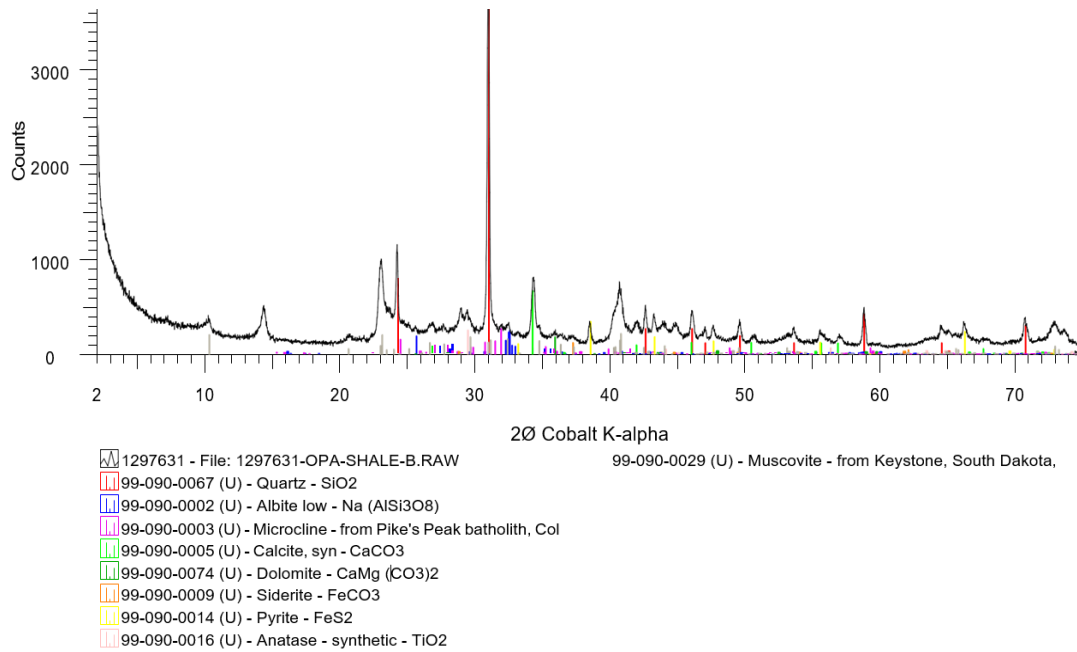


Fig. 11: XRPD Bulk Mineralogy analysis on the OPA material from the borehole BCI-21B, Mont Terri, studied in this research

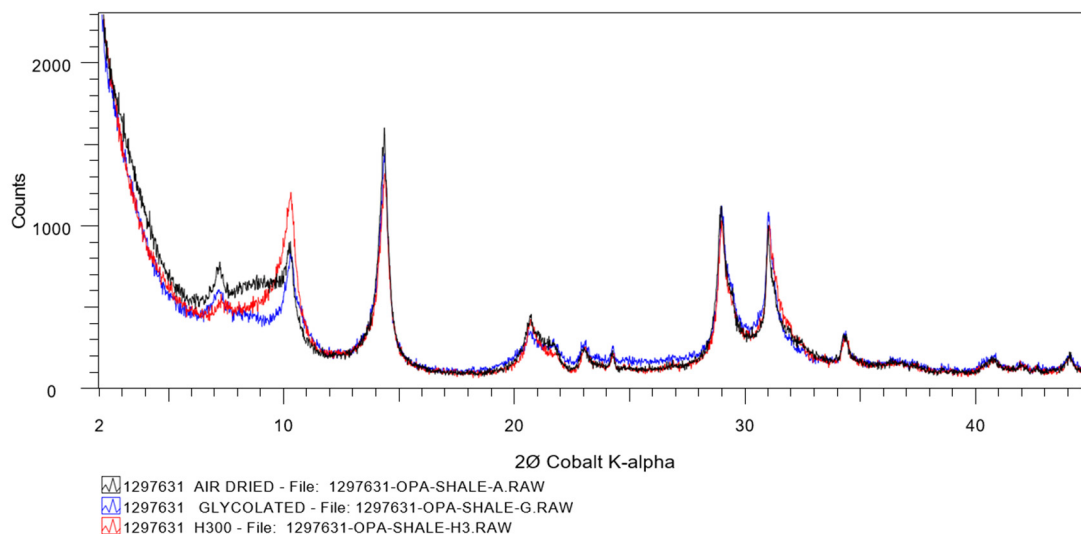


Fig. 12: XRPD analysis of the clay minerals in the < 2 mm clay size fraction

3.3 Porosimetry analysis (MIP and N₂ adsorption)

MIP provides direct quantitative information on the pore structure and transport properties of Opalinus Clay. Fig. 13 summarizes MIP measurements of the cumulative void ratio, versus the pore throat diameter, d , for two specimens from the same core. Touret et al. (1990) suggested that the clay intra-aggregate pores are in the range $\sim 0.1 - 0.2 \mu\text{m}$, while inter-aggregate pores are in the range $\sim 0.2 - 3 \mu\text{m}$ (Touret et al. 1990). Similarly, Kuila and Prasad (2013) characterize the intra-aggregate porosity of a mixed illite and smectite clay for pores less than $0.1 \mu\text{m}$. In the present study, an equivalent pore diameter, $d = 0.10 \mu\text{m}$ was assumed as a partition threshold to distinguish between inter-cluster and intra-cluster pores within the Opalinus Clay material. The modal pore entrance size is in the order of 18 nm for both specimens. The total intruded volume can be different due to the presence of the non-intruded minerals, while the characteristic pore size is comparable. The pores larger than 100 nm can be assumed as the inter-cluster pores that refer to the inter-aggregate or the pores associate with the fractures. The fluid flow is expected to predominantly take place within these group of pores and larger fractures.

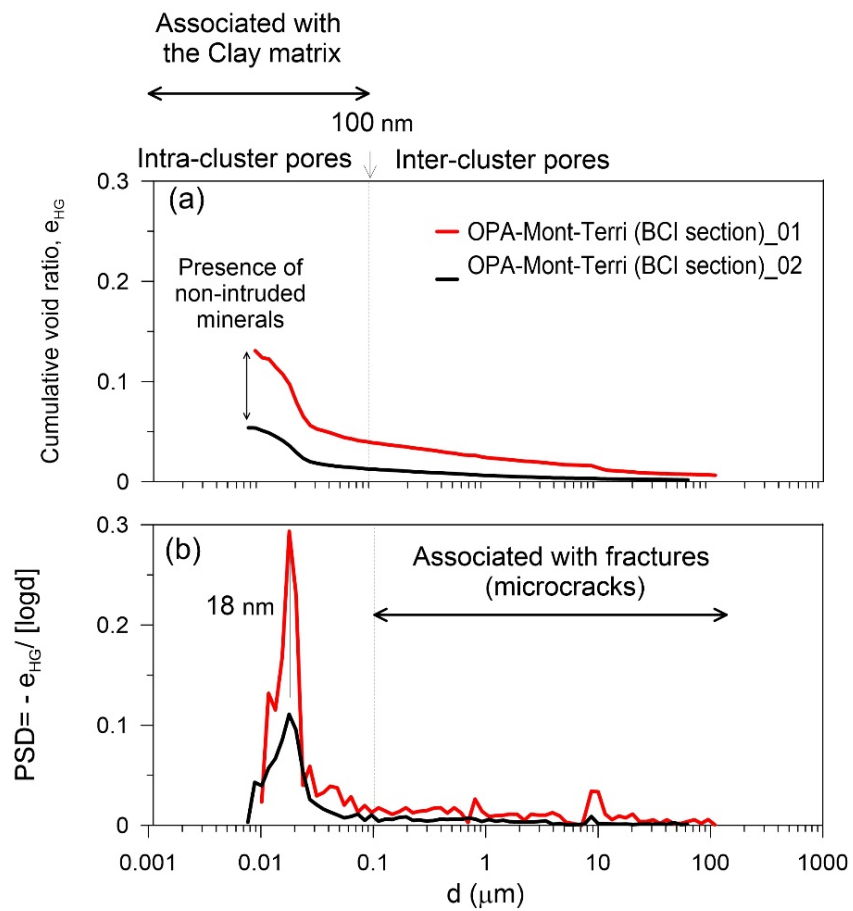


Fig. 13: (a) Cumulative void ratios (e_{GH}) and (b) the pore (entrance) size distribution (PSD) functions for natural Opalinus Clay specimens in the present study

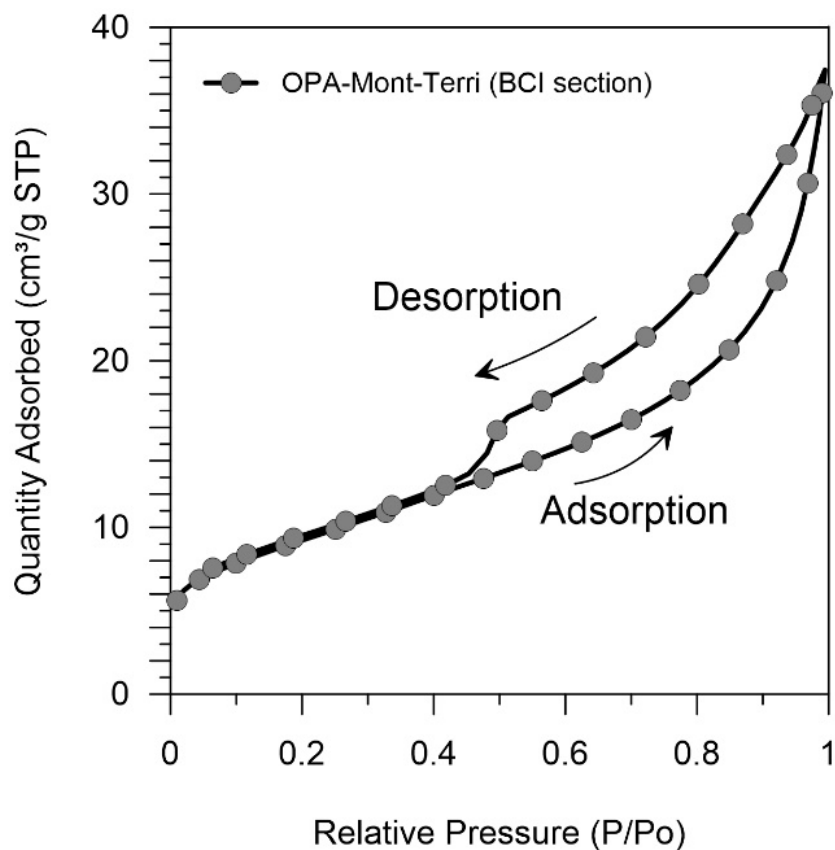


Fig. 14: Adsorption-desorption isotherms of N₂ at liquid N₂ (-197.3 °C) temperature (STP: standard temperature)

The adsorption-desorption isotherms of nitrogen gas of the material is presented in Fig. 14. The material displays Type IV isotherms (Thommes et al. 2015) typical for monolayer – multilayer adsorption in mesoporous and macroporous solids. The hysteresis behavior is under H3 category hysteresis loop that is commonly given by microstructures with non-rigid aggregates of plate-like particles e.g. clays, or consisting of macropores, which are not completely filled with pore condensate (Thommes 2015). The hysteresis between adsorption and desorption branches is associated with the presence of mesopores (2 – 50 nm), while the absence of a plateau at high p/p_0 indicates macropores (> 200 nm). A characteristic 'forced closure' in the desorption branch can be observed (at $p/p_0 = 0.50 - 0.45$) indicating a significant fraction of smaller pores (< 4 nm). The values of the specific surface of Opalinus Clay specimens oscillate around 31 – 33 m²/g for BET estimates, respectively.

3.4 Pore-scale visualization

High resolution scanning and backscattered electron microscopy

Electron microscopic observations were carried out on Opalinus Clay specimens using a Carl Zeiss' Merlin HR-SEM system (ZEISS AG, Jena, Germany) that was equipped with an electron backscatter diffraction (EBSD) analyzer and also provided energy-dispersive X-Ray spectroscopy (EDS) for chemical phase analysis. Electron microscopy imaging (in both Scanning and Backscattered modes) and EDS analyses were carried out at 15 kV at a working distance of 10 mm. Observations were carried out on both broken and broad ion beam (BIB) milled surfaces of the material. Smooth, 2D Surfaces of Opalinus Clay were prepared using a JEOL SM argon-ion cross section polishing system (JEOL Ltd., Tokyo, Japan) by an accelerating voltage of 6 kV, a sample current of 2.8 mA, and a milling time of 8 – 10 hr. The natural Opalinus Clay specimens were cross-sectioned perpendicular to the fissility plane. Both series of specimens were mounted to SEM stubs using carbon tapes and were coated with a 10 nm carbon layer to provide a conductive surface.

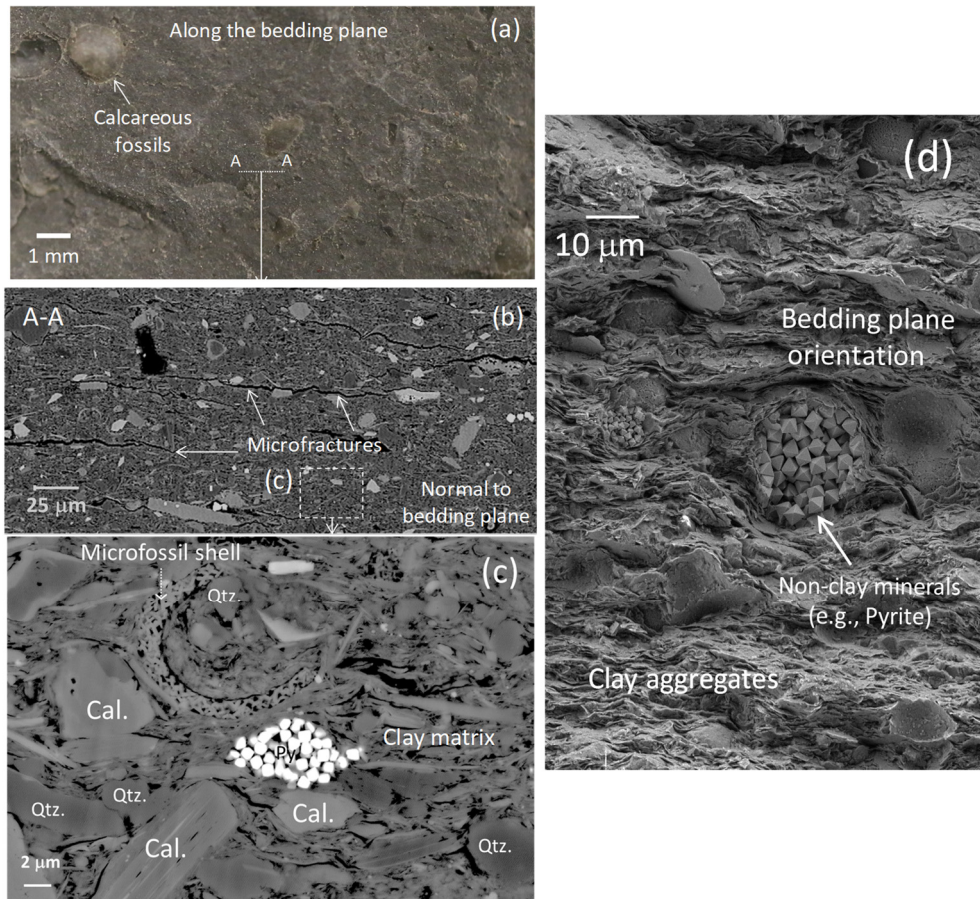


Fig. 15: Typical microfabric of the Opalinus Clay material at Mont-Terri site (BCI and FEA sections)

(a) optical image of a broken surface along the bedding; (b) EBSD photomicrograph of an ion-milled surface indicating the orientation of the fractures with respect to the grains; (d) non-clay mineral grains and microfossils within the clay matrix, and (d) SEM photomicrograph of a broken surface of the material in part (a) exhibiting the highly compacted clay matrix

Fig. 15 provides detailed information on the petrofabrics of Opalinus Clay and demonstrates their variability and heterogeneity. The material exhibits a pronounced microfabric consisting of clay aggregates and tabular-shaped non-clay particles, which are preferentially-oriented parallel to the fissility plane. Inter-aggregate micro-cracks are abundant and show similar preferential orientation. The order of typical microfracture apertures in the electron microscopy images is compatible with information from the MIP analysis presented in Fig. 13. Such microfractures caused by stress unloading during drilling and recovery are likely the potential pathways for the fluid flow and particle transport in Opalinus Clay. A detailed study on the microfabric and diagenesis of Opalinus Clay at Mont Terri site (FE-A section) can be found in Seiphoori (2019) as well as in Seiphoori et al. (2017).

3.5 Interaction with in-situ pore water

The physico-chemical reaction of the OPA material with pore water during hydration is a key element in self-sealing of fractures. To visualize this possible reaction and how fast it can occur over time, a simple experiment was designed where a piece of intact OPA (BCI-21B) was subject to the synthetic water prepared according to (Mäder 2011):

Tab. 4: Synthetic pore water composition for Opalinus Clay after (Mäder 2011)

#	Compound	g/500mL, deionized water
1	NaCl	3.3682
2	KCl	0.0951
3	NaHCO ₃	0.0228
4	CaCl ₂ ·2H ₂ O	0.8755
5	MgCl ₂ ·6H ₂ O	0.9317
6	Na ₂ SO ₄	1.7044

The camera view is along the specimen bedding (fissility) plane direction as shown in Fig. 16. The material exhibits intense slaking behavior short time after immersed in the synthetic water, suggesting slight cementation in the natural state. A fast swelling of the surface is observed (Fig. 16-b) immediately after the material surface hydrates even using the synthetic water with considerable salinity of 13.98 g/L. This behavior indicates that the repulsive forces building up during the hydration of the aggregates can overcome the inter-aggregate cementation bonding and result in disintegration of the entire aggregates. We expect this fast reaction with water play an important role in the fracture evolution during triaxial experiments. On the other hand, the swelling and degree of cementation resulted from the burial diagenesis are the two major factors competing with each other during the interaction with pore water under actual repository-like conditions and within the excavation damaged zones. We also investigated the interaction of Opalinus Clay from the Schlattingen site with the synthetic water and the results are presented in the Appendix (Fig. A-1, and A-2). A less significant disintegration of the material at the Schlattingen site is observed which is associate with the strong diagenetic cementation bonds in this formation. One can expect self-sealing potential in the Schlattingen formation where the swelling is hindered due to cementation effects.

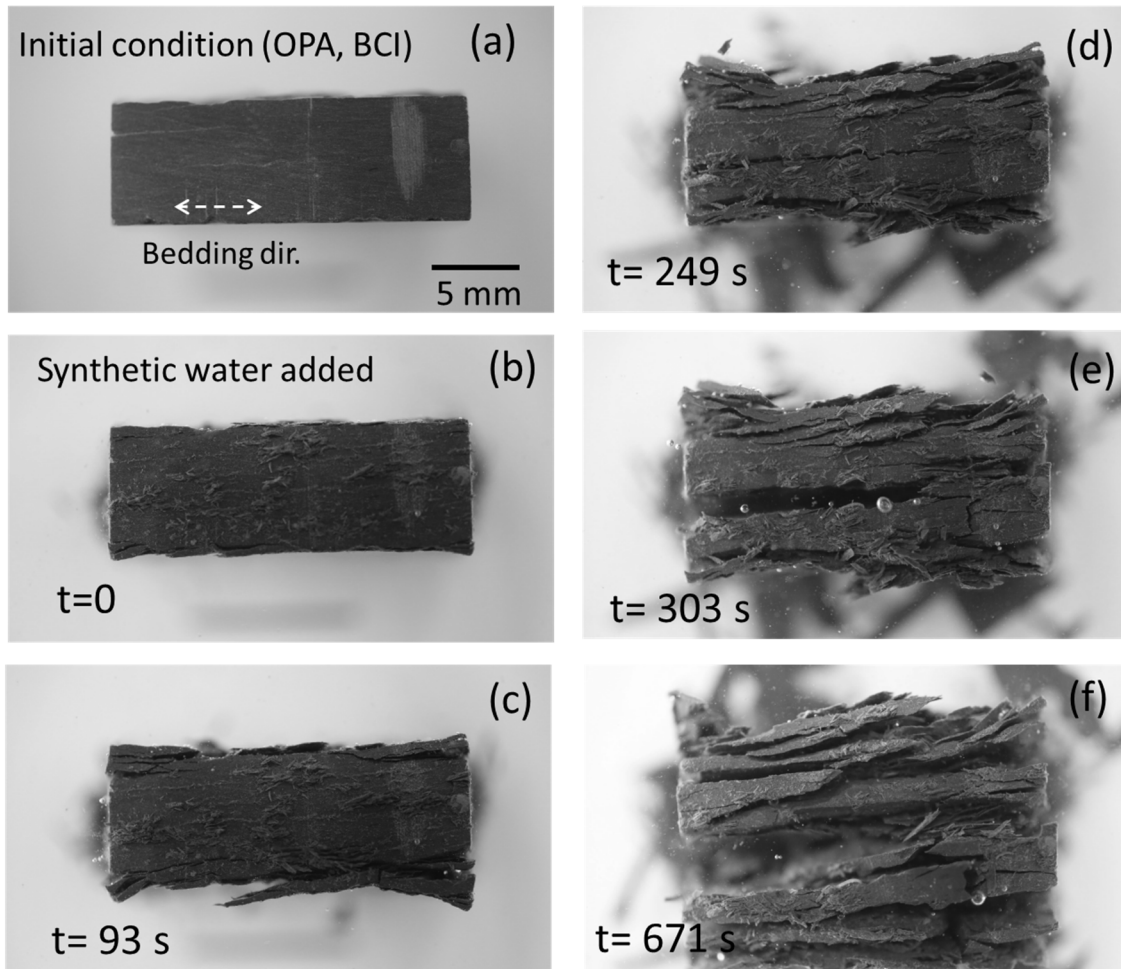


Fig. 16: Time-lapse visual observation of the reaction of Opalinus Clay (BCI-21B) material with synthetic pore water, and fast disintegration of the material due to hydration and swelling

4 Triaxial testing

4.1 Sample preparation

Cylindrical samples were prepared for triaxial experiments. The natural material was first Extruded from The PVC tubes using a horizontal band-saw, and the main material block was cut into smaller pieces using an abrasive band-saw. A precise diamond abrasive wire-saw was then employed to cut hexagonal prisms out from the main block.

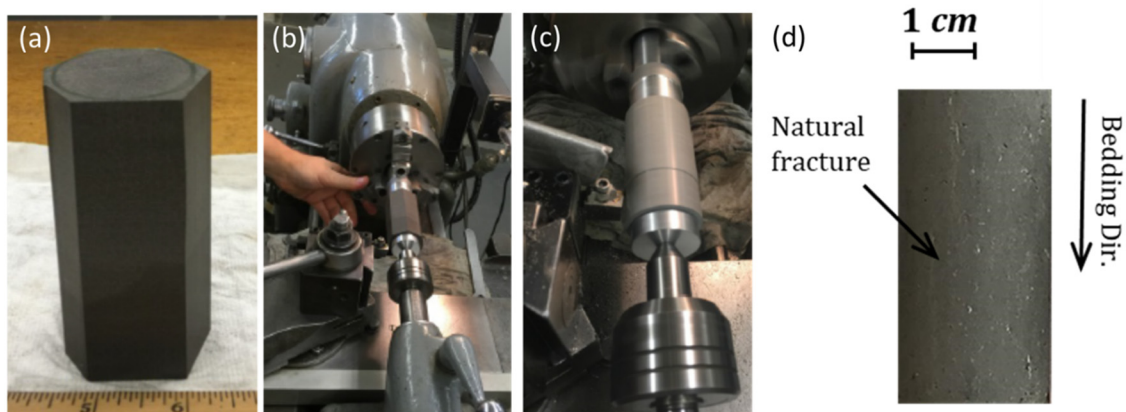


Fig. 17: Hexagonal prism prepared using the wire-saw is cut into cylindrical samples by employing a mechanical lathe as demonstrated in (b) and (c)
A typical p-sample with bedding along the axial direction is shown in (d).

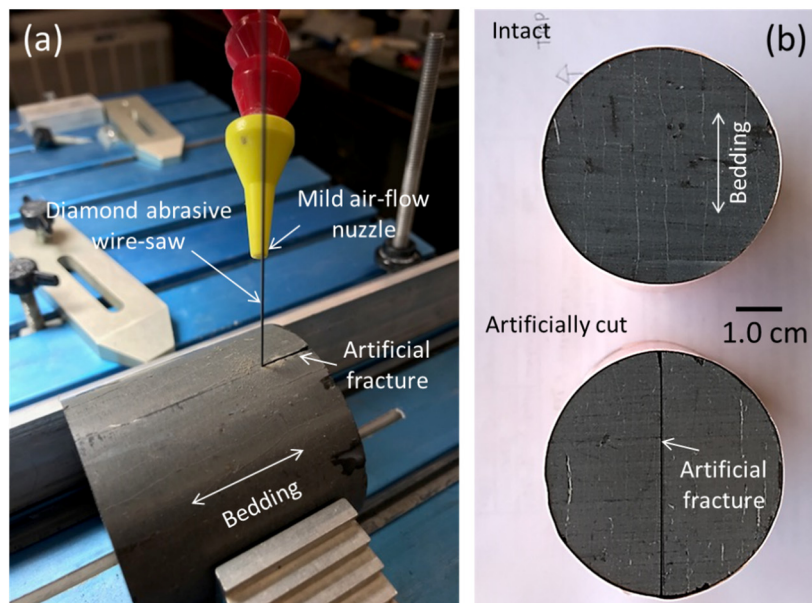


Fig. 18: (a) Creation of the artificial fracture plane using an abrasive wire saw, (b) intact and artificially cut samples

The hexagonal prism then was cut and trimmed into cylindrical samples by employing a lathe machine and a disk grinder as demonstrated in Fig. 17. A typical cylindrical sample prepared by adopting the above-mentioned procedure is depicted in this figure. We found this technique effective, with minimum disturbance to the intact materials. The samples then were sealed and stored for experimental purposes. Triaxial experiments were conducted on both intact and artificially fractured (cut in halves) as shown in Fig. 18. The fracture was created using a diamond (abrasive) wire-saw as demonstrated in this figure.

4.2 Internal fracture network

X-Ray micro computed tomography (micro-CT, Nikon) was used as a non-invasive non-destructive method to characterize the internal pore network of natural Opalinus Clay. The technique provided valuable information on structural features of the material due to the presence of natural fractures. The system provides 3D visualization via reconstruction of image stacks at a voxel (volume element) resolution of up to 5 μm which corresponds to the ability to describe the structural features of the shallow Opalinus Clay material. Considering the size of our triaxial samples, the maximum resolution attainable is 32 μm.

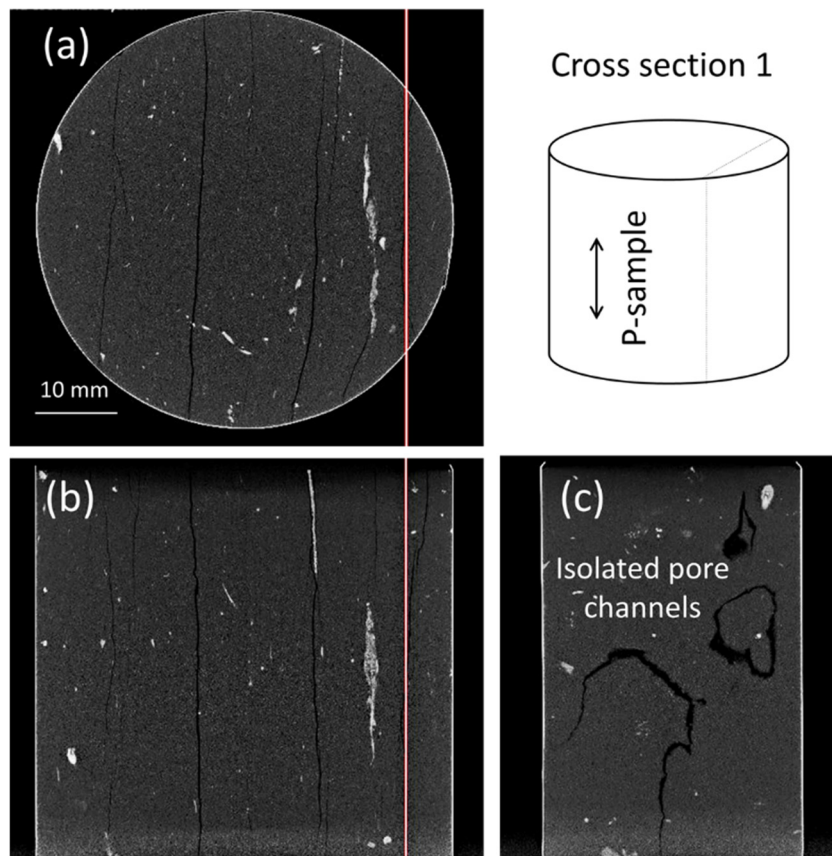


Fig. 19: X-Ray micro-CT analysis of a p-sample of Mont-Terri Opalinus Clay (BCI section), where the isolated pore channels along the bedding plane can be observed

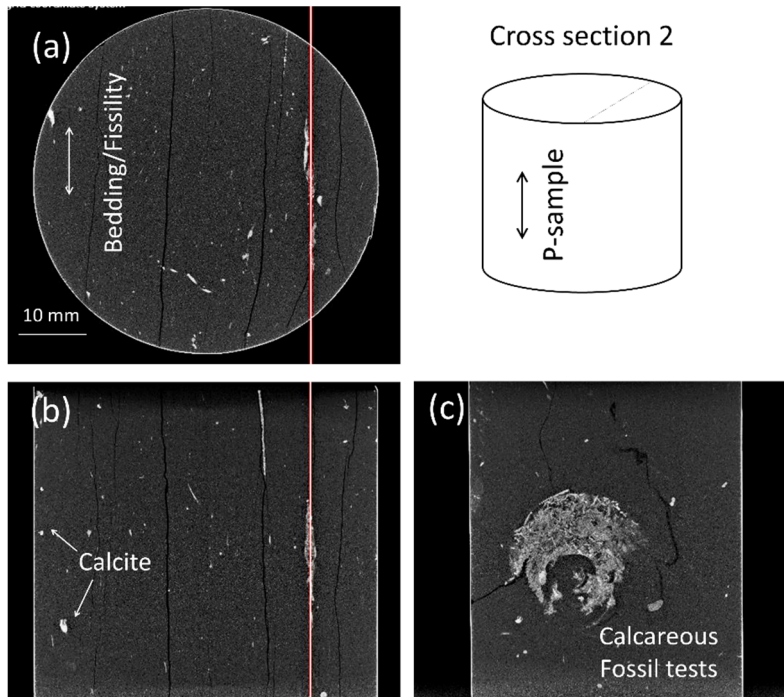


Fig. 20: The bright grains are either the carbonate calcium particles or the calcareous fossil tests across the bedding plane of the material

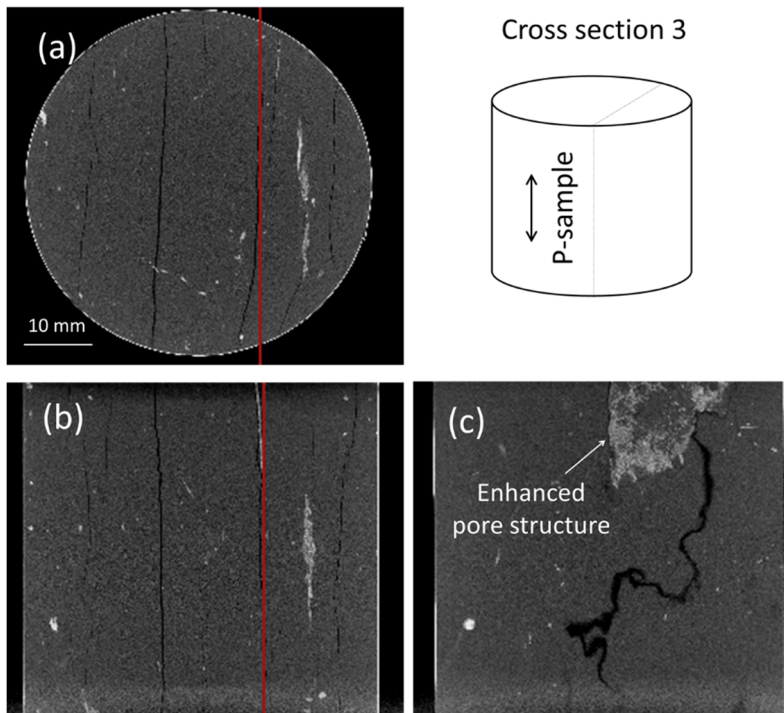


Fig. 21: Enhances pore channel along the bedding and in the proximity of the non-clay particles and particularly the fossils

The presence of micro-channels along the microfossils were observed previously in the microscopic images.

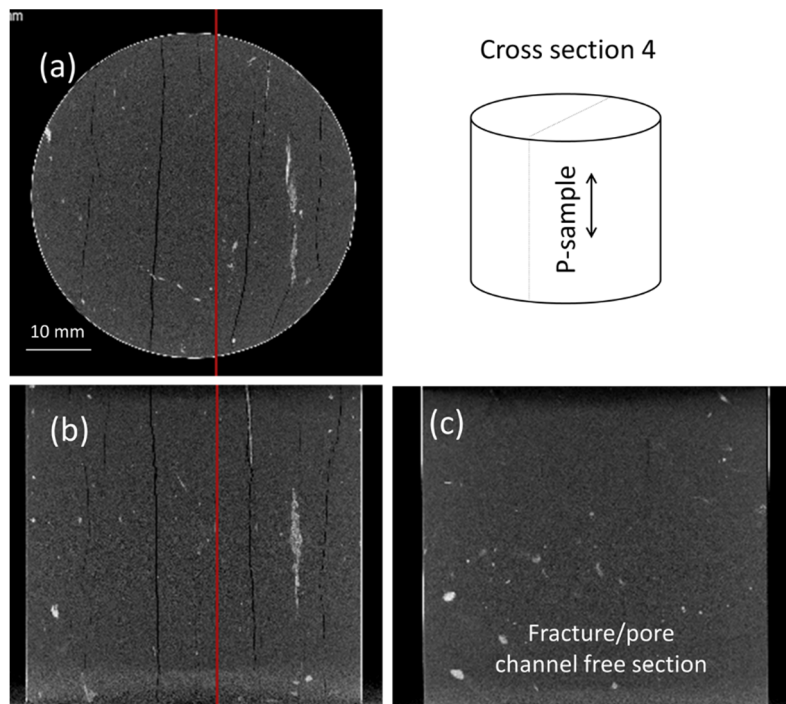


Fig. 22: A cross section which is free of any pore channels or fractures along the bedding plane

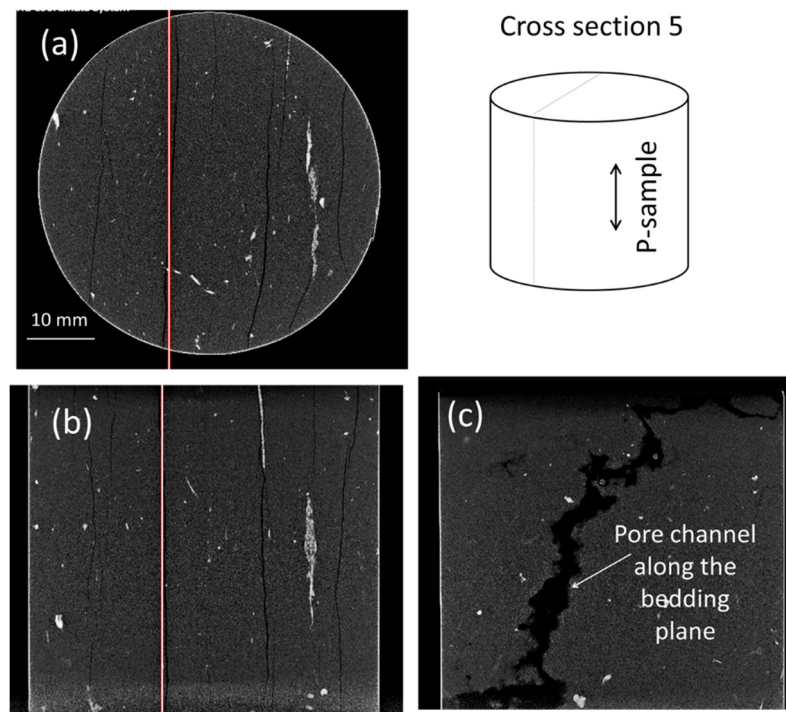


Fig. 23: Presence of irregular pore-channels along the bedding plane which are likely the pathways for flow and particle transport along the bedding of Opalinus Clay material

A rigorous MATLAB coding was developed in order to reconstruct the internal pore structure patterns of the material at different stages of the hydro-mechanical self-sealing experiments. The X-Ray micro-CT results of an intact cylindrical sample of Opalinus Clay from Mont-Terri (BCI section) where the bedding (fissility) plane is aligned with the vertical axis (p-sample) are shown in the following figures for several cross sections along the bedding planes. The material is characterized by significant material and structural heterogeneity. The bright grains are calcite particles which are likely the main source of cementation in the material, along with the calcareous fossils' tests as large as about 20 mm in size. The pore-channels within the bedding have arbitrary structures and likely the potential pathways for the flow and transport across the materials (Fig. 23c). The hydro-mechanical evolution of these channels due to the inter-plane hydration and the normal effective stress acting on these planes control the hydraulic conductivity of the natural material.

4.3 Calculation of the in-situ stress conditions

According to the Swiss disposal concept (Johnson *et al.* 2004), the potential repositories for HLW will be located in the Opalinus Clay formations at depths of about 500m to 900m below the ground surface. The corresponding lithostatic stress and effective stress at this depth of the geological media can be calculated using the following equations:

$$\sigma_p = [(1 - n)G_s + n]\gamma_w h \quad \text{Equation 5}$$

$$\sigma'_p = \sigma_p - u = (\gamma_{sat} - \gamma_w)h = (1 - n)(G_s - 1)\gamma_w h \quad \text{Equation 6}$$

where n is the shale total porosity, G_s the specific gravity (ρ_s/ρ_w) and ρ_s and ρ_w are the solid and water densities, respectively, γ_w is the water unit weight, and h is the in-situ depth of the formation. Note that an average density is assumed here for the sake of estimation. The actual density depends on the various existing lithologies to the surface. Using these equations, a total stress in range of 12 – 22 MPa, and an effective stress in range of 7 – 14 MPa can be expected at the repository depth. The stresses applied during triaxial testing are compatible with the in-situ stresses estimated here with a maximum confining stress of 16 MPa and a maximum pore water pressure of up to 4 MPa.

4.4 Permeability

Permeability is a property of a porous medium that is an indication of the ability for fluids (gas or liquid) to flow through the medium with a unit (m^2), or darcy ($1 \text{ darcy} = 9.87 \times 10^{-13} m^2$). Permeability is part of the proportionality constant in Darcy's law which relates the steady state fluid flow rate to a pressure gradient applied to the porous media:

$$\frac{Q}{A} = \frac{k}{\mu} \frac{\Delta P}{L} \quad \text{Equation 7}$$

where:

Q is the flow rate of the fluid (m^3/s).

A is the cross section of the sample (m^2).

k is the permeability of a medium (m^2).

μ is the dynamic viscosity of the fluid ($Pa \cdot s$); for water $8.90 \times 10^{-4} Pa \cdot s$.

ΔP is the applied pressure difference (Pa).

L is the length over which the pressure gradient acts (m).

4.4.1 Relationship between hydraulic conductivity and permeability

The proportionality constant for the flow of fluid (specifically water) through a porous medium is called the hydraulic conductivity; permeability is one part of this and a property of the porous medium only, not the fluid. Given the value of hydraulic conductivity for a subsurface system, the permeability can be calculated as:

$$k = K \frac{\mu}{\rho g} \quad \text{Equation 8}$$

k is the permeability, m^2 .

K is the hydraulic conductivity, m/s .

ρ is the density of the fluid, kg/m^3 .

g is the acceleration due to gravity, m/s^2 .

4.4.2 Fracture permeability

Transmissivity

Transmissivity in general is defined as the product of hydraulic conductivity and thickness for an aquifer (Ritzema 2006). Transmissivity can be equivalently introduced for the flow through a well-defined rock fracture. The simplest model of flow of flow through a rock fracture is the parallel plate model with an exact calculation of the hydraulic conductivity known as the "cubic law" (Witherspoon et al. 1980). The derivation of the cubic law assumes smooth fracture walls (parallel plates), separated by an aperture h . Zimmerman & Bodvarsson (1996) show that the permeability of such a fracture can be identified as $k = h^2/12$. For a width w , the product of the permeability and area, which is also known as the transmissivity, is equal to:

$$T \equiv kA = wh^3/12 \quad \text{Equation 9}$$

T is the transmissivity for the parallel plate model and has units of $[\text{m}^4]$. In more general form, the transmissivity is in a form of $T = Cwh^3$, where C is a dimensionless parameter fractures (Zimmerman & Bodvarsson 1996). The real fractures, however, have rough walls and variable apertures. Besides, there are regions where the two opposing faces of the natural fracture wall are in contact with each other. To use the cubic law to predict the transmissivity of a real rock fracture, the aperture h can be replaced by the mean apertures, $\langle h \rangle$ (Brown 1987). In order for taking account the effects of roughness and obstructions, Zimmerman and Bodvarsson (1996) suggest replacing $\langle h \rangle$ with the hydraulic aperture h_H . This requires solving the Navier-Stokes equations in fracture geometries by including a varying aperture and obstructed regions. Considering the complexity of formulating the actual transmissivity for an irregular fracture within Opalinus Clay samples in this study, the fracture permeability results are presented in terms of apparent permeability rather transmissivity as defined in next section.

Apparent permeability

In a fractured medium with low matrix permeability such as Opalinus Clay, the total fluid flow takes place predominantly through fractures. The fluid flow can take place through a network of fractures or through a single fracture such as in artificially fractured samples in this study (see Fig. 18). In this study, we define an apparent permeability, k_{app} , for artificially fractured Opalinus Clay sample and define it as:

$$\Delta V = k_{app} A \quad \text{Equation 10}$$

where ΔV is the total transferred fluid (m^3), and A is the total cross section in both intact and artificially fractured samples of Opalinus Clay as shown in Fig. 18.

4.5 Triaxial testing equipment

The self-sealing experiments were carried out using an advanced servo-hydraulic operated triaxial cell system (Autolab, 1500) manufactured by NER, the New England Research, Inc (Fig. 24). The layout of the system is schematically presented in Fig. 24. The cell holds samples up to about 50.8 mm (2.0 in) in diameter to apply in-situ stress conditions, pore pressure, and temperature.

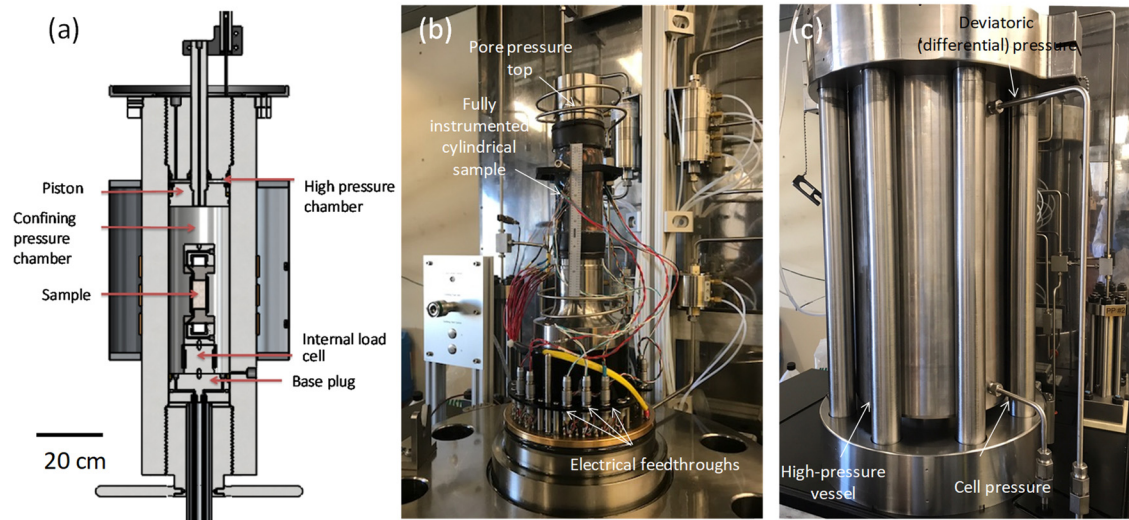


Fig. 24: High-pressure triaxial cell parts and the fully instrumented sample

Multiple locally installed strain gauges, internal LVDT, internal load-cell, and the acoustic channels around a copper-jacketed cylindrical sample coated with a flexible epoxy layer for extra sealing purposes

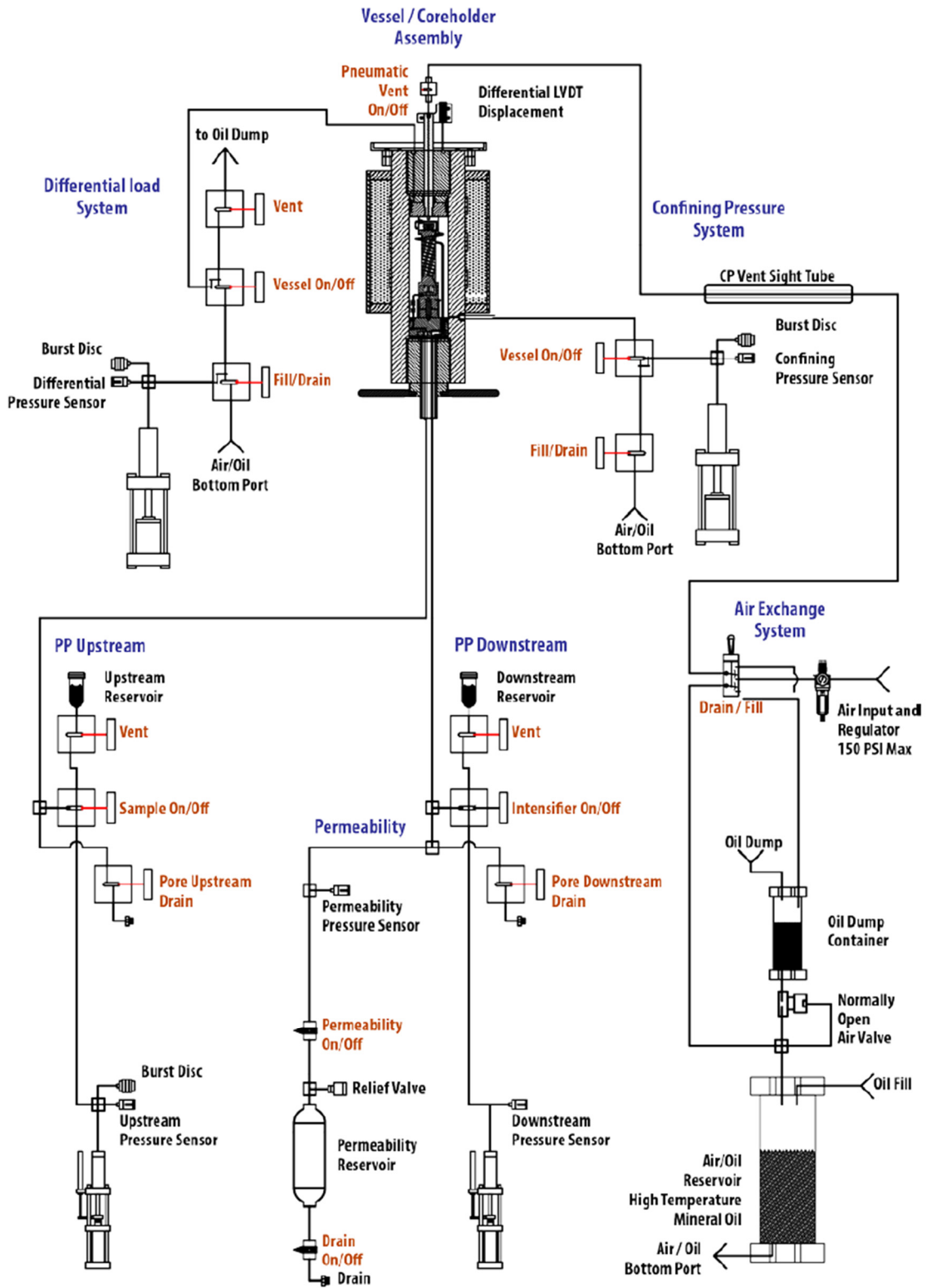


Fig. 25: Schematic layout of the advanced triaxial testing equipment in the study of self-sealing fracture of Opalinus Clay material

The triaxial system consists of a pressure vessel with an internal piston for differential stress and servo-hydraulic intensifiers for differential (deviatoric) stress, confining and pore pressures. An electronics console interfaces with the mechanical system to precisely control the state of stress and to condition and amplify signals from the transducers and devices measuring force, pressure, displacement, strain, temperature, velocity, and resistivity. A data acquisition system generates reference signals to control the equipment, to acquire data, and to process the data collected on each experiment as of Fig. 25. The design comes in two standard configurations, making it convenient for routine measurements at reservoir pressures up to 69 MPa or 138 MPa and temperatures up to 120 °C. In the 69-MPa configuration, the load-cell is calibrated to 790 kN which is sufficient to bring the Opalinus Clay samples to failure at the maximum confining pressure for the system. The servo-hydraulic system provides controlling confining pressures, pore pressure, flow-rate, strain rate and axial deviatoric load. The pore pressure intensifier system allows testing with water of different chemical composition (i.e., synthetic water). The system is equipped with an acoustic module (piezo-electric transducers) that allows measuring the compressional and shear (P and S) wave velocities over any stress path in either an active or a passive configuration.

4.5.1 General sample assembly

This section describes the general procedure for assembling the triaxial samples. Cylindrical samples are first weighted, and the dimensions are recorded. The samples were then copper-jacketed, and the jacketing was secured to the end platens using two viton loops sealed with a layer of a two-piece flexible epoxy. Analytical filter papers (Schleicher & Schuell #595) and two metallic mesh (#80) were used on both ends to prevent migration of particles into the pore fluid paths during the experiments. The sample then was installed in the triaxial vessel and pressurized up to 10 MPa over a short period. This step was conducted to ensure that the copper jacket conforms on the sample prior to installation of the strain gauges and acoustic sensors. The instrumentation was completed after the pressurization stage. A photograph of an assembly is shown in as shown in Fig. 26. This figure shows the base plate and plug with the vessel O-ring seal, the sample assembly ready for insertion into the pressure vessel as shown in Fig. 24. The base plug contains 48 high-pressure electrical feedthroughs, three pore pressure ports, and a thermocouple. Once the sample was inserted into the transducer assembly, it was attached to the load cell with a centering pin. The load cell was connected to the appropriate four-pin connectors mounted on the base plug. The four-pin connectors provide sufficient data output for all of the measurement options supported by the system.

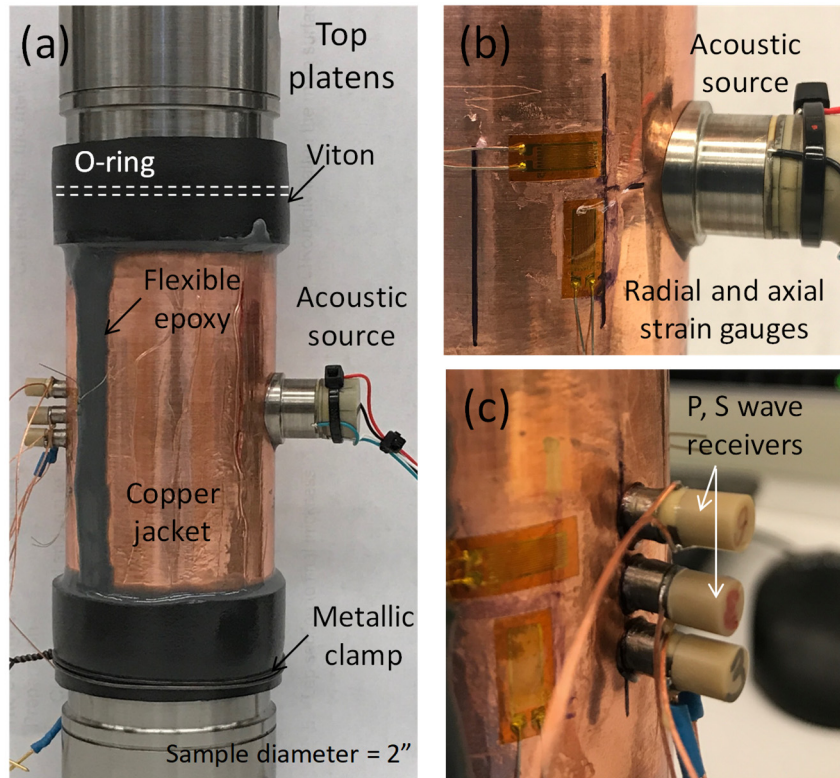


Fig. 26: The sample assembly prior to the triaxial experiment and the installation of the strain gauges and acoustic sensors

The load cell measures the differential force on the sample during the test. The total force on the system is the force exerted by the confining pressure plus the differential load exerted by the piston in contact with the sample. Since the load cell measures the force in excess of the force exerted by the confining pressure, when converting to stress, the confining pressure plus the differential stress on the sample equals the total axial stress. For the sample shown in Fig. 26, strain gages were used to monitor the deformation of the Opalinus Clay sample either at the location of the artificial fracture or on the matrix. Finally, the pore pressure lines were attached, both the upper and lower pore pressure intensifiers in the system, and the appropriate pore pressure connections made on the base plug. Once the sample column was assembled, the pressure vessel was lowered onto the pressure seal using a crane. The top vessel was mounted to a crane system that allows lifting and horizontal movement using a powered control. We chose two sets of aspect ratios for the cylindrical samples: 2×1 and 1×1 (height to diameter ratio). The second series were selected for the permeability data and in the case where only isotropic behavior of the material in triaxial testing was the major consideration. The shorter length was chosen to decrease the equilibrium time in consolidation and fluid flow processes in a typical cylindrical sample (equilibrium time $\propto h^2$, where h is the sample height).

4.5.2 Cylindrical samples for self-sealing experiments

The triaxial experiments were conducted on the intact and artificially fractured samples as shown in Fig. 18. The samples are 1×1 (height to diameter ratio) type. The initial geometrical and physical properties of an intact sample is presented in Tab. 5. Although the initial degree of saturation of the material was calculated as 96 % (see Tab. 1), the material was observed to lose moisture during the sample preparation steps (Section 4.1). In addition, the release of confining pressure and the slight desiccation at the laboratory condition during the sample preparation results in a slight opening of the natural fractures along the fissility plane. As a result, the degree of saturation before jacketing was calculated as 83 %, for a total porosity $n = 0.18 - 0.19$. Another challenge during sample preparation was related to the creation of the artificial fracture along the bedding plane as described in Section 4.1 which resulted in formation of irregular patterns on the fracture's wall surfaces. The intersection of the irregular fissility plane with the straight direction of the wire-saw resulted in spalling of the material from the fracture wall as shown in Fig. 27-a and b. The both halves of the cylindrical sample then were paired, wrapped in a copper jacket for X-Ray Micro-CT tomography. The X-Ray images of the sample is shown in Fig. 27 c to e, where the natural and artificial fractures are observed. It should be noted that the sample cross-section is not a perfect circle. The loss of material during wire-sawing and a slight grinding the surface using sand papers (40 and 120 grit) result in the reduction of the sample diameter normal to the fracture plane. It should be noted that due to the presence of the artificial fracture, the calculation of the total porosity and the initial degree of saturation of the sample is approximate as listed in Tab. 5. The sample was fully instrumented after initial pressurization to 10 MPa to ensure that the copper jacket conforms onto the sample prior to installation of the strain gauges and acoustic sensors.

Tab. 5: Geometrical and physical properties of the tested samples in triaxial system

Sample	Dimensions (mm)	Density, ρ (g/cm ³)	Porosity, n (%)	Initial water content, w (%)	Initial degree of saturation (%)
OPA-BCI-intact	D = 51.5 H = 52.9	2.39	0.187	6.95	83
OPA-BCI-fractured	D ₁ = 50.4 D ₂ = 43.6 H = 52.6	≈ 2.39	> 0.187	6.95	< 83

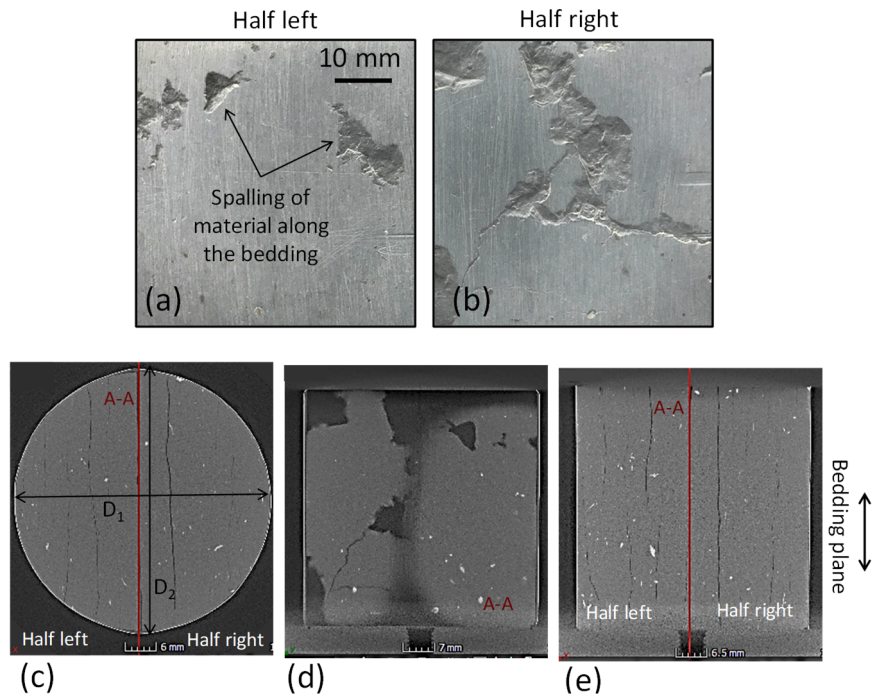


Fig. 27: Spalling of the material from the fracture wall

(a), (b) formation of irregular patterns on the wire-cut surfaces of the artificially fractured Opalinus Clay sample two halves; (c)-(d) X-Ray micro-CT images of the paired halves prior to installation in triaxial cell and jacketing

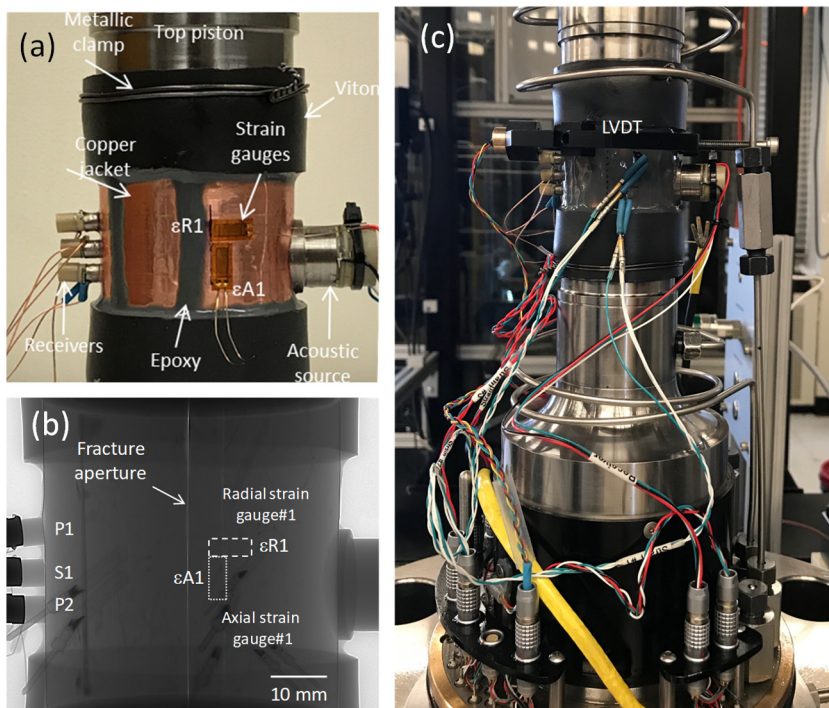


Fig. 28: Cylindrical sample for self-sealing triaxial experiment

(a) sample assembly prior to installation in triaxial cell, (b) X-Ray image of an artificially cut sample; and (c) the configuration of the sample and sensors after installation in triaxial cell

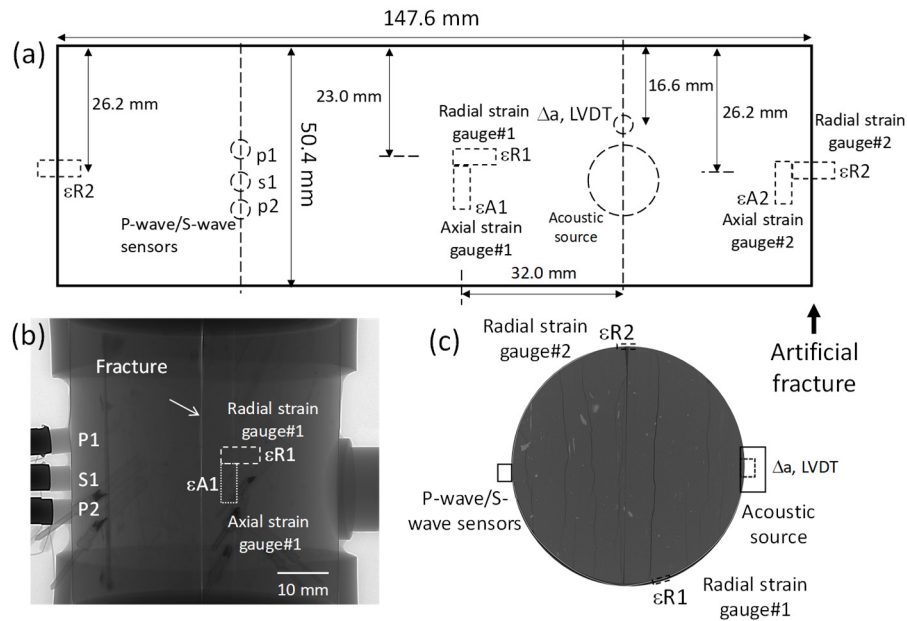


Fig. 29: Instrumentation map on the artificially fractured sample jacketed for triaxial testing
Two pairs of strain gauges across the fracture and on the material matrix are installed as detailed in (b). The relative direction of the bedding planes and the acoustic sensors, LVDT and strain gauges are described in (c).

The configuration of the sample and the installation of the sensors for the acoustic and deformation properties can be observed in Fig. 28. The detailed map of the installed sensors on the jacketed sample, artificially fractured for the self-sealing experiment is shown in Fig. 29. The internal fracture network of the same sample was reconstructed from the tomography data which will be detailed in Section 4.3.2.

5 Results and discussion

5.1 Ar-gas fracture permeability experiments

In this section, we detail the triaxial stress paths applied on an artificially fractured Opalinus Clay sample (OPA-BCI-fractured, Fig. 28) for the Ar-gas permeability experiments as shown in Fig. 30. The gas permeability results on the intact sample is also presented for the sake of comparison. After installing the instrumented sample (OPA-BCI-fractured, Fig. 28) in the triaxial cell, the confining pressure (σ_p , cp in the plots) was first increased to 5.2 MPa. The top and bottom Ar-gas (pore) pressures (u_t and u_b) were then increased to 3.8 MPa and kept constant during the entire experiment. Several cycles of the isotropic loading and unloading were applied by increasing and decreasing the total confining (cell) pressure as depicted in Fig. 30. A 17-hour constant effective pressure condition was applied to investigate the creep effect on the material. The fluctuation in pore Ar-gas pressures (Fig. 30) is associated with the attempts for steady-state permeability measurements. The effective pressure here is defined as the total isotropic pressure minus the average pore gas pressure ($\sigma'_p = \sigma_p - u_{avg}$) as plotted in the figure with respect to the experiment time.

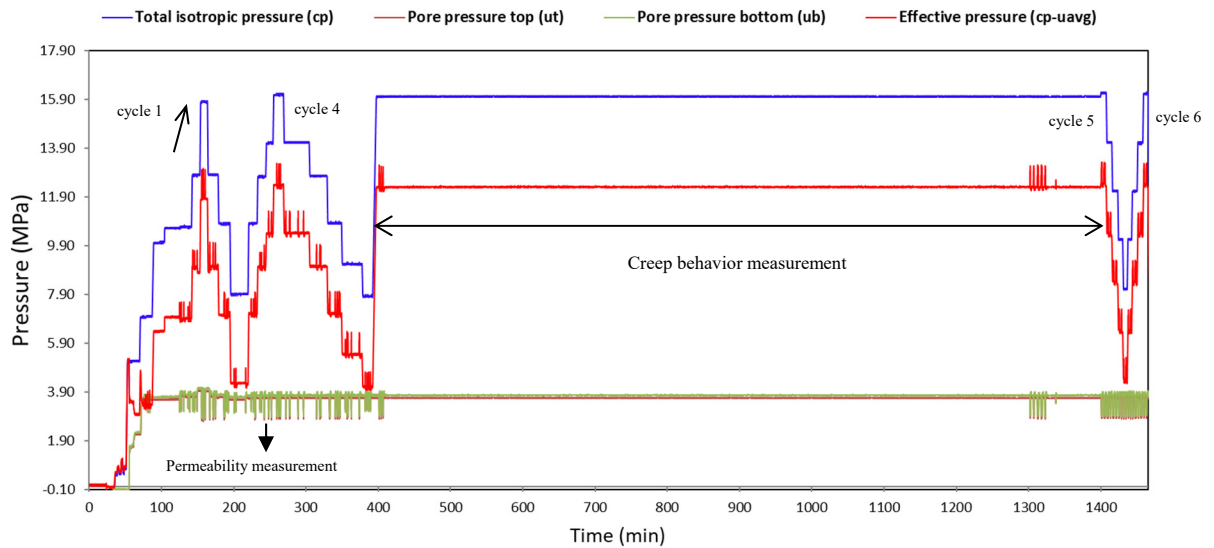


Fig. 30: Variation of the total isotropic pressure, pore gas (Ar) pressures at top and bottom of the sample and the effective pressure with respect to time

The fluctuations in the gas pressures indicate the attempts for the steady-state permeability measurements.

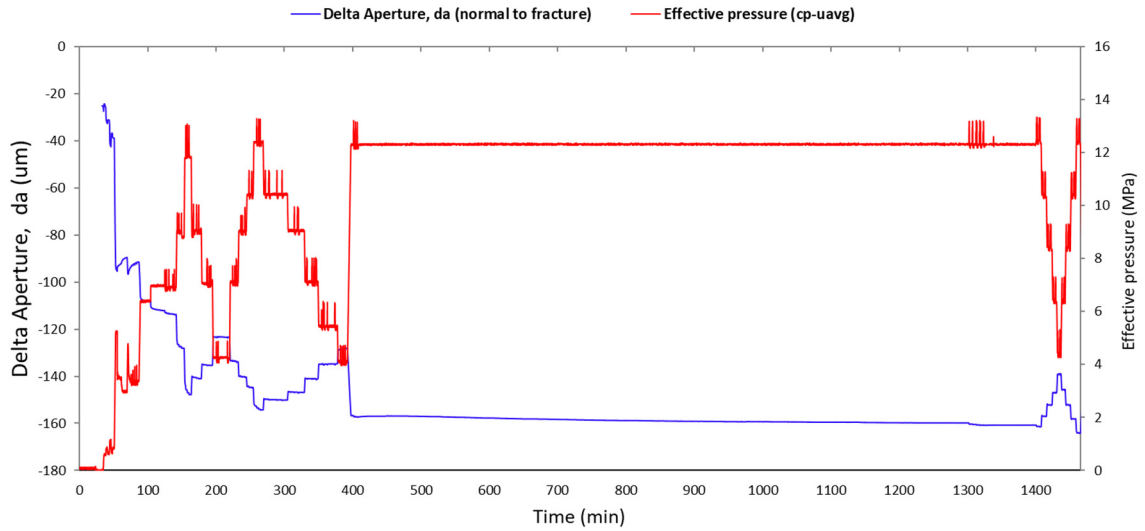


Fig. 31: Variation of the aperture displacement measured using the LVDT positioned in the direction normal to the fracture plane

The variation of the total deformation normal to the fracture is measured using an internal LVDT installed on the sample circumference (see Fig. 29-b). This variation is associated with the change in the major (artificial) aperture and the natural fracture closure. While this deformation is mainly controlled by the artificial fracture (than the natural fractures), we call the LVDT variation as the delta aperture (Δa , da in the plot). The delta aperture and the effective stress ($\sigma'_p = \sigma_p - u_{avg}$) over time is plotted in Fig. 31. The variation of the aperture change (in μm) with respect to the effective pressure is also plotted in Fig. 32. The total deformation includes the elastic and accumulative inelastic (plastic) deformation behavior.

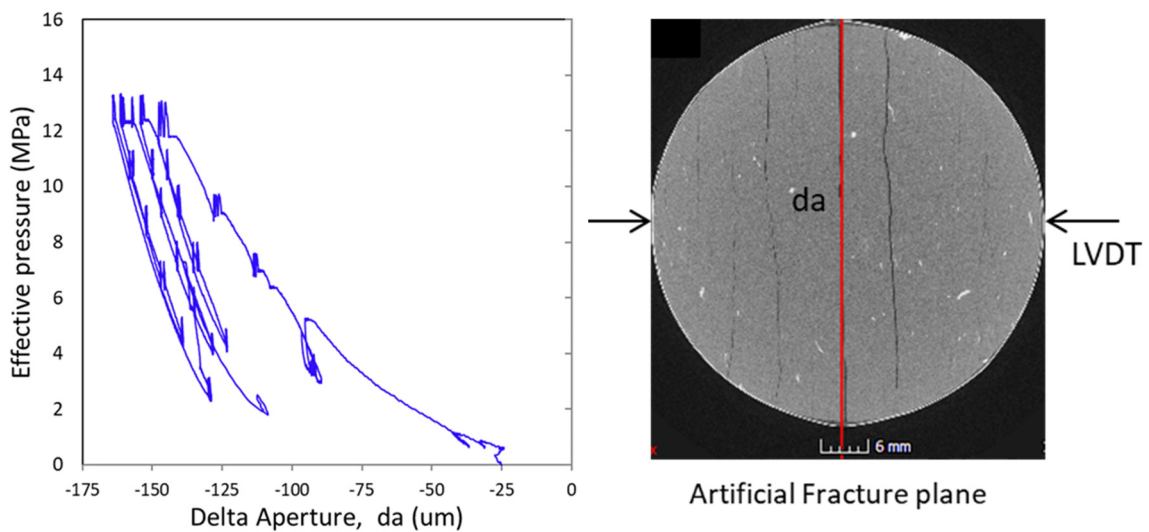


Fig. 32: Aperture change measured by the LVDT installed normal to the fracture plane with respect to the cycles of the applied effective pressure

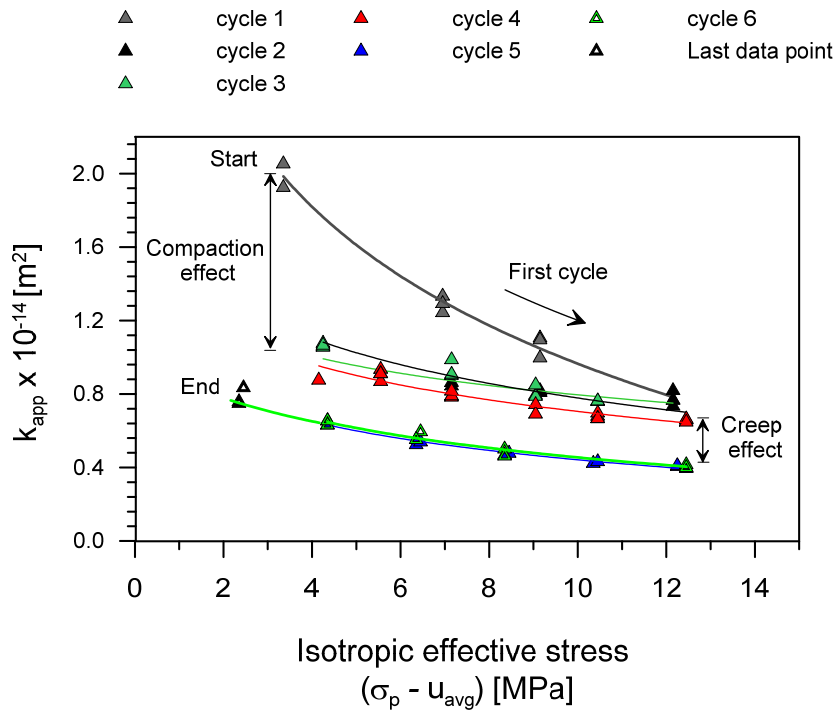


Fig. 33: Ar-gas apparent permeability of the artificially fractured Opalinus Clay sample as a function of the applied isotropic effective pressure for several cycles of loading and unloading. Cycles 5 and 6 were performed after 17 hours creep of the fracture under an effective pressure of 12.4 MPa (See Appendix B for the tabulated data).

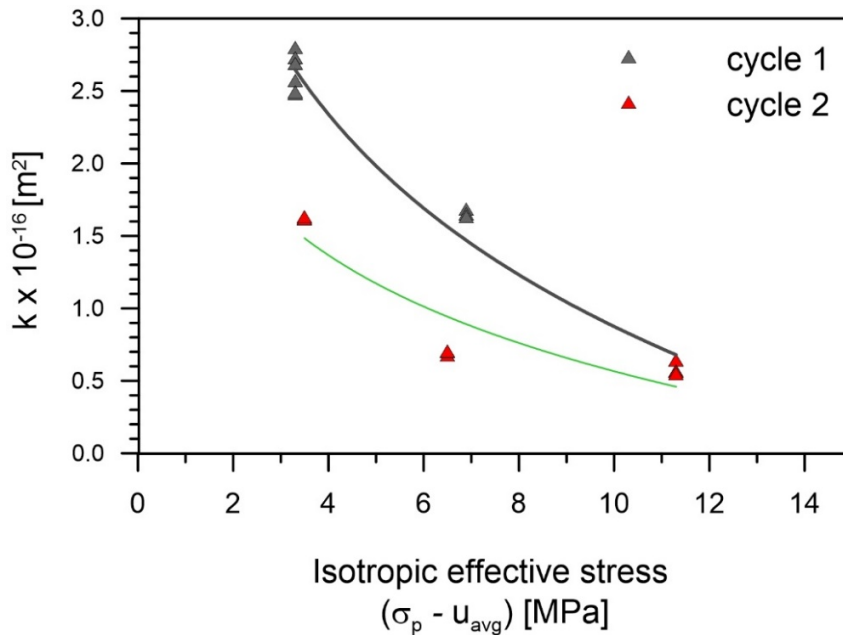


Fig. 34: Ar-gas permeability of the intact Opalinus Clay sample as a function of the applied isotropic effective pressure for one cycle of loading and unloading

The apparent permeability of the artificially fractured sample with respect to the applied isotropic effective pressure for several cycles of loading and unloading is presented in Fig. 33. The apparent permeability decreases with cyclic loading/unloading initially due to plastic deformation of the asperities along the fracture plane (effect of compaction). After second cycle, the hysteresis effect becomes negligible. A hold time of about 17 hours was considered after cycle 4 to evaluate the effect of the creep on the permeability which resulted in a remarkable decrease as observed in Fig. 33. The results of the gas permeability experiments of the intact sample (OPA-BCI-intact) are presented in Fig. 34. The artificial fracture increases the gas conductivity of the medium by two orders of magnitude indicating that the artificial fracture plane performs as an effective pathway for the gas transport through fractured medium. The p-wave velocities were also recorded during these cycles and the results are presented in Fig. 35. The increase in the p-wave velocities from piezoelectric sensors 1 and 2 (see Fig. 28) are in good agreement and indicating the closure of the artificial fracture. The p-wave velocity trend line for the intact sample is also plotted. The average p-wave velocity decreased by about 500 m/s due to the presence of the artificial fracture. The s-wave sensors did not provide values which could be due to the lack of sufficient coupling for shear waves at the fracture location.

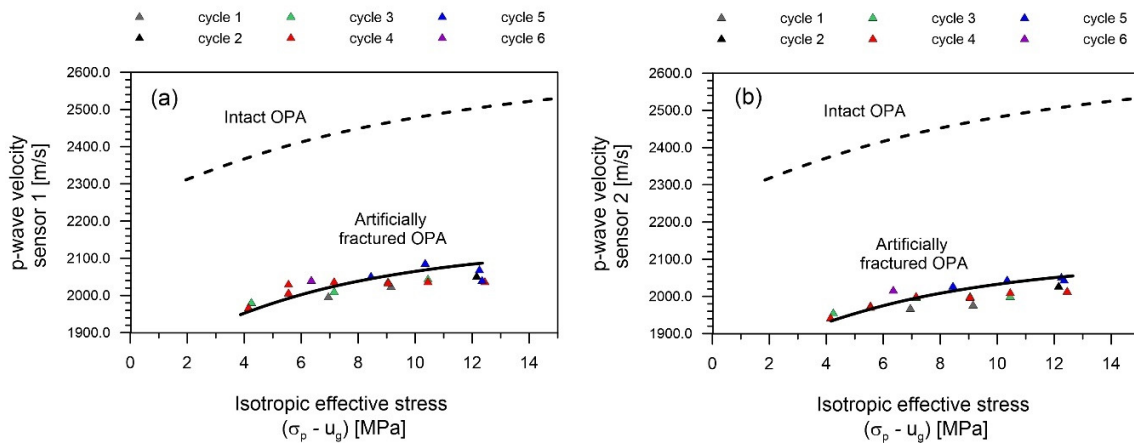


Fig. 35: Variation of the p-wave velocities recorded during the gas permeability using p-wave piezoelectric sensors 1 and 2 as shown in Fig. 28

The artificial fracture significantly decreases the p-wave velocity.

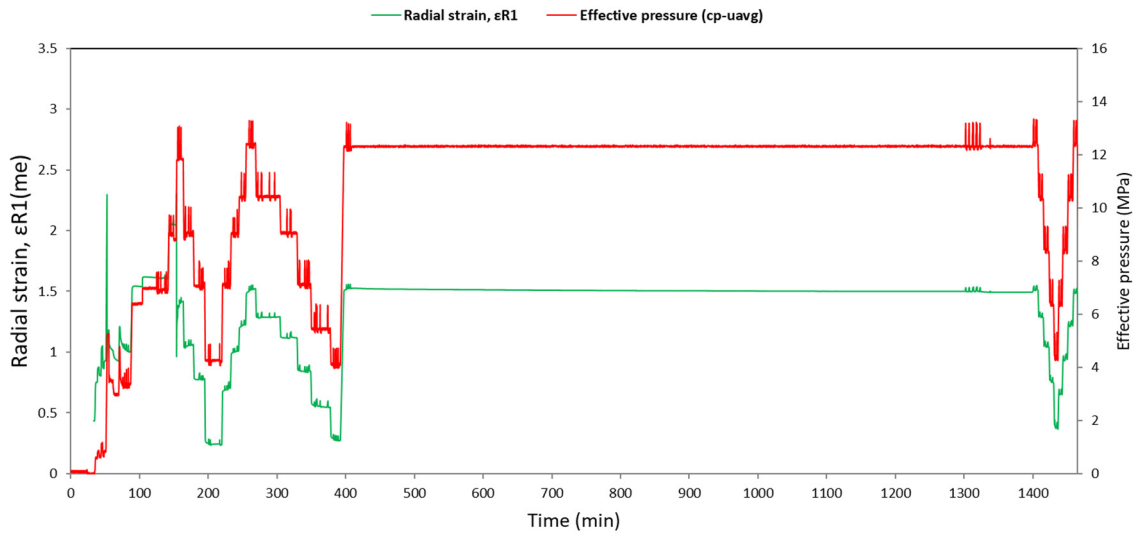


Fig. 36: Variation of the radial strain recorded at gauge#1 (ϵ_{R1} in milli-strain)
See Fig. 29 for the location of the strain gauge

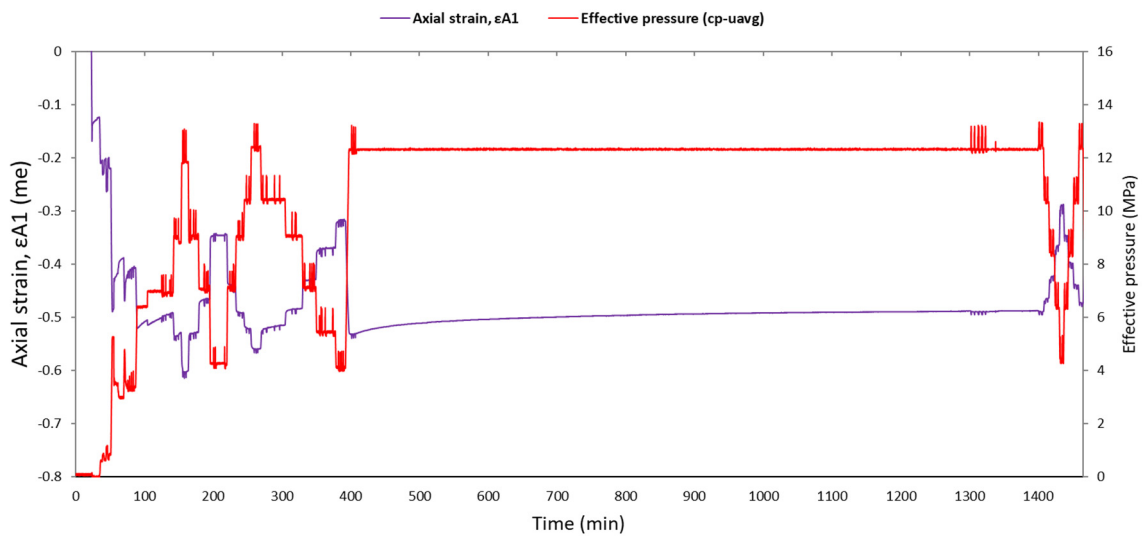


Fig. 37: Variation of the axial strain recorded at gauge#1 (ϵ_{A1} in milli-strain)
See Fig. 29 for the location of the strain gauge

Fig. 36 to Fig. 39, show the measurements of two pairs of strain gauges for the radial and axial directions installed normal to each other as demonstrated in Fig. 29. The effective pressure ($\sigma'_p = \sigma_p - u_{avg}$) over time is also plotted. The radial strain at location 2 (ϵ_{R2}) was installed at the artificial fracture location, and the axial strain at this location (ϵ_{A2}) was installed at the proximity of the fracture. The compression and creep effects are more pronounced for the radial strain gauge installed at this location.

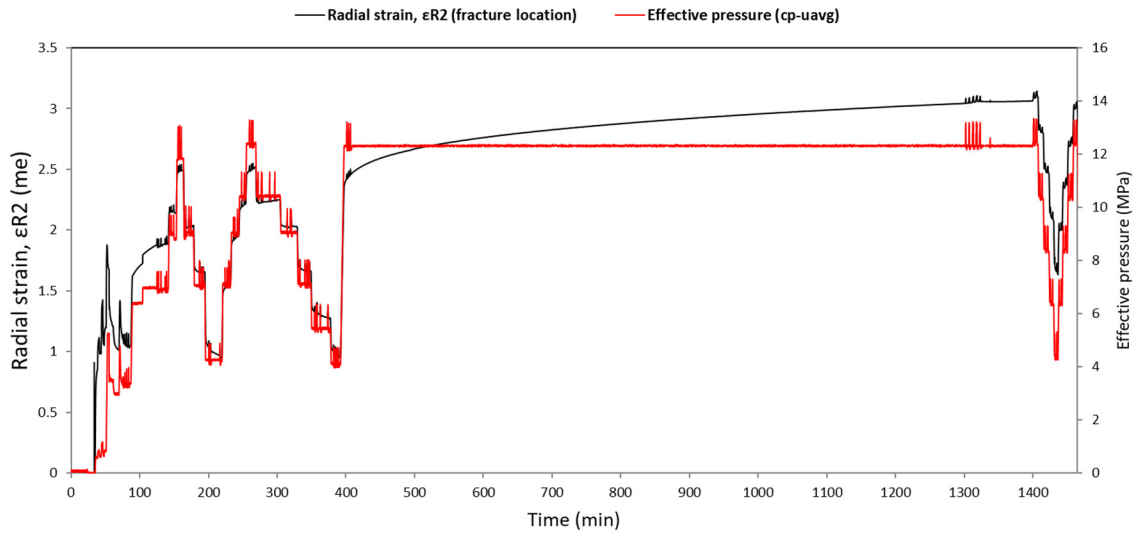


Fig. 38: Variation of the axial strain recorded at gauge#2 (ϵ_{R2} in milli-strain)
See Fig. 29 for the location of the strain gauge

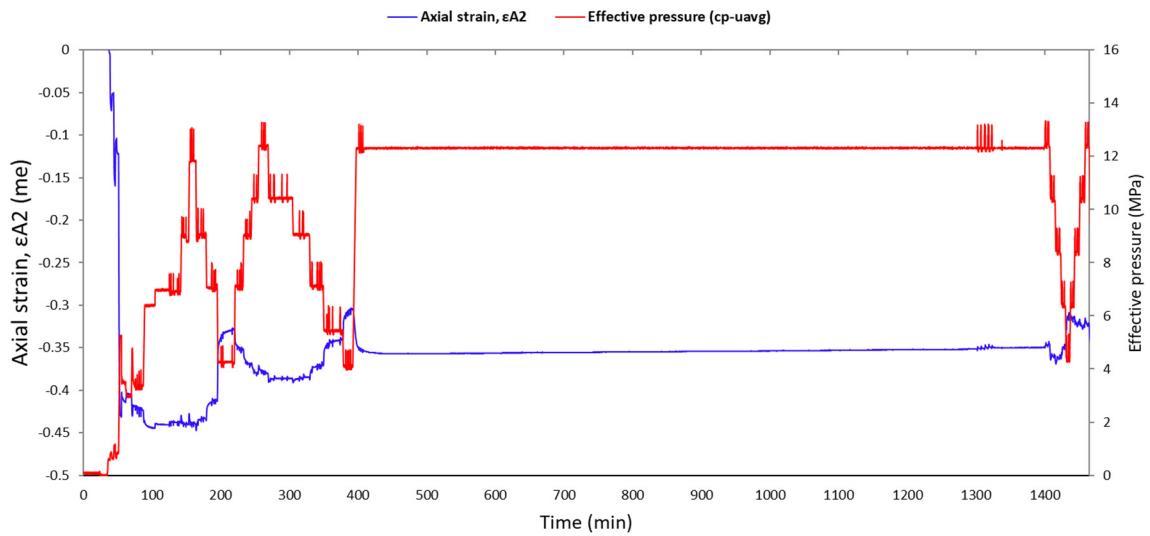


Fig. 39: Variation of the axial strain recorded at gauge#1 (ϵ_{A2} in milli-strain)
See Fig. 29 for the location of the strain gauge

The total volumetric strain of the sample was estimated using the recorded data from the strain gauges installed on the material's matrix as shown in Fig. 29. The total volumetric strain exhibits only a slight accumulation of the plastic strains, which implies the process of closure and opening of the fractures has a negligible effect on the total volume. On the other hand, we showed from the nanoindentation experiments on similar Opalinus Clay material in the first report that the heterogeneity of the material results in a strong spatial variation of the elastic modulus. The reading of the strain gauges thus is expected to be influenced by material heterogeneity of the matrix due to small surface area that the strain gauges cover.

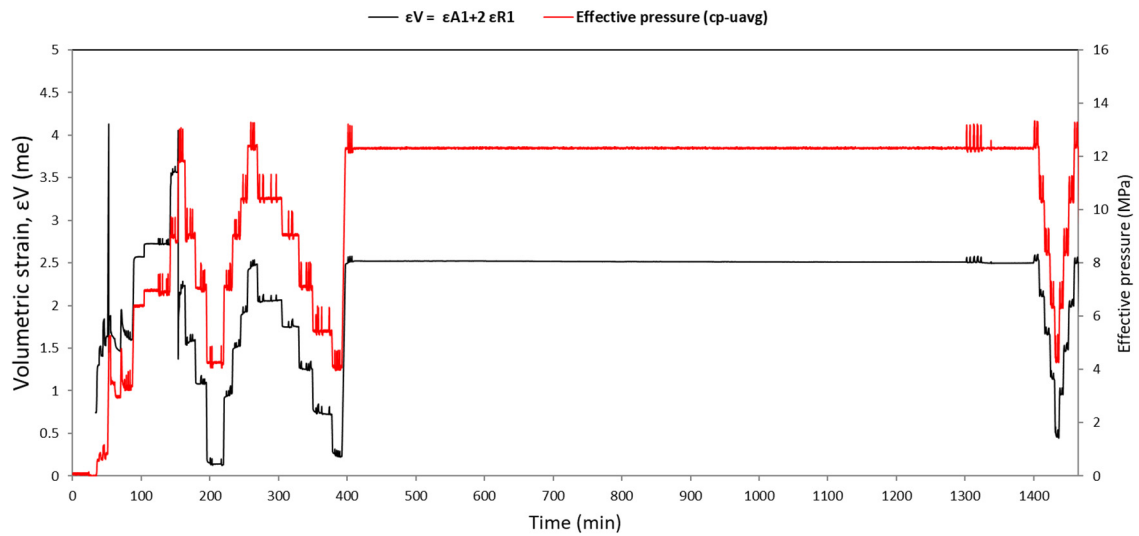


Fig. 40: Variation of the total volumetric strain using data of the recorded axial and radial strain at gauge#1 (in milli-strain) positioned on the material's matrix
See Fig. 29

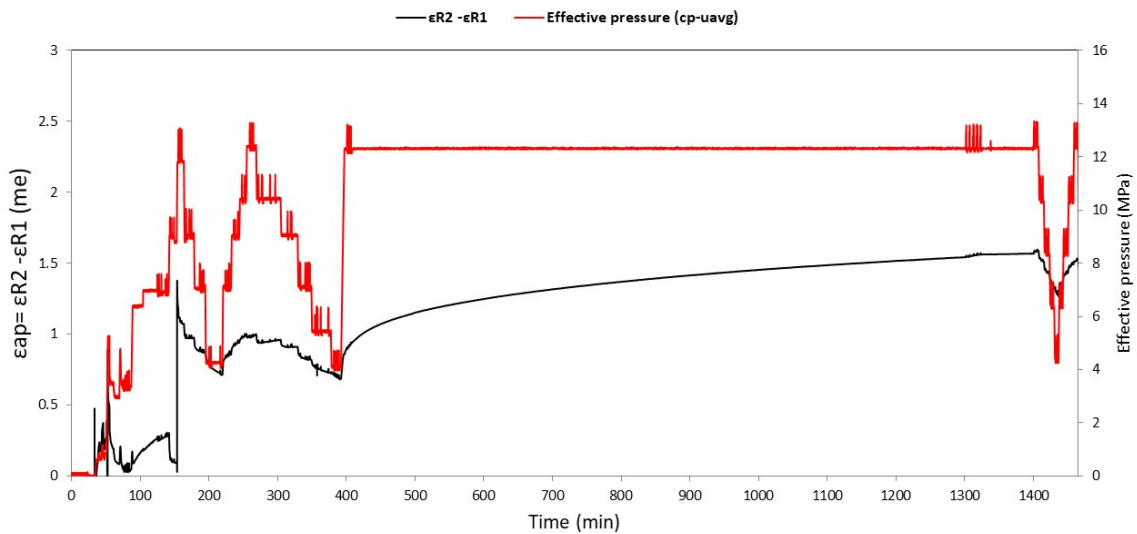


Fig. 41: Variation of the difference in records of the radial strain at gauges #1 and 2 defined as ϵ_{ap} as an indication for the aperture strain of the artificial fracture

The variation of the difference between the radial strains at the location of the fracture and the matrix provides indication for the aperture strain variation during the experiments (Fig. 41). An inelastic behavior of the fracture aperture can be observed during the creep process; an important factor that affect the fluid transmissivity under a given applied effective stress over time, where the gravity-driven creep mechanism can change the asperity and configuration of the contact surfaces and consequently affect the transmissivity.

5.2 Synthetic water fracture permeability experiments

Although the intact sample is permeable to gas, the immediate hydration and swelling after applying synthetic water does not allow the steady state measurement of the permeability. In other words, for understanding the self-sealing mechanism of the fractures, creation of an unsealed fracture is necessary. This section details the self-sealing triaxial experiments on the same sample (OPA-BCI-fractured) described in the previous section. The sample was scanned (X-Ray micro-CT analysis) to investigate the effect of the applied stress path during the Ar-gas experiments. The X-Ray machine allowed scanning of the entire sample assembly without altering any configuration. The sample assembly was then reinstalled in the triaxial cell, and in order to bring the fractures to the state at the end of the gas experiments (previous section), two cycles of loading and unloading were applied, and the Ar-gas apparent permeability was measured at each step. After two cycles, the gas transmissivity was comparable with the final stages of the previous experiment ($k_{app} = 6.3 \times 10^{-15} \text{ m}^2$ at $\sigma_p = 16 \text{ MPa}$, $u_{avg} = 3.8 \text{ MPa}$; $k_{app} = 8.8 \times 10^{-15} \text{ m}^2$ at $\sigma_p = 10 \text{ MPa}$, $u_{avg} = 3.8 \text{ MPa}$). At this stage, the total confining stress was set to 10 MPa, and while the sample was disconnected from the pore pressure controllers, the Ar-gas was evacuated and the pore pressure controller to the bottom of the sample was filled with synthetic water (described in Tab. 4).

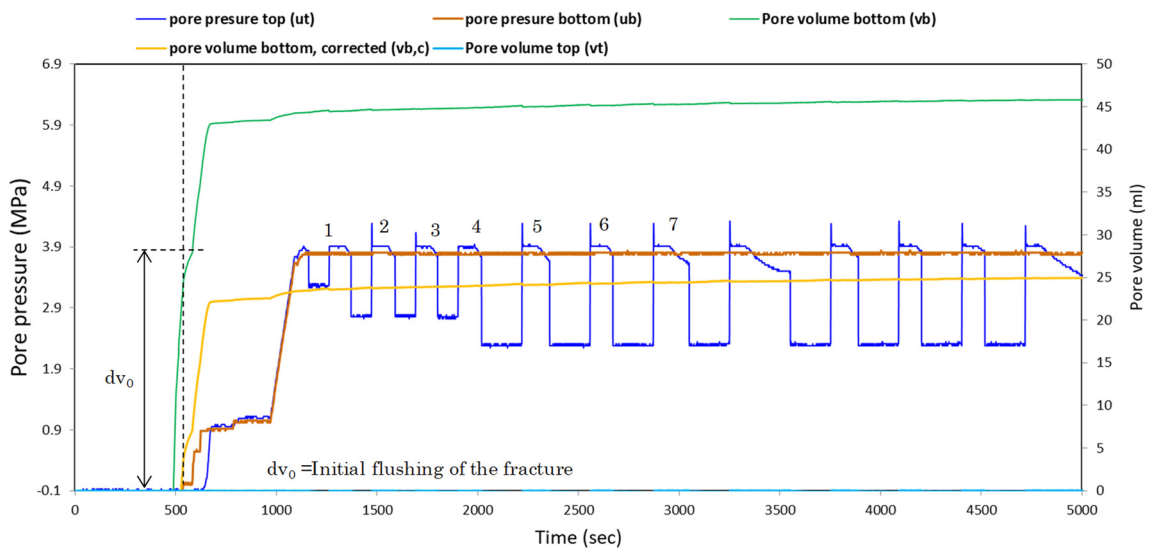


Fig. 42: Variation of the pore water volume and pore pressure applied to the bottom and top of the sample in triaxial experiment

The first jump in pore volume bottom occurs during flushing. Pore pressure top is periodically dropped to induce a pressure gradient for the steady state permeability measurement.

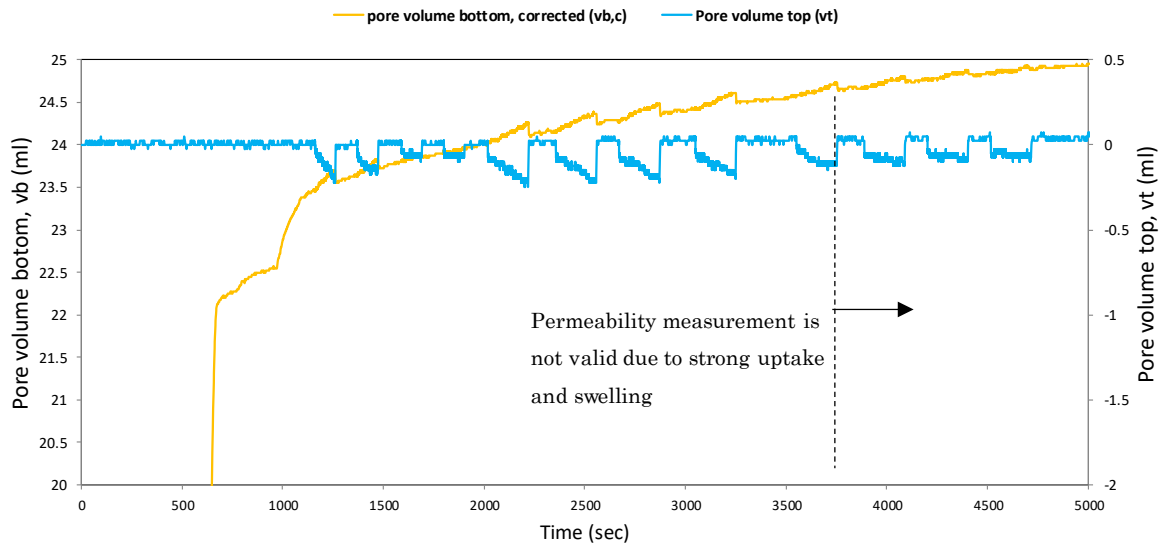


Fig. 43: Variation of the pore volume top and bottom during the steady-state permeability measurement described in Fig. 42

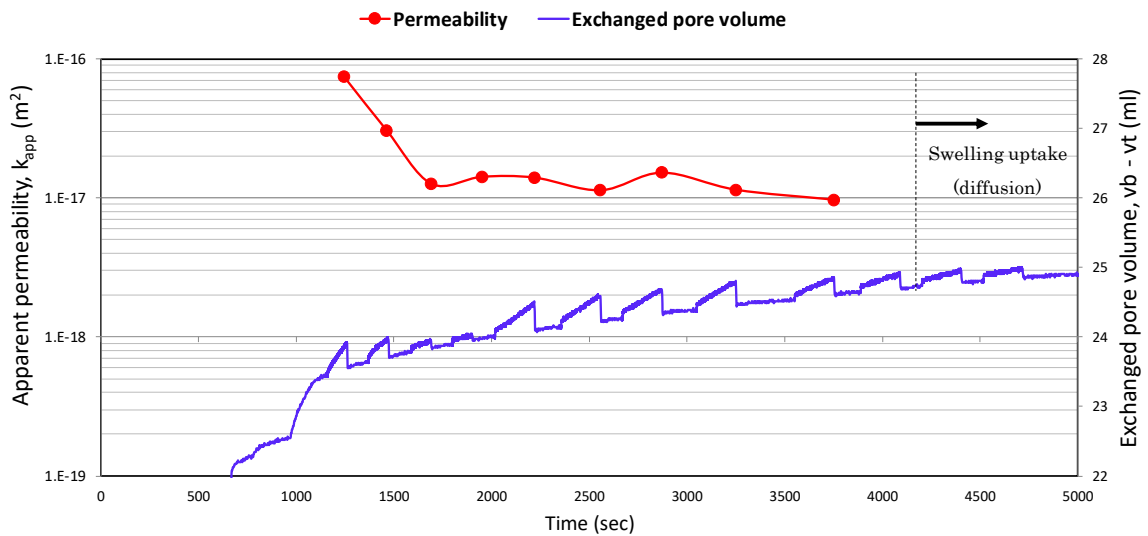


Fig. 44: (a) Change of the apparent permeability over time during the water flow through the fracture

The permeability is measured while the material swells along the fracture plane and decreases due to the self-sealing process of the fracture.

The flow was applied to the bottom of the sample to flush the synthetic water along the artificial fracture plane in a very short time allowing Ar-gas to exit from top valve which was vented to the atmospheric condition. The top pore pressure valve was kept open until a flow of water was observed, then was immediately closed and the pore water was applied to the top of the sample (Fig. 42). This procedure ensures that the fracture is saturated and the air within the fracture would not be entrapped after when the top of the sample is also connected to water flow. The pore water pressures at both ends were then increased to the target values of 3.9 MPa.

In order to measure the water permeability immediately after initial saturation of the fracture, the pore pressure top was periodically dropped to 1.8 MPa to create a pressure gradient over a given measurement time (Fig. 42-b). This measurement was continuously conducted for 9 points until the steady state measurement was not possible because the sample started to uptake water without exchanging between both top and bottom paths. This observation is associated with the swelling along the fracture plane.

Tab. 6: Steady-state apparent permeability measurement during triaxial self-sealing experiment

Attempts	Time	Cell pressure (MPa)	Pore pressure top (MPa)	Pressure difference (MPa)	T (°C)	k _{app} (μD)	k _{app} (m ²)
1	1245	10.2	3.8	1.8	23.8	75.4	7.44 × 10 ⁻¹⁷
2	1463	10.2	3.8	1.8	23.7	31.0	3.06 × 10 ⁻¹⁷
3	1692	10.2	3.8	1.6	23.8	12.8	1.26 × 10 ⁻¹⁷
4	1951	10.2	3.8	1.8	23.7	14.4	1.42 × 10 ⁻¹⁷
5	2220	10.2	3.8	1.8	23.6	14.2	1.40 × 10 ⁻¹⁷
6	2558	10.2	3.8	1.8	23.2	11.5	1.13 × 10 ⁻¹⁷
7	2872	10.2	3.8	1.8	23.2	15.4	1.52 × 10 ⁻¹⁷
8	3251	10.2	3.8	1.8	23.2	11.6	1.14 × 10 ⁻¹⁷
9	3753	10.2	3.8	1.8	23.3	9.84	9.71 × 10 ⁻¹⁸

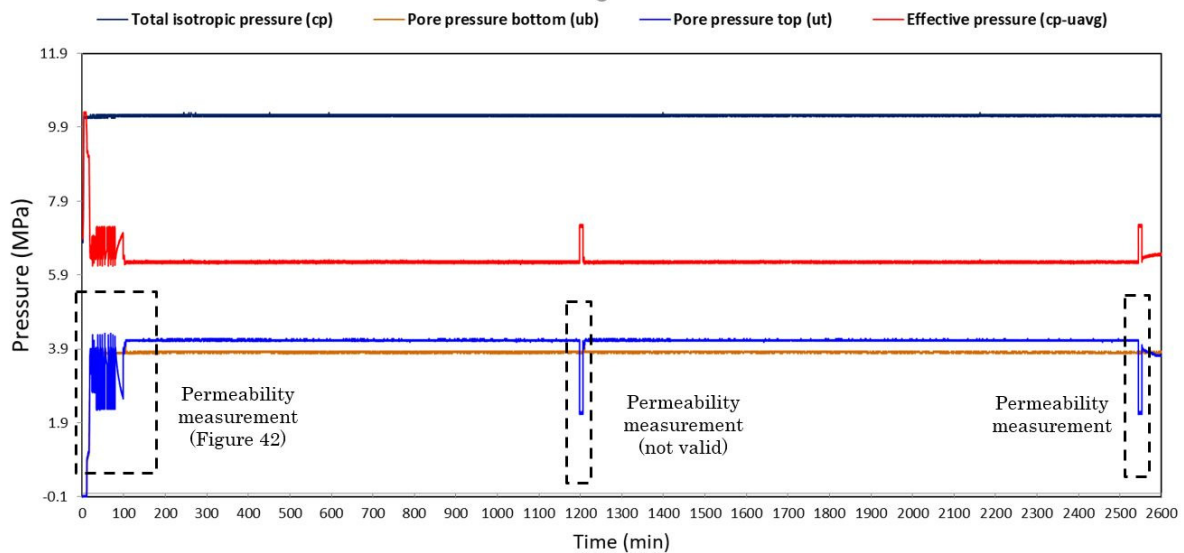


Fig. 45: Stress path applied on the artificially fractured sample immediately after gas experiment

The permeability experiments were performed during the first 80 min as marked in the plot. The swelling kinetics were recorded for the next 44 hours.

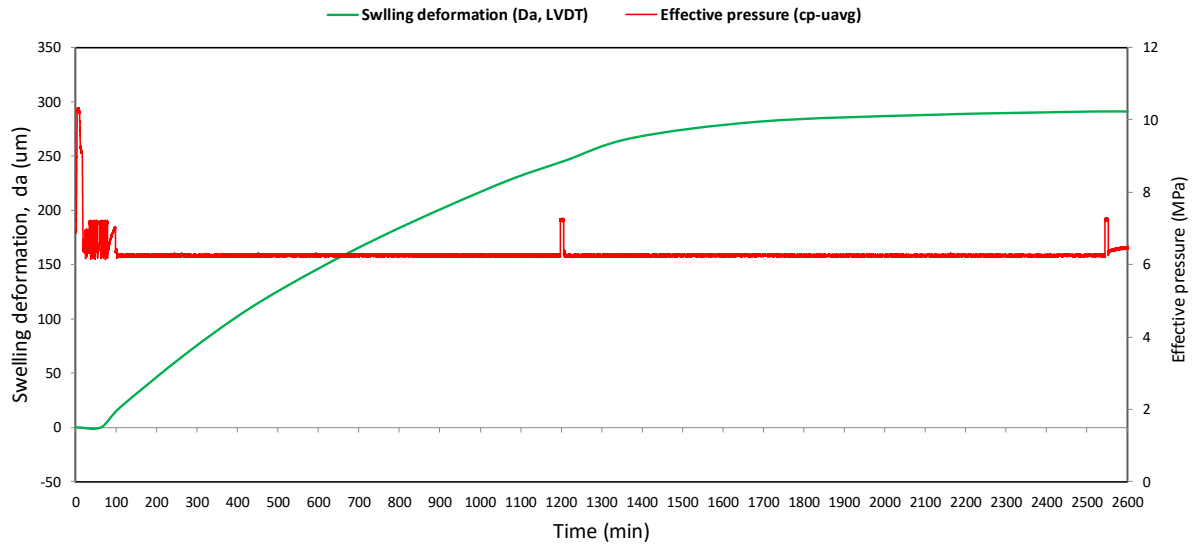


Fig. 46: Variation of the swelling displacement measured using the LVDT positioned normal to the fracture plane for a constant effective pressure over time

The fracture permeability decreases due to the self-sealing process of the fractures as a result of further hydration of the particle surfaces at the fracture plane. The variation of the pore volume at both ends is presented in Fig. 43. The results of the steady-state permeability measurements during the initial self-sealing process are presented in Tab. 6 and Fig. 44. The apparent permeability decreases one order of magnitude from minute 21 to minute 29 (7.45 minutes period). The experiment then was continued under a constant effective stress of about 6.4 MPa for more than 44 hours as demonstrated in The swelling strains were recorded using the measurements from the LVDT positioned normal to the fracture plane (Fig. 46), the radial strain gauge at the fracture location (Fig. 47) and the axial strain gauge in the proximity of the fracture (Fig. 48) as demonstrated in Fig. 29. Several attempts were made to measure the permeability after 45 hours from the beginning of the experiment by applying a pore pressure gradient through the sample and measuring the change in pore volume exchange under a steady state condition. However, the water uptake (diffusion) during swelling proved that the measurement of permeability is not possible even after swelling equilibrium. The variation of the swelling strain and the water uptake during the last 24 hours of the experiment is shown in Fig. 49.

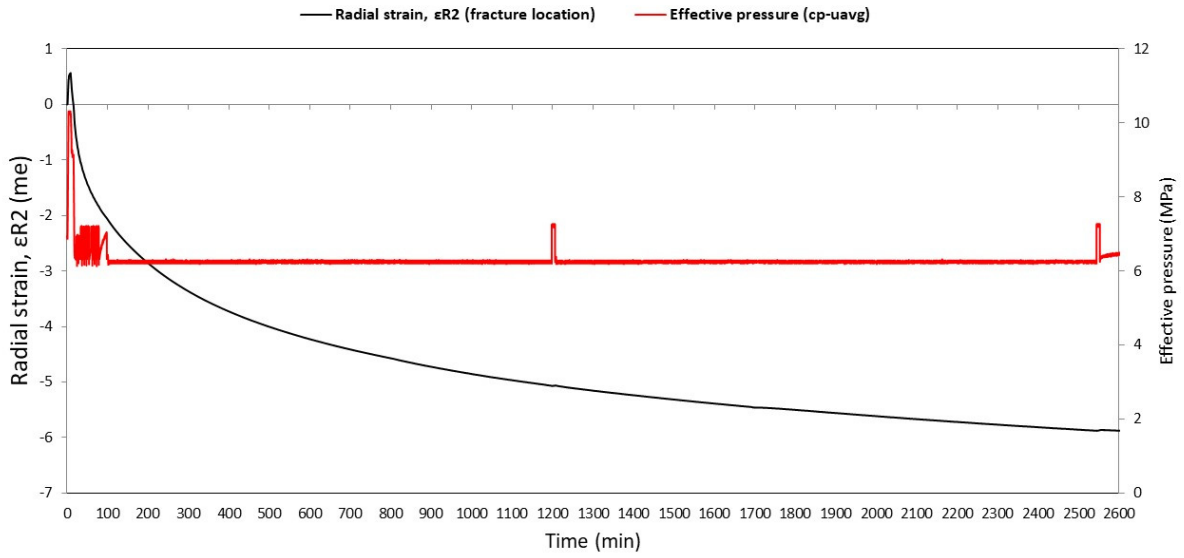


Fig. 47: Variation of the radial strain (in milli-strain) measured using the strain gauge installed on the fracture position (see Fig. 29)

The confining and pore pressures were slowly decreased so that the effective stress was kept almost constant during unloading step. The sample was then taken out from the triaxial assembly and immediately transferred to the X-Ray Micro-CT scanner for the tomography data. The sample was kept in the copper jacket, to preserve the structure after the experiment, while all the sensors were removed carefully. The sample and jacket were sealed using a thin paraffin film to prevent losing water during the scanning.

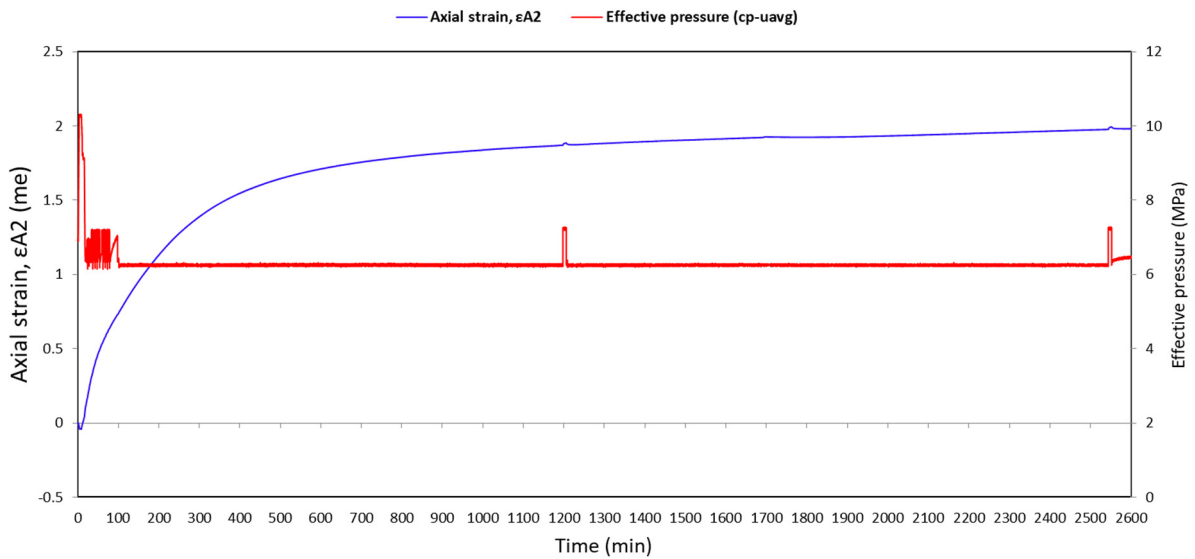


Fig. 48: Variation of the axial strain (in milli-strain) positioned in the proximity of the fracture position (see Fig. 29)

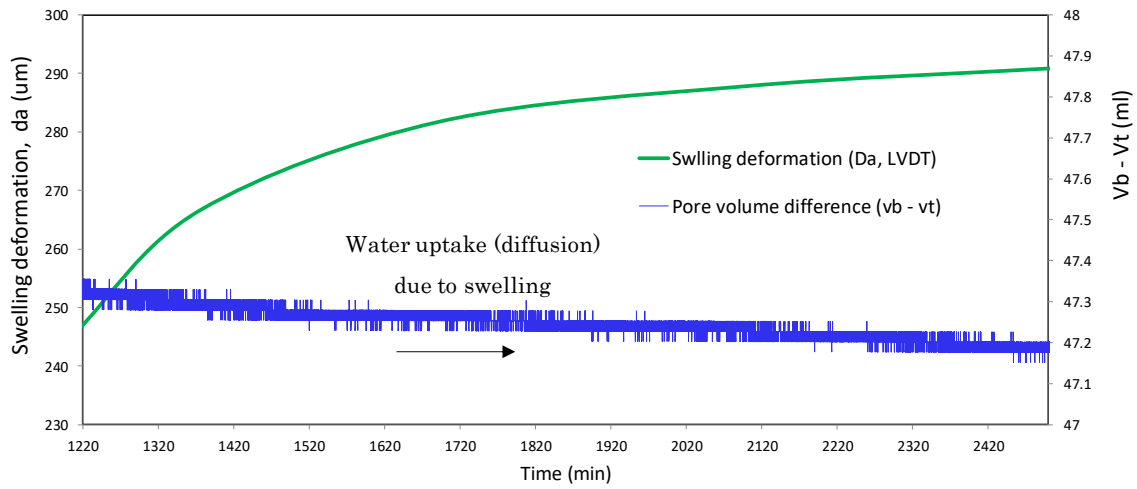


Fig. 49: Variation of the swelling deformation recorded by the LVDT and the pore volume difference ($v_b - v_t$)

The pore volume shows that the material absorbs water due to swelling diffusion related processes.

Tab. 7: Water content and degree of saturation of the Opalinus Clay sample prior and after triaxial testing

Sample	Void ratio, e	In-situ water content, w_{in} (%)	Final water content, w_f (%)	In-situ degree of saturation, Sr_{in} (%)	Final degree of saturation, Sr_f (%)
OPA-BCI- Fractured	0.20	6.95	7.24	95.56	99.55

After scanning, the water content of the sample was measured as 7.24 % with 4.17 % increase, which is associated with the uptake of water by the matrix during swelling of the clay particle. Accordingly, the degree of saturation increases to 99 % for a constant void ratio of 0.20 (Tab. 7). It should be noted that the void ratio might slightly increase due to hydration, and the actual degree of saturation might be larger. However, we posit that the change in the matrix void ratio is negligible and the swelling deformation are due to hydration along the fracture surface.

5.3 Evolution of the internal pore structure due to self-sealing of fractures

5.3.1 Visual observations

The initial and final fracture planes of the Opalinus Clay samples tested in the triaxial cell are shown in Fig. 50, where the swelling and filling the initial gaps can be observed. This behavior is originated from the swelling of the clay aggregates during the hydration and infilling the existing gaps, where the aggregates swell.

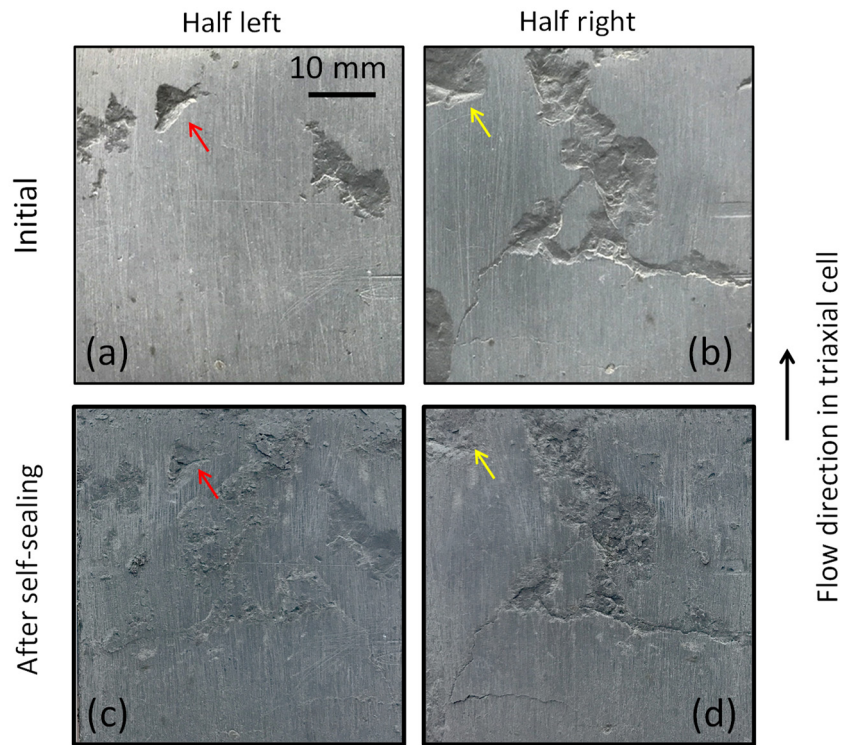


Fig. 50: (a), (b) Initial fracture plane after preparing the artificially fractured sample of the Opalinus Clay; and (c), (d) final fracture plane after triaxial self-sealing experiments, where the swelling and filling the initial gaps can be observed (see Fig. 27)

5.3.2 Evolution of the internal pore structure (X-Ray micro-CT)

The internal fracture pattern and the entire pore structure of the cylindrical Opalinus Clay sample (pore resolution 64-68 μm) were obtained after each stage of the experiments including the initial preparation, jacketing, Ar-gas experiment and the final self-sealing due to pore water experiments. The process of self-sealing of the fractures in a typical cross section of the Opalinus Clay sample after triaxial experiments (detailed in Section 5.2) is shown in Fig. 51. The cross-section is at depth of 3.15 mm from the bottom of the sample in triaxial cell. The sealing of fractures in this plane is clearly observed, particularly after water experiments and activation of the swelling mechanism.

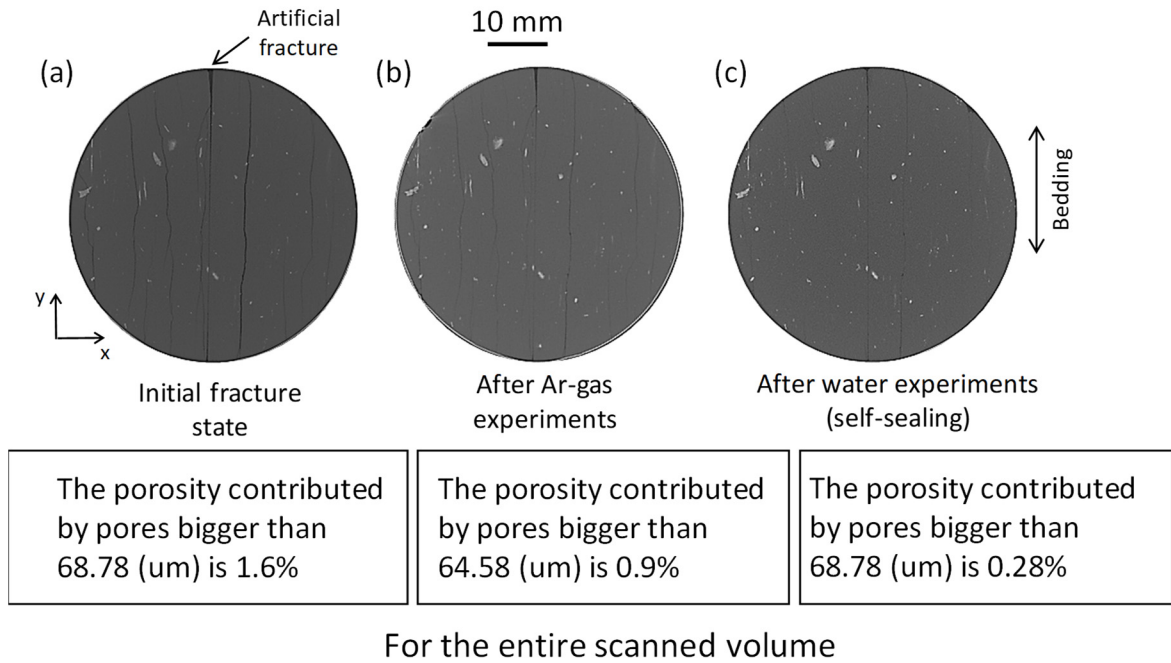


Fig. 51: Process of self-sealing of the fractures in Opalinus Clay sample after triaxial experiments detailed in Section 5.2.

The cross section is at depth of 3.15 mm from the bottom of the sample in triaxial cell. The porosity contributed by pores at the X-Ray resolution are calculated at each stage.

A MATLAB code was developed for 3D reconstruction of the internal pore structure.

The porosity contributed by pores larger than the X-Ray micro-CT resolution is also calculated and presented in Fig. 51. The initial porosity by pores larger than 68.78 μm is 1.6 % which included the pores likely serving as the effective pathways for the flow and transport processes.

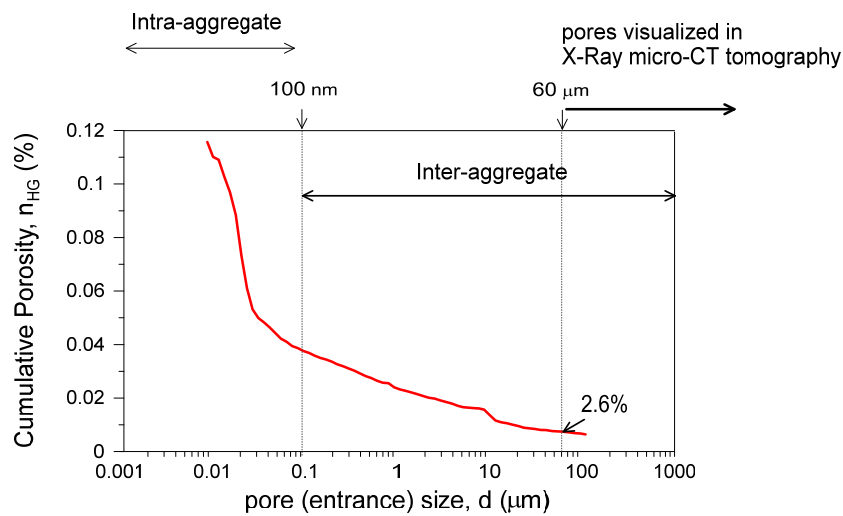


Fig. 52: Range of the pores visualized with the X-Ray micro-CT tomography technique compared with the MIP data for the intruded porosity with respect to the pore entrance size

The pore structure of the cylindrical sample was reconstructed by stacking the x-y plane images (Fig. 51) after each experiment and dismantling the cell. The visualization of the internal pore structure of the cylindrical sample evolved due to interaction with synthetic pore water and the involved hydro-mechanical processes during triaxial experiments reveals a remarkable evolution of the internal pore network after self-sealing experiment as shown in Fig. 53 to Fig. 55.

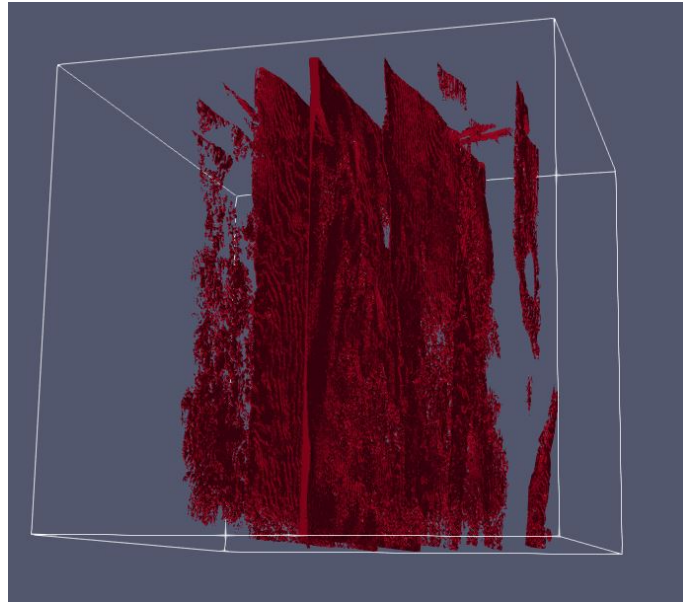


Fig. 53: Internal 3D pore structure of the Opalinus Clay sample (with artificial fracture plane) at initial condition reconstructed from the X-Ray micro-CT data before testing under triaxial condition

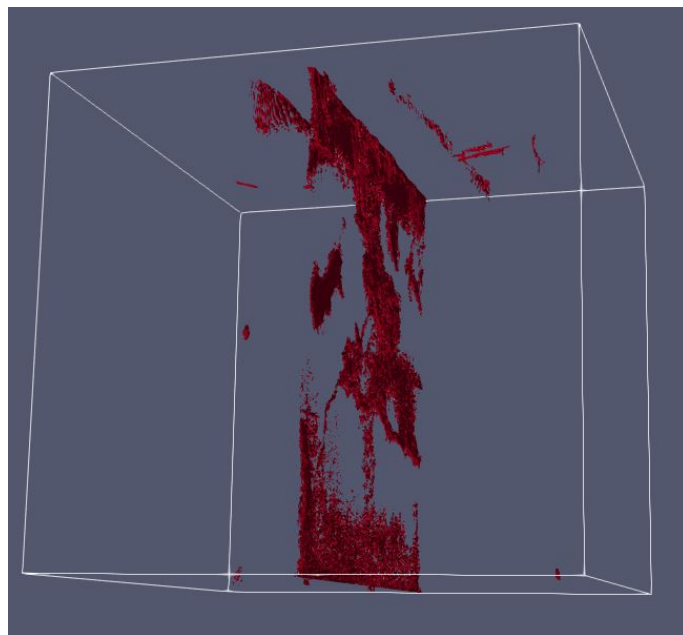


Fig. 54: Internal 3D pore structure of the Opalinus Clay sample (with artificial fracture plane) after self-sealing experiment with synthetic pore water

A remarkable fracture sealing is observed due to a fast swelling process.

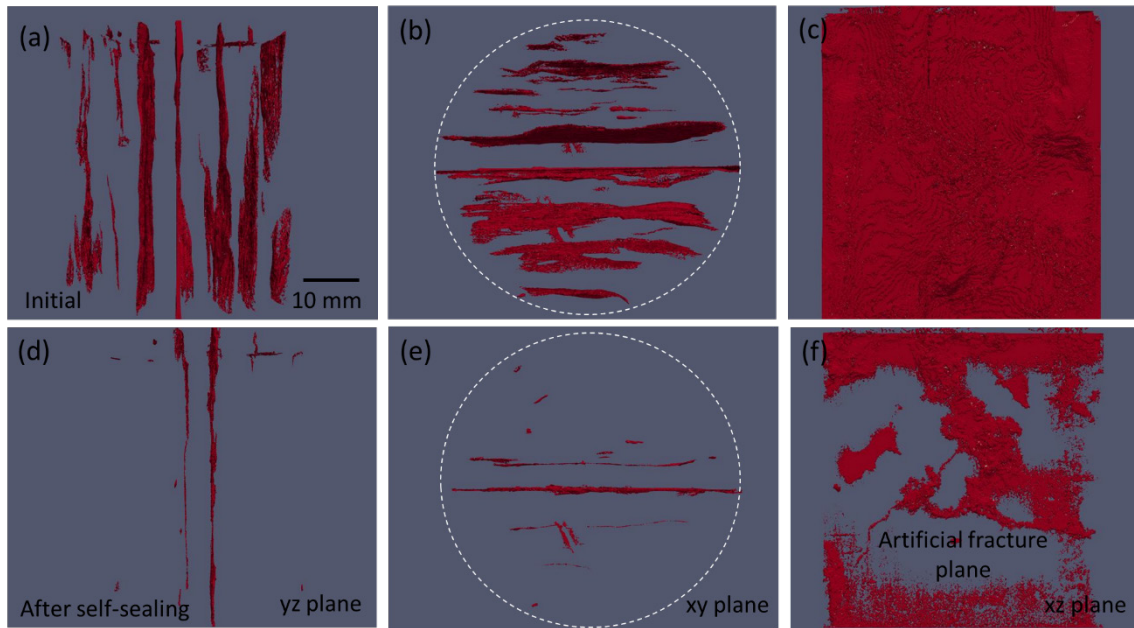


Fig. 55: A comparison between the internal 3D pore structure of the Opalinus Clay sample (with artificial fracture plane)

At initial condition and after self-sealing experiment with synthetic pore water in different planes. The Ar-gas and water flow were applied in the direction normal to the xy plane.

A significant modification of the artificial fracture plane, and a complete elimination of the natural fractures can be observed in these analyses.

6 Summary, conclusions and outlook

We reported a systematic investigation of the self-sealing of fractures in Opalinus Clay material. This research aimed to improve our understanding of the flow and transport processes in the Excavation damaged Zone (EDZ) of the repository tunnels for the storage of high-level radioactive waste in Switzerland. Our study is an innovative multi-scale research to investigate the self-sealing potential of claystones in general, and the Opalinus Clay in particular.

Summary

The strong coupling in hydro-mechanical and chemo-physical behavior of the Opalinus Clay demanded a detailed characterization of this material including the physical and microstructural properties. Detailed bulk and clay fraction mineralogical analysis using X-Ray powder diffraction (XRPD), including the expandability of the mixed-layer illite/smectite was conducted. The pore structural properties of the material were analyzed using the Mercury Intrusion Porosimetry (MIP), and N₂ gas adsorption technique. The internal fracture network of the material was determined using the X-Ray Micro-CT technique to visualize the fractures and geometrical properties. We studied the microfabric properties of the material using the Scanning and Backscattered Electron Microscopy (SEM/BSEM) techniques on the fractured and 2D broad-(Ar)ion beam (BIB) milled surfaces to provide insights into the pore structure and intrinsic heterogeneity behavior, the key elements in fracture permeability in Opalinus Clay material. Systematic triaxial experiments were conducted to mimic the self-sealing of the fractures, on the fully instrumented cylindrical samples including the intact and the artificially fractured geometry. The Ar-gas permeability and fracture transmissivity of the respectively intact and artificially fractured samples along the bedding plane were determined for several cycles of isotropic loading/unloading, while the axial and radial strains were locally measured using high-precision strain gauges installed at several locations on the periphery of the cylindrical samples. The deformation normal to the natural bedding and artificial fracture plane (aperture opening/closing) was directly measured using a radial LVDT, and the elastic wave velocities across the bedding were continuously measured during all experiments. Following the gas experiments, the samples were subject to synthetic water for permeability and fracture transmissivity measurements during transient conditions.

A fast transition in apparent permeability for the synthetic water experiments was observed that indicates the significant self-sealing capacity of the material. The swelling behavior of the material was monitored until a steady-state condition reached under a controlled isotropic effective stress. To determine the evolution of the internal fracture network during different stages of the gas and water permeability analyses, the X-Ray micro-CT technique was conducted. The internal pore structure information revealed a remarkable self-sealing behavior of fractures due to the internal hydration of clay matrix and swelling within the fracture planes. These results are significant in understanding the hydro-mechanical and – chemico-osmotic self-sealing processes in a fractured system of the Excavation Damage Zones (EDZ) in response to resaturation processes after repository closure and provides experimental bases for constitutive modeling of the self-sealing of fractures in the natural and disturbed zones in Opalinus Clay formation.

Key results

The key results of the study can be summarised as follows:

- Phenomenological evidence has been provided to support of Nagra's conceptual framework for fracture closure in Opalinus Clay (see Fig. 7). Fast disintegration of Opalinus Clay samples was observed when subjected to synthetic porewater (e.g.; Fig. 16). The temporal evolution of the disintegration process depends on the diagenetic history of the material (see also Appendix A)
- The experimental data base has been extended to proof the existing fracture closure laws for Opalinus Clay (Fig. 2). The new data bases confirm the strong dependence of fracture permeability on effective stress (Fig. 33, Fig. 34).
- Direct visual evidence for fracture closure has been gained by micro-CT measurements, indicating fast and efficient closure of fracture systems, when subjected to synthetic pore water (Figures 53, 54 and 55).

Concluding remarks and outlook

The study of the diagenetic cementation in Opalinus Clay indicates a strong relation between the self-sealing potential and the degree of burial diagenesis (in terms of cementation bonds) as major factors to be addressed in the long-term safety assessment of radioactive wastes repositories, where the fluid flow and particle transport in fractured Opalinus Clay are fundamentally important. We plan to complement the current study with further triaxial experiments on Opalinus Clay with different end members of different diagenetic effects particularly the deep Opalinus Clay (Schlattingen) with stronger cementation bonds (see Appendix A). Another question of potential relevance is the effect of temperature on the fracture permeability due to the dependence of the Opalinus Clay swelling potential to the temperature. The sensitivity of the swelling potential of the Opalinus Clay to temperature may have both, a positive or negative effect on the self-sealing behavior of the rock which could be uncovered by further experiential investigations.

7 References

- Abouelresh, M.O. & Slatt, R.M. (2012): Lithofacies and sequence stratigraphy of the Barnett Shale in east-central Fort Worth Basin, Texas. AAPG bulletin 96, 1-22.
- Alheid, H., Aranyossy, J., Blümling, P., Hoteit, N. & Van Geet, M. (2007): EDZ Development and Evolution (RTDC 4). EDZ development and evolution. State of the art. NF-PRO. Contract, 2003-02389.
- Bandis, S., Lumsden, A. & Barton, N. (2004): Fundamentals of rock joint deformation. International Journal of Rock Mechanics and Mining Sciences & Geomechanics Abstracts. Elsevier, pp. 249-268.
- Barton, N., Bandis, S. & Bakhtar, K. (1985): Strength, deformation and conductivity coupling of rock joints. International journal of rock mechanics and mining sciences & geomechanics abstracts. Elsevier, pp. 121-140.
- Blümling, P., Bernier, F., Lebon, P. & Martin, C.D. (2007): The excavation damaged zone in clay formations time-dependent behaviour and influence on performance assessment. Physics and Chemistry of the Earth, Parts A/B/C 32, 588-599.
- Bock, H., Dehandschutter, B., Martin, C.D., Mazurek, M., De Haller, A., Skoczylas, F. & Davy, C. (2010): Self-sealing of fractures in argillaceous formations in the context of geological disposal of radioactive waste.
- Bock, H.J.N.T.R.T.-., Q+ S Consult (2000): RA Experiment: Data report on rock mechanics-Mont Terri project.
- Bossart, P. (2018): Twenty years of research at the Mont Terri rock laboratory: what we have learnt. Mont Terri Rock Laboratory, 20 Years. Springer, pp. 407-413.
- Bossart, P., Meier, P.M., Moeri, A., Trick, T. & Mayor, J.-C. (2002): Geological and hydraulic characterisation of the excavation disturbed zone in the Opalinus Clay of the Mont Terri Rock Laboratory. Engineering Geology 66, 19-38.
- Brown, S.R.J.J.o.G.R.S.E. (1987): Fluid flow through rock joints: the effect of surface roughness. 92, 1337-1347.
- Davy, C.A., Skoczylas, F., Barnichon, J.-D. & Lebon, P.J.P., Chemistry of the Earth, P.A.B.C. (2007): Permeability of macro-cracked argillite under confinement: gas and water testing. 32, 667-680.
- Deming, D., Cranganu, C.v Lee, Y. (2002): Self-sealing in sedimentary basins. Journal of Geophysical Research: Solid Earth 107, ETG 2-1-ETG 2-9.
- Diomidis, N. (2016): Production, consumption and transport of gases in deep geological repositories according to the Swiss disposal concept. Nationale Genossenschaft für die Lagerung radioaktiver Abfälle.
- Evans, K., Kohl, T., Hopkirk, R. & Rybach, L.J.P.R.E.T.H., Zürich, Switzerland (1992): Modelling of energy production from Hot Dry Rock systems.

- Fang, Y., Elsworth, D., Wang, C., Ishibashi, T. & Fitts, J.P.J.J.o.G.R.S.E. (2017): Frictional stability-permeability relationships for fractures in shales. 122, 1760-1776.
- Favero, V., Ferrari, A. & Laloui, L. (2016a): On the hydro-mechanical behaviour of reconstituted and natural Opalinus Clay Shale. *Engineering Geology*, 208, p.128–135.
- Freivogel, M. & Huggenberger, P.J.M.T.P.G., *Paleohydrogeology, Report, S.F.o.t.M.T.R.*, 2003. Modellierung bilanzierter Profile im Gebiet Mont Terri–La Croix (Kanton Jura). 7-44.
- Gale, J.E. (1982): The effects of fracture type (induced versus natural) on the stress-fracture closure-fracture permeability relationships. The 23rd US Symposium on Rock Mechanics (USRMS). American Rock Mechanics Association.
- Giot, R., Auvray, C., Conil, N. & de La Vaissière, R.J.E.G. (2018): Multi-stage water permeability measurements on claystone by steady and transient flow methods. 247, 27-37.
- Goodman, R.E. (1976): *Methods of geological engineering in discontinuous rocks*.
- Goodman, R.E., Taylor, R.L., Brekke, T.L.J.J.o.S.M. & Div, F. (1968): A model for the mechanics of jointed rock.
- Gradstein, F., Ogg, J., Schmitz, M. & v Ogg, G. (2012): *The Geologic Time Scale 2-Volume Set*. Elsevier Amsterdam.
- Hofmann, H., Blöcher, G., Milsch, H., Babadagli, T., Zimmermann, G.J.I.J.o.R.M. & Sciences, M. (2016): Transmissivity of aligned and displaced tensile fractures in granitic rocks during cyclic loading. 87, 69-84.
- Johnson, L., Marschall, P., Zuidema, P. & Gribo, P. (2004): Effects of post-disposal gas generation in a repository for spent fuel, high-level waste and long-lived intermediate level waste sited in opalinus clay. National Cooperative for the Disposal of Radioactive Waste (Nagra).
- Kohli, A.H. & Zoback, M.D. (2013): Frictional properties of shale reservoir rocks. *Journal of geophysical research: solid earth* 118, 5109-5125.
- Lanyon, G. & Senger, R. (2011): A structured approach to the derivation of effective properties for combined water and gas flow in the EDZ. *Transport in porous media* 90, 95-112.
- Mäder, U., Jenni, A., Lerouge, C., Gaboreau, S., Miyoshi, S., Kimura, Y., Cloet, V., Fukaya, M., Claret, F. & Otake, T. (2018): 5-year chemico-physical evolution of concrete–claystone interfaces, Mont Terri rock laboratory (Switzerland). *Mont Terri Rock Laboratory, 20 Years*. Springer, pp. 309-329.
- Mäder, U.J.N.A. (2011): Recipe and preparation of a simplified artificial pore water for Opalinus Clay and Brown Dogger. 11-159.
- Marschall, P., Distinguin, M., Shao, H., Bossart, P., Enachescu, C. & Trick, T. (2006): Creation and evolution of damage zones around a microtunnel in a claystone formation of the Swiss Jura Mountains. *SPE International Symposium and Exhibition on Formation Damage Control*. Society of Petroleum Engineers.

- Marschall, P., Giger, S., De La Vassière, R., Shao, H., Leung, H., Nussbaum, C., Trick, T., Lanyon, B., Senger, R. & Lisjak, A. (2018): Hydro-mechanical evolution of the EDZ as transport path for radionuclides and gas: insights from the Mont Terri rock laboratory (Switzerland). *Mont Terri Rock Laboratory, 20 Years*. Springer, pp. 175-196.
- Marschall, P., Horseman, S. & Gimmi, T. (2005): Characterisation of gas transport properties of the Opalinus Clay, a potential host rock formation for radioactive waste disposal. *Oil & gas science and technology* 60, 121-139.
- Marschall, P., Giger, S. (2016): ENSI-Nachforderung zum Indikator "Tiefenlage im Hinblick auf bautechnische Machbarkeit" in Etappe 2 SGT: Geomechanische Unterlagen. *Nagra Arbeitsbericht NAB 16-43*.
- Mazurek, M., Gautschi, A., Marschall, P., Vigneron, G., Lebon, P. & Delay, J. (2008): Transferability of geoscientific information from various sources (study sites, underground rock laboratories, natural analogues) to support safety cases for radioactive waste repositories in argillaceous formations. *Physics and Chemistry of the Earth, Parts A/B/C* 33, S95-S105.
- Mazurek, M., Hurford, A.J. & Leu, W.J.B.R. (2006): Unravelling the multi-stage burial history of the Swiss Molasse Basin: integration of apatite fission track, vitrinite reflectance and biomarker isomerisation analysis. 18, 27-50.
- Nagra (2014a): Etappe 2: Vorschlag weiter zu untersuchender geologischer Standortgebiete mit zugehörigen Standortarealen für die Oberflächenanlage; Geologische Grundlagen; Dossier IV Geomechanische Unterlagen. *Nagra Technischer Bericht NTB 14-02*.
- Nagra (2014b): Etappe 2: Vorschlag weiter zu untersuchender geologischer Standortgebiete mit zugehörigen Standortarealen für die Oberflächenanlage; Geologische Grundlagen; Dossier VI Barriereneigenschaften der Wirt-und Rahmengesteine. *Nagra Technischer Bericht NTB 14-02*.
- Neuzil, C. (1994): How permeable are clays and shales? *Water resources research* 30, 145-150.
- Popp, T., Salzer, K. & Minkley, W. (2008): Influence of bedding planes to EDZ-evolution and the coupled HM properties of Opalinus Clay. *Physics and Chemistry of the Earth, Parts A/B/C* 33, S374-S387.
- Raven, K. & Gale, J. (1985): Water flow in a natural rock fracture as a function of stress and sample size. *International Journal of Rock Mechanics and Mining Sciences & Geomechanics Abstracts*. Elsevier, pp. 251-261.
- Ritzema, H. (2006): Subsurface flow to drains. *Drainage principles and applications*, pp. 263-304.
- Rutqvist, J. & Stephansson, O.J.H.J. (2003): The role of hydromechanical coupling in fractured rock engineering. 11, 7-40.
- Seiphoori, A. (2019): The effects of burial diagenesis on Opalinus Clay behavior: a multiscale study of the pore structure and mechanical properties. *Nagra Arbeitsbericht NAB 19-06*.
- Seiphoori, A., Whittle, A.J., Krakowiak, K.J., Einstein, H.H.J.C. & Minerals, C. (2017): Insights into diagenesis and pore structure of opalinus shale through comparative studies of natural and reconstituted materials. 65, 135-153.

- Sone, H. & Zoback, M. (2011): Visco-plastic properties of shale gas reservoir rocks. 45th US Rock Mechanics/Geomechanics Symposium. American Rock Mechanics Association.
- Thommes, M., Kaneko, K., Neimark, A.V., Olivier, J.P., Rodriguez-Reinoso, F., Rouquerol, J., Sing, K.S.J.P. & Chemistry, A. (2015): Physisorption of gases, with special reference to the evaluation of surface area and pore size distribution (IUPAC Technical Report). 87, 1051-1069.
- Touret, O., Pons, C., Tessier, D. & Tardy, Y. (1990): Etude de la répartition de l'eau dans des argiles saturées Mg²⁺ aux fortes teneurs en eau. *Clay minerals* 25, 217-223.
- Tsang, C.-F., Bernier, F. & Davies, C. (2005): Geohydromechanical processes in the Excavation Damaged Zone in crystalline rock, rock salt, and indurated and plastic clays—in the context of radioactive waste disposal. *International Journal of Rock Mechanics and Mining Sciences* 42, 109-125.
- Witherspoon, P.A., Wang, J.S., Iwai, K. & Gale, J.E.J.W.r.r. (1980): Validity of cubic law for fluid flow in a deformable rock fracture. 16, 1016-1024.
- Zhang, C.-L. (2011): Experimental evidence for self-sealing of fractures in claystone. *Physics and Chemistry of the Earth, Parts A/B/C* 36, 1972-1980.
- Zhang, C.-L. (2013): Sealing of fractures in claystone. *Journal of Rock Mechanics and Geotechnical Engineering* 5, 214-220.
- Zimmerman, R. & Main, I.J.I.G.S. (2004): Hydromechanical behavior of fractured rocks. 89, 363-422.
- Zimmerman, R.W. & Bodvarsson, G.S.J.T.i.p.m. (1996): Hydraulic conductivity of rock fractures. 23, 1-30.

Appendix A: Interaction of Opalinus Clay with synthetic water

Time-lapse visual observation of the reaction of the Opalinus Clay from Mont Terri and Schlattingen sites with synthetic water was conducted as presented in Fig. A-1 and A-2. The synthetic water was prepared according to Mäder (2011). The Mont Terri material exhibits intense slaking behavior short time after immersed in the synthetic water, suggesting slight cementation in the natural state. A fast swelling of the surface is observed immediately after the material surface hydrates even using the synthetic water with considerable salinity of 13.98 g/L. This behavior indicates that the repulsive forces building up during the hydration of the aggregates can overcome the inter-aggregate cementation bonding and result in disintegration of the entire aggregates, while in Schlattingen material, the stronger bonds can resist the inter-particle repulsion (note: a comprehensive geotechnical characterization of the Opalinus Clay from the Schlattingen site is found in Favero et al. 2016a and Marschall & Giger 2016).

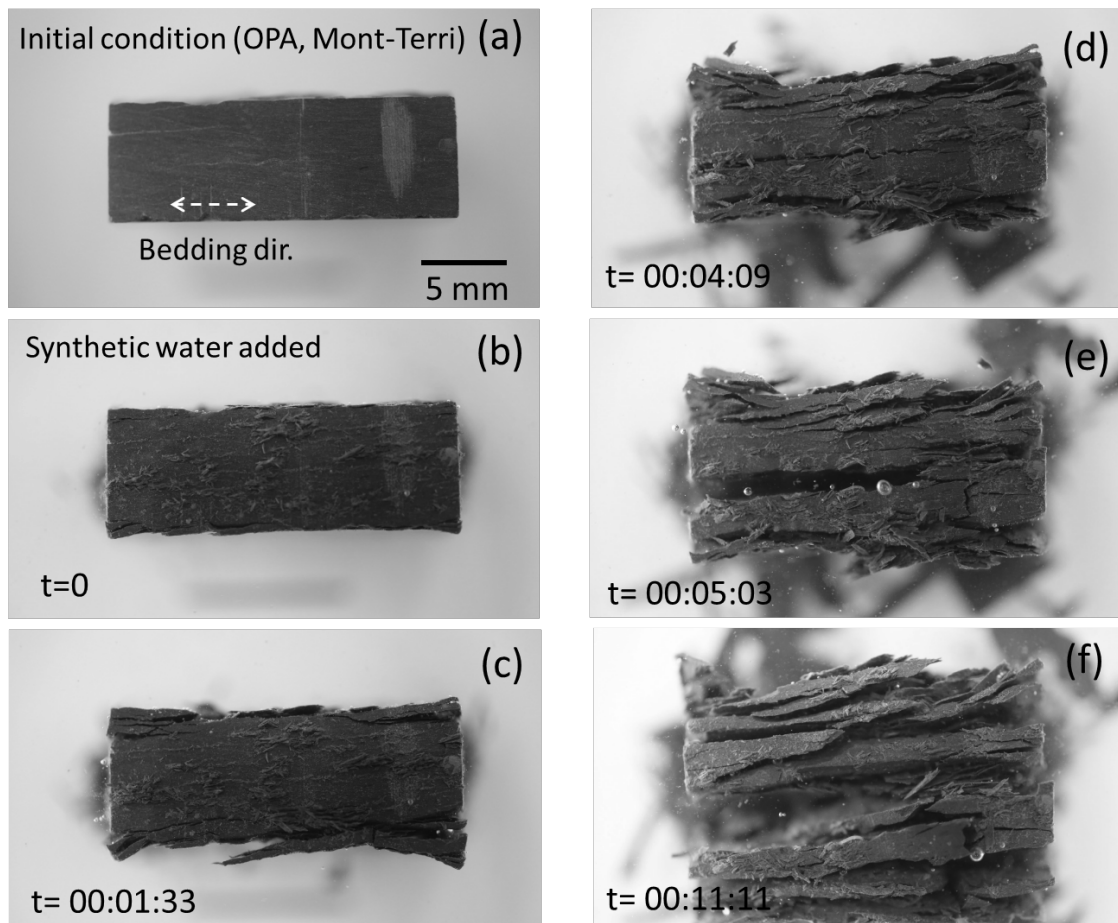


Fig. A-1: Time-lapse visual observation of the reaction of Mont Terri OPA (BCI-21B, Clay content about 67 %) material with synthetic pore water, and fast disintegration of the material due to hydration and swelling

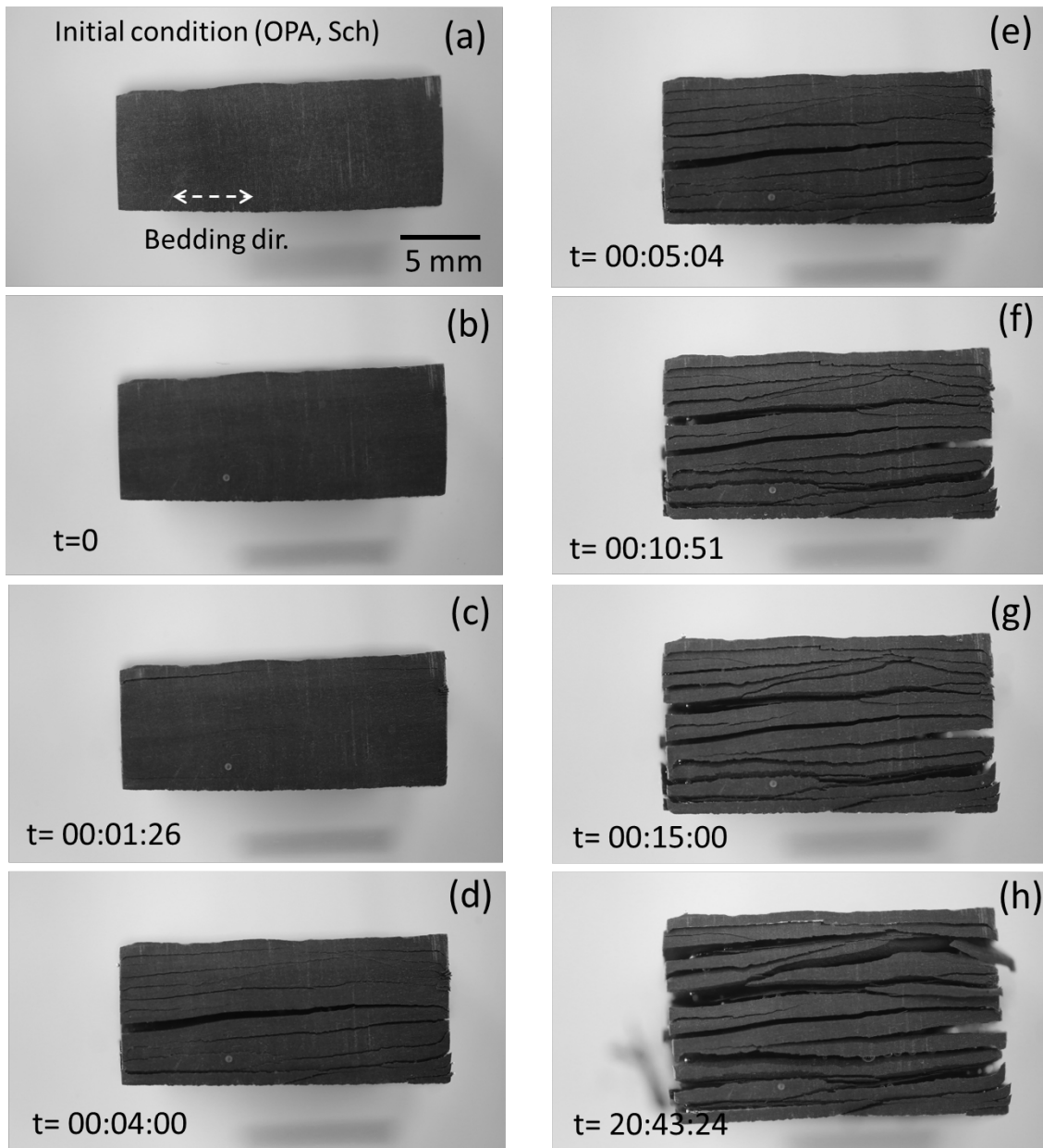


Fig. A-2: Time-lapse visual observation of the reaction of Schlattingen OPA (Molasse Basin, SLA-1 well, depth about 850 m, clay content about 55 %) material with synthetic pore water with less significant disintegration of the aggregates compared with the Mont Terri material

Appendix B: Steady-state Ar-gas permeability measurement in triaxial cell

This table summarizes the steady-state (apparent) permeability measurement of the artificially fractured Opalinus Clay sample (OPA-BCI-fractured) in triaxial testing condition described in Section 5.1 and plotted in Fig. 33.

Tab. A-1: Steady-state permeability measurement of the artificially fractured Opalinus Clay sample (OPA-BCI-fractured)

Event	Type	Conf (MPa)	Pore top (MPa)	Diff (MPa)	Temp (°C)	Perm (μD)	Perm (m^2)
0	Steady-state	7.0	3.6	1.8	22.7	NA	NA
1	Steady-state	7.0	3.6	1.8	22.6	2.44e+04	2.41E-14
2	Steady-state	7.0	3.6	1.8	22.6	1.95e+04	1.92E-14
3	Steady-state	7.0	3.6	1.8	22.5	2.08e+04	2.05E-14
4	Steady-state	10.7	3.8	1.8	22.4	1.35e+04	1.33E-14
5	Steady-state	10.7	3.8	1.8	22.4	1.26e+04	1.24E-14
6	Steady-state	10.7	3.8	1.8	22.2	1.31e+04	1.29E-14
7	Steady-state	10.7	3.7	1.8	22.3	1.54e+04	1.52E-14
8	Steady-state	10.7	3.8	1.8	22.2	1.36e+04	1.34E-14
9	Steady-state	12.8	3.8	2.0	22.4	1.11e+04	1.1E-14
10	Steady-state	12.8	3.8	2.0	22.4	1.12e+04	1.11E-14
11	Steady-state	12.8	4.0	2.0	22.3	1.01e+04	9.97E-15
12	Steady-state	15.8	3.9	2.0	22.4	7.77e+03	7.67E-15
13	Steady-state	15.9	3.9	2.2	22.4	8.30e+03	8.19E-15
14	Steady-state	15.8	3.9	2.0	22.4	7.44e+03	7.34E-15
15	Steady-state	12.8	3.8	2.0	21.9	8.19e+03	8.08E-15
16	Steady-state	12.8	3.8	2.0	22.0	8.30e+03	8.19E-15
17	Steady-state	12.8	3.8	2.0	21.9	8.22e+03	8.11E-15
18	Steady-state	10.8	3.8	1.8	21.7	8.75e+03	8.64E-15
19	Steady-state	10.9	3.8	1.8	21.8	8.56e+03	8.45E-15
20	Steady-state	10.9	3.6	1.8	21.8	7.97e+03	7.87E-15
21	Steady-state	7.9	3.6	1.8	21.6	1.07e+04	1.06E-14
22	Steady-state	7.9	3.6	1.8	21.6	1.09e+04	1.08E-14
23	Steady-state	8.0	3.6	1.8	21.7	1.19e+04	1.17E-14
24	Steady-state	10.9	3.7	1.8	22.6	9.14e+03	9.02E-15
25	Steady-state	10.8	3.7	2.0	22.6	9.20e+03	9.08E-15
26	Steady-state	10.8	3.8	1.8	22.5	1.00e+04	9.87E-15

Tab. A-1: Cont.

Event	Type	Conf (MPa)	Pore top (MPa)	Diff (MPa)	Temp (°C)	Perm (μD)	Perm (m^2)
28	Steady-state	12.7	3.7	2.0	22.2	7.98e+03	7.88E-15
29	Steady-state	12.8	3.8	2.0	22.2	8.61e+03	8.5E-15
30	Steady-state	14.1	3.8	2.0	22.2	7.70e+03	7.6E-15
31	Steady-state	14.1	3.8	2.0	22.2	7.73e+03	7.63E-15
32	Steady-state	16.1	3.8	2.0	22.1	6.69e+03	6.6E-15
33	Steady-state	16.1	3.8	2.0	22.1	6.73e+03	6.64E-15
34	Steady-state	16.1	3.8	2.0	22.1	6.56e+03	6.47E-15
35	Steady-state	14.1	3.8	1.8	22.5	6.89e+03	6.8E-15
36	Steady-state	14.2	3.8	2.0	22.4	7.06e+03	6.97E-15
37	Steady-state	14.1	3.8	1.8	22.0	6.75e+03	6.66E-15
38	Steady-state	14.2	3.8	1.8	22.1	6.76e+03	6.67E-15
39	Steady-state	12.8	3.8	2.0	22.0	7.53e+03	7.43E-15
40	Steady-state	12.8	3.8	1.8	22.2	7.00e+03	6.91E-15
41	Steady-state	10.9	3.8	1.8	22.0	7.69e+03	7.59E-15
42	Steady-state	10.9	3.8	1.8	22.0	7.94e+03	7.84E-15
43	Steady-state	10.9	3.8	1.8	22.0	8.01e+03	7.91E-15
44	Steady-state	10.9	3.8	1.8	22.0	8.27e+03	8.16E-15
45	Steady-state	9.2	3.7	1.6	21.8	8.80e+03	8.69E-15
46	Steady-state	9.2	3.8	1.6	21.9	9.47e+03	9.35E-15
47	Steady-state	9.2	3.8	1.6	22.6	9.23e+03	9.11E-15
48	Steady-state	9.2	3.8	1.8	22.7	9.22e+03	9.1E-15
49	Steady-state	7.8	3.7	1.8	22.4	8.87e+03	8.75E-15
50	Steady-state	7.8	3.7	1.8	22.5	1.00e+04	9.87E-15
51	Steady-state	7.8	3.7	1.8	22.5	9.82e+03	9.69E-15
52	Steady-state	7.8	3.7	1.8	22.5	9.77e+03	9.64E-15
53	Steady-state	16.0	3.8	2.0	22.7	5.95e+03	5.87E-15
54	Steady-state	16.0	3.8	2.0	22.7	6.21e+03	6.13E-15
55	Steady-state	16.1	3.8	2.0	22.6	6.11e+03	6.03E-15
56	Steady-state	16.0	3.8	1.8	23.2	4.11e+03	4.06E-15
57	Steady-state	16.0	3.8	1.8	23.3	4.16e+03	4.11E-15
58	Steady-state	16.1	3.8	1.8	23.3	4.94e+03	4.88E-15
59	Steady-state	16.0	3.8	1.8	23.9	4.94e+03	4.88E-15
60	Steady-state	16.1	3.8	1.8	24.0	5.40e+03	5.33E-15

Tab. A-1: Cont.

Event	Type	Conf (MPa)	Pore top (MPa)	Diff (MPa)	Temp (°C)	Perm (μ D)	Perm (m^2)
61	Steady-state	16.2	3.8	1.8	23.9	4.00e+03	3.95E-15
62	Steady-state	16.2	3.7	1.8	23.9	4.02e+03	3.97E-15
63	Steady-state	14.1	3.8	1.8	23.4	4.28e+03	4.22E-15
64	Steady-state	14.2	3.8	1.8	23.3	4.38e+03	4.32E-15
65	Steady-state	12.2	3.8	1.8	23.1	4.84e+03	4.78E-15
66	Steady-state	12.1	3.8	1.6	23.1	4.74e+03	4.68E-15
67	Steady-state	10.1	3.8	1.6	23.0	5.31e+03	5.24E-15
68	Steady-state	10.2	3.8	1.6	23.0	5.46e+03	5.39E-15
69	Steady-state	8.1	3.8	1.4	22.8	6.40e+03	6.32E-15
70	Steady-state	8.1	3.8	1.6	22.9	6.63e+03	6.54E-15
71	Steady-state	10.2	3.8	1.6	23.2	6.03e+03	5.95E-15
72	Steady-state	10.1	3.8	1.6	23.2	5.60e+03	5.53E-15
73	Steady-state	12.1	3.8	1.6	23.4	5.08e+03	5.01E-15
74	Steady-state	12.1	3.8	1.6	23.3	5.03e+03	4.96E-15
75	Steady-state	14.1	3.8	1.8	23.5	4.69e+03	4.63E-15
76	Steady-state	14.1	3.8	1.8	24.1	4.68e+03	4.62E-15
77	Steady-state	16.2	3.8	1.8	24.3	4.21e+03	4.16E-15
78	Steady-state	16.2	3.8	1.8	24.3	4.05e+03	4E-15
79	Steady-state	6.1	3.6	1.4	23.4	7.60e+03	7.5E-15
80	Steady-state	6.1	3.6	1.4	23.4	7.68e+03	7.58E-15
81	Steady-state	6.2	3.6	1.4	23.6	8.45e+03	8.34E-15

Appendix C: Steady-state water permeability measurements according to Tab. 6

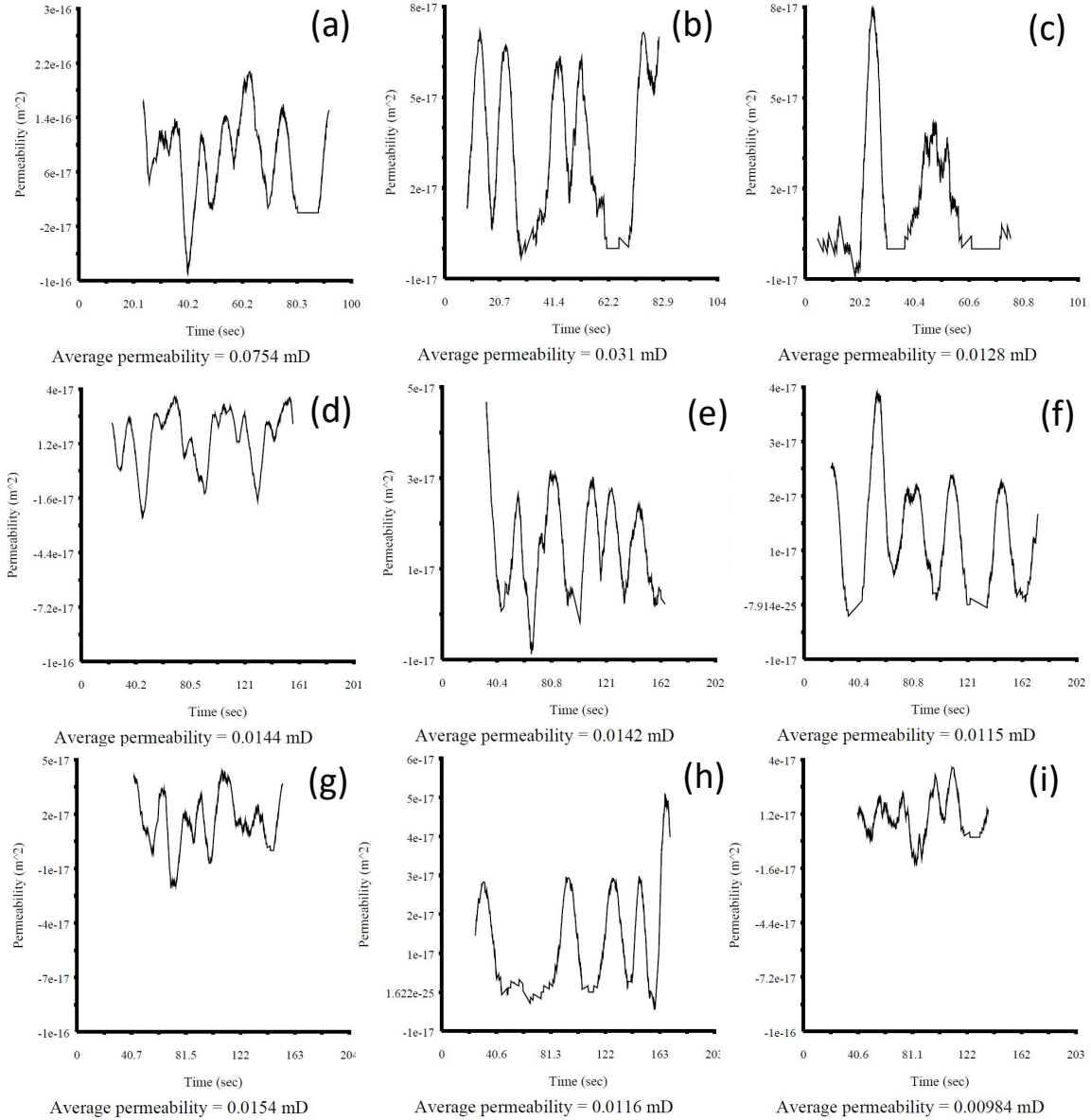


Fig. C-1: Permeability versus time during the steady-state measurement of the synthetic water permeability during the self-sealing experiment on sample OPA-BCI-fractured
 See Tab. 6 for the corresponding test numbers